Optimizing Laser Powder Bed Fusion (L-PBF) for Improved Performance: A Reinforcement Learning Approach for Choosing Process Parameters

Materials Engineering in Energy Technology
Department of Mechanical and Materials Engineering
Master's thesis

Author(s):
Sakshi Amin

Supervisor(s):
Wallace M. Bessa
Sampsa Laakso
Kandice S.B Ribeiro

29.7.2025
Turku

Master's thesis

Subject: Materials Engineering in Energy Technology
Author(s): Sakshi Amin
Title: Optimizing Laser Powder Bed Fusion (L-PBF) for Improved Performance: A Reinforcement Learning Approach for Choosing Process Parameters
Supervisor(s): Wallace M. Bessa, Kandice Barros Riberio, Sampsa Laakso
Number of pages: pages
Date: 29.07.2025

Abstract.

Laser Powder Bed Fusion (L-PBF) is a high-performance manufacturing process for parts with complex geometries. However, a poor choice of process parameters induces the formation of defects, suggesting the need for an improved control system to optimize the result. This paper presents a control policy using Reinforcement learning (RL) for optimizing key process parameters such as laser power (P) and scanning speed (V), aiming to maintain melt pool depth. In this approach, Q learning algorithm iteratively learns how to choose optimal process parameters by maximizing a reward function designed to minimize deformation. A melt pool is simulated using Flow 3D for SS316L, while part-scale deformations are investigated with Finite Element method (FEM). Response surface methodology (RSM) is used to statistically analyse as well as validate deformation behaviour. The proposed approach is the first step towards a data-driven, intelligent control system aimed at optimizing process parameters for stable melt pool depth and minimizing defect formation in L-PBF.

Key words: melt pool, finite element method, reinforcement learning, process parameter optimization, laser powder bed fusion, Response surface methodology (RSM), defect formation, SS316L.

Table of contents

Nomenclature

Abbreviation	**Long form**
AM	Additive manufacturing
RL	Reinforcement Learning
L-PBF	Laser powder bed Fusion
CFD	Computational fluid dynamics
FEM	Finite element method
CAD	Computer-aided drawing
PLC	Programmable logic control
CNC	Computer numerical machine
DEM	Discrete element modelling
SS316L	Stainless steel 316L (An alloy of Fe)
GA	Gas Atomization
PSD	Particle size distribution
RSM	Response surface method
DED	Directed Energy Method
CNN	Convolution Neural Network
SVM	Support vector machine
FGPA	Field programmable gate array
RBF	Gaussian Radial basis network
SIFT	Scale Invariant Feature Transform
BoW	Bag of words
GMM	Gaussian mixture model
PCA	Principal component analysis
PPO	Proximal policy optimization
DZ	Deposition zone
HAZ	Heat-affected zone
RZ	Remelting zone
SEM	scanning electron microscopy
DQN	Deep Q networks
PD	Packing Density
MLP	Multilayer Perception

Symbols used in this study	**Unit**	**Definition**
ϵ_d	J/mm³	Laser Energy Density
e	-	Coefficient of resititution
ν	-	Poisson's ratio
α	1/K	Thermal coefficient
cp	J/kg·K	Specific Heat
k (can also be denoted as λ)	W/m·K	Themal conductivity
E	MPa	Youngs Modulus
ρ	kg/ m³	Bulk density
k	N/ m^2	Spring constant
AED	J/mm³	Area Energy Density (Laser energy density absorbed by material per unit volume)
m_i	kg	Mass of particle i
u_i	m/s	Velocity of particle i
$\frac{du_i}{dt}$	m/s²	Acceleration of particle
F_{ij}^n	N	Normal contact force from j to i
F_{ij}^t	N	Tangential contact force
F_{ij}^a	N	Adhesive force
F_i^B	N	Body force (e.g., gravity)
I_i	kg·m²	Moment of inertia of particle i
ω_i	rad/s	Angular velocity of particle i

M_{ij}^t	N·m	Torque due to tangential force
M_{ij}^r	N·m	Torque due to rolling resistance
k_n	N/m	Normal stiffness
δ_{ij}^n	m	Normal overlap/displacement
n_{ij}	-	Unit normal vector between particles
η_n	kg/s	Normal damping coefficient
u_{ij}^n	m/s	Normal relative velocity between particles
e_n	-	Normal restitution coefficient
m_{ij}	kg	Reduced mass particle of i,j
π	-	pi
ln	-	natural log
μ		Coefficient of friction
μ_{Spw}	-	Coefficient of static friction- (particle wall)
μ_{Dpw}	-	Coefficient of dynamic friction- (particle wall)
μ_{Spp}	-	Coefficient of static friction- (particle particle)
μ_{Dpp}	-	Coefficient of dynamic friction- (particle particle)
SE	J/m^2	Surface energy (use to denote adhesion)
AIF	φ (◦)	Angle of internal friction
$T(x,y,z,t)$	K(Kelvin)	Temperature at position and time
W	W/m^3	Heat source intensity (volumetric)
$\nabla^2 T$	K/m^2	Laplacian of temperature
$\frac{\partial T}{\partial t}$	K/s	Time rate of temperature change
$\frac{\partial T}{\partial n}$	K/m	Temp. gradient in normal direction
q	W/m^2	Heat flux
γ	W/(m^2·K)	Heat exchange coefficient (convective)

T_f	K (Kelvin)	Ambient/fluid temperature
σ	Pa	Cauchy stress tensor
ε	–	Total strain
ε_e	–	Elastic strain component
ε_p	–	Plastic strain component
ε_{th}	–	Thermal strain component
F_v	N/m³	Body force per unit volume
D10	µm	The largest 10% particle size
D50	µm	The largest 50% particle size
D90	µm	The largest 90% particle size
I_0	W/m²	Maximum beam intensity representing laser power per unit area

1 Introduction

Additive manufacturing excels in crafting intricate designs and complex geometries, revolutionizing industries from aerospace to healthcare. Moreover, its efficiency and resource optimization are aimed at innovation and sustainability, reshaping the manufacturing landscape for the future. [1]

The Laser Powder Bed Fusion (LPBF) technique is one among several processes of additive manufacturing (AM) [2]. In this process, loose powder material is deposited uniformly onto a build platform and is then melted and fused using a Laser, which acts as a heat source.[2], [3]. While L-PBF seems to be useful and robust with active use in industries, some defects arise in this process that lowers its efficiency and cause failure in a product. Understanding and controlling these defects is essential for optimization of the L-PBF process and achieving top-quality, reliable parts. The melt pool is a complicated interplay of process parameters, significantly influencing defect formation and ultimately affecting the part quality. Hence, process monitoring and process parameter optimization are critical to achieving instant high-quality parts[4]. Traditional process optimization approaches, such as Design of Experiment (DOE) methods like Taguchi or full factorial DOE, can be both high in costs and time-consuming, as they require manufacturing and analysis of many physical specimens[5]. Moreover, some of these methods can only optimize singular process parameters at a time. On the contrary, application of machine learning is found to be favorable in process optimization compared to traditional methods due to its ability in parameter prediction without requiring prior knowledge of the underlying mechanisms of the system[6]. Machine learning techniques such as Convolutional neural networks (CNN), Artificial neural networks, Support vector Machine (SVM),Gaussian Radial basis network (RBF) and Reinforcement Learning (RL) have shown promising results in real time process monitoring, control and optimization [3], [7], [8], [9].

Reinforcement Learning has emerged as a powerful tool to tackle complex control systems and process parameter optimization by automatically learning control policies through its interaction with simulated environments and using feedback to enhance decision-making.[4] [5]. Due to its capability of self-learning and adapting to changing conditions of the simulated environment or previously unseen process parameters, it can access a more comprehensive range of information and strengthen its decision-making process accordingly, making it quite attractive for complex process optimization and control applications.[10] Integrating Reinforcement learning (RL) with AM, especially to develop a control system for process parameter optimization, is appealing due to the possibility of increased efficacy in the process, increased part quality, and ease of process [11]. There has been some exploration in RL methods for making a control policy for process parameter optimization to detect and mitigate defects in a melt pool, although few as compared to other Machine learning techniques.[7], [12].

The motivation behind this study is to improve the performance of Laser Powder Bed Fusion process(L-PBF) by optimizing key process parameters using this novel and emerging technique of Reinforcement learning (RL). This approach is a significant step towards intelligent control system capable of minimizing defect formation in L-PBF through process parameter optimization. To apply this motivation, accurate modeling of the L-PBF process is required. Understanding how key process parameters influence the thermal and physical phenomena of the material and process is essential, as they affect the melt pool behavior and defect formation. Using traditional experimental investigation is often tedious and expensive for the scale of this study. Hence, we rely on high-fidelity numerical methods such as Computational Fluid Dynamics (CFD) and Finite Element Modeling (FEM) to model this process[6] With this in mind, this study is structured into three main research objectives: -

1. Simulate the melt pool behaviour for SS316L material.
   - We investigate the ability to generate melt pool profiles that reflect realistic behaviour for a few scanning speed (V) and laser power (P) combinations, and understand how these parameters influence the melt pool depth. This also includes applying proper validation methods to ensure the simulations obtained are reliable.
2. Studying the L-PBF process through FEM.
   - Accurately modelling the L-PBF process and capturing the relevant thermal and mechanical phenomena that result in deformations. We also aim to apply appropriate validation methods and analyse the results.
3. Designing a control system using Reinforcement learning (RL)
   - Building a smart control system using an RL method, capable of selecting optimal process parameters (P and V) through reward-driven learning, hence minimizing deformation. Furthermore, we also evaluate the learning behaviour and the performance of the RL agent based on its convergence.

1.1 Additive Manufacturing

1.1.1 Introduction to Additive Manufacturing

The acceptance of Additive manufacturing processes has been increasing due to their benefits, such as increased manufacturing speed and the reduction of conventional processes, such as die punching and casting, which require numerous specialized tools. Some other key benefits are the cleanliness and versatility of the AM processes, short time for prototyping, and the ability of low volume on-demand production. [13], [14], [15] To create a part in AM, there are several steps involved, which are highlighted in Figure 1. Usually, Computer-aided design (CAD) is used to make a 3D object or surface that will be compatible with printing in an AM machine. The next step is to set the machine up for adjusting the energy source, defining layer thickness, and preparing the material tailored to the specific AM process.
Once the setup is ready, the part is ready to be built by the machine through an automated process.[14]

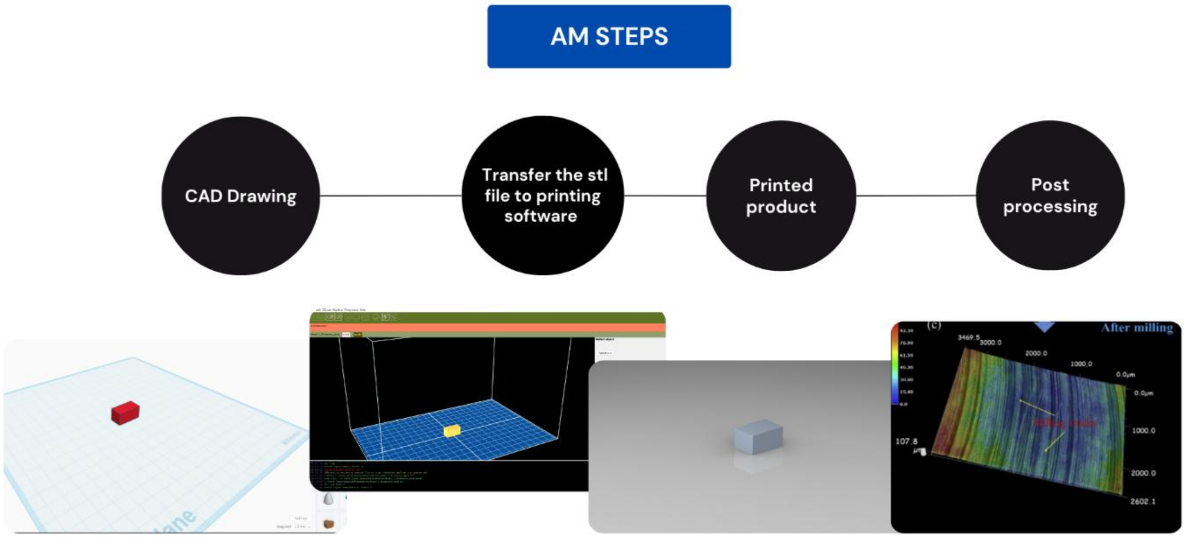

Figure 1 Steps involved in the AM process [14], [16]

After building and removal of the part through appropriate safety measures, it may not be directly used due to various reasons, such as the parts still being weak, built with additional supporting structures that are mostly vestigial, poor surface finish, or part dimensional inaccuracies; hence, post-processing is required to increase the part functionality, features, and appearance. These post-processing techniques can be mechanical, chemical or Laser based treatments as shown in Figure 2 [16], [17], [18].

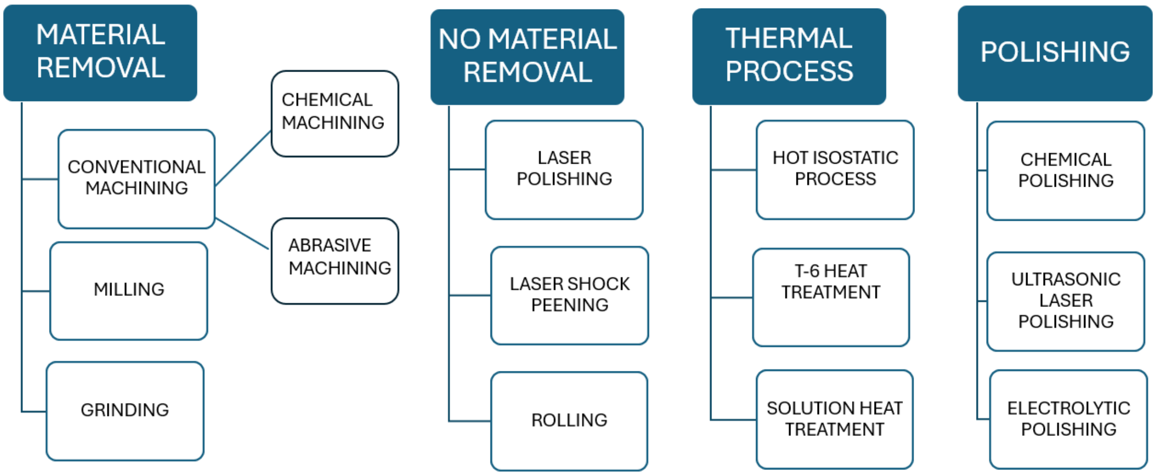

Figure 2 Various post-processing techniques

According to the ASTM/ISO standard terminology[19]There are seven AM processes. Table1. summarises the working principles of these processes and highlights their benefits.

AM PROCESS	WORKING PRINCIPLE	BENEFITS	REF
VAT Polymerization	Layer by layer printing of a photopolymer such as resin and then a light source such as UV light or visible light is used to solidify it. Three different techniques are used: stereolithography, digital light synthesis (DLS), and digital light processing (DLP). There are two techniques for scanning, which can be either top-down configuration or bottom-up mask projection.	- High precision and capable of achieving a high resolution, excellent thermal resistance, and smoother texture of the finished part. - Low shrinkage, fast curability, which is rarely achievable in any other AM techniques. - Less material waste and cheaper due to stereolithography materials being cheaper and available	[14], [20], [21]

		-	
Powder Bed fusion	Powder bed fusion process involves spreading layers of metal powder on a build platform one after the other. With the help of a heat source such as laser or electron beam the powder is fused in a layer wise fashion until a part is created.	- Great for small-scale parts as it gives high dimensional accuracy for complex, detailed parts used in heavy-duty industries. - A higher percentage of medical devices printed through L-PBF are FDA approved, making it a favourable choice over other AM processes.	[22], [23]
Material Jetting	In Material Jetting, a photopolymer which is stored in a tank, is transferred to the nozzle and deposited on the build platform drop by drop. A light source, such as a UV lamp, is used for curing it. Support material such as wax is required to support the integrity of the part.	- Ability to control elasticity and transparency. - High quality due to being able to control layer thickness. - Versatility with colour. Low surface roughness.	[24], [25]
Binder jetting	Powder particles spread on a build platform are bonded to create a desired part using a binding agent flowing from a print head. The powder material can be either ceramics or metal, and the binding agent is usually an adhesive, for example, resin or silica	- Almost all Powder materials are used in this process as it offers versatility. - Material leaves little residue after thermolysis. - The need for support structure is reduced, hence making this process highly desirable for the healthcare industry.	[26], [27]

Directed deposited Energy (DED)	A laser is used to melt powder feedstock that is fed through a nozzle on a built platform. A melt pool is created, and the process is repeated by moving the nozzle until the desired 3D part is created.	- DED can produce larger parts than L-PBF due to more design autonomy. - Printing in non-horizontal surfaces is also possible. - It is a hybrid and more dynamic offering both additive and subtractive	[28], [29]
Solid state lamination	Characterised as one of the oldest methods of Additive manufacturing. In this process layer by layer welding of metal sheets on a laminated workpiece is achieved using a hot press. Then the desired 3D shape is cut out of the top layer and the unnecessary parts are discarded and cannot be reused.	- Inexpensive raw materials, quick and low-cost manufacturing. - Parts can be deployed immediately after they are fabricated. - Material can be managed easily and is environmentally friendly	[14], [30], [31]
Material extrusion	In Material extrusion a polymer material either in wire or pellet form is fed into a deposition unit and dispensed through a nozzle in a molten form. The molten material falls into a movable built platform and is solidified. This process is iterated layer-by-layer until the desired 3D part is created	- Widely used for fast and low-cost prototyping - Broad range of materials can be used for ME ranging from polymers to plastics and composites.	[32], [33]

Table 1:- The seven AM processes and its advantages

1.2 Laser Powder Bed fusion

Powder Bed fusion technologies have been quite versatile, innovative, and rapidly developing both for research and commercial purposes in advanced manufacturing industries. Figure 3. is a schematic illustration of the L-PBF process.

All PBF processes share a similar component: (1) A built platform (2) A powder reservoir where fresh powder is stored and dispensed on the build platform (3) A recoater blade to spread the powder layer, and (4) a heat source such as a laser or electron beam. The powder layer is melted selectively by the heat source, in a layer wise fashion according to the part designed in the CAD software. After the creation of one layer, the build platform lowers and a new powder layer is spread. This process continues until the required 3D part is fully created[23], [34], [35]. The build chamber is protected with inert gas such as argon to avoid oxidation, which happens when the powder such as titanium and magnesium are exposed to oxygen at high temperatures[35].

Powder Bed Fusion uses either a sintering or a melting process. It can be classified by the following techniques [36]:- [31]

- Selective Laser Sintering(SLS):-
- Electron Beam Method (EBM):-
- Selective Laser Melting (SLM):-
- Direct Laser Metal Sintering:- (DLMS)

The difference in these techniques is that in sintering the particles of the powder melt partially and bond but not homogeneously vs in melting techniques the particles are fused together completely by fully melting and rapidly solidifying. In this study we are focusing on SLM due to its high precision and compatibility with building complex geometries[37].

Due to its ability of precision melting with high efficiency, laser is one of the most important components in L-PBF. The Laser type and its intensity are quite important in determining the speed of the build or the time of print and is also an essential process parameter that determines the quality of the L-PBF produced part. The most widely used lasers are either CO2, Nd: YAG or diode and fiber lasers. CO2 lasers is the most common type of laser used. It is quite economical with good beam quality and high output power however Nd:YAG is said to be better suited as it is better absorbed by metallic powders[38], [39].

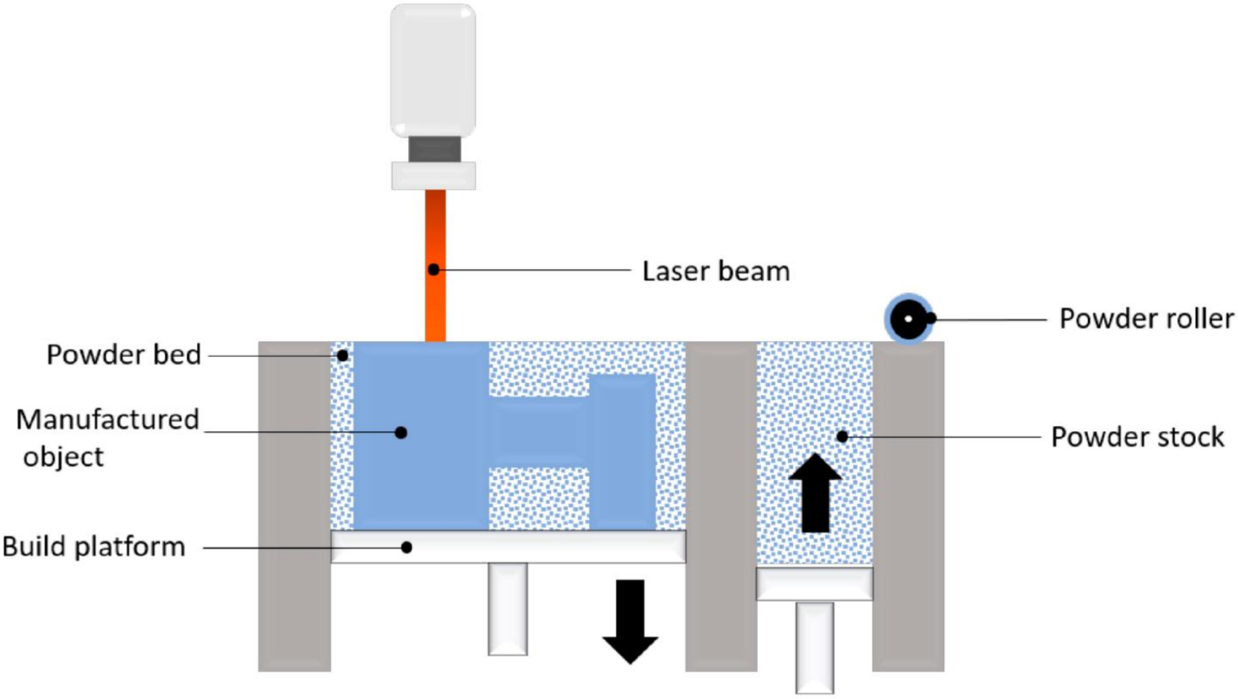

Figure 3 Diagram of L_PBF process, reused from [35].

Processing Parameters

Due to LPBF being a complex process in nature, the manufacturing process of a part involve interactions between its process parameters, and they can impact the functionality, performance, and quality of the final fabricated product., [34]. The individual parameters are laser power (P), scanning speed (v), hatch spacing(h), and layer thickness (t), and the combination of these process parameters affects the laser energy density, which in turn influences the heat transfer and grain growth needed for densification of molten tracks in the L-PBF process[40]. The laser energy density is calculated by the formula

$$\epsilon_d = \frac{P}{u \cdot h \cdot d} \tag{1}$$

Where ϵ_d is the energy density of the laser (J/mm^3), u is the scanning speed, h is the hatch spacing, and d is the layer thickness. Hatch spacing is the distance between two adjacent scan tracks measured from their centers, while layer thickness is the height of a powder layer when spread on the powder bed and then melted Fig 4. illustrates the concept of hatch spacing and layer thickness. There have been several experiments to determine the effect of process parameters on the thermal, mechanical, and microstructural properties of a material.

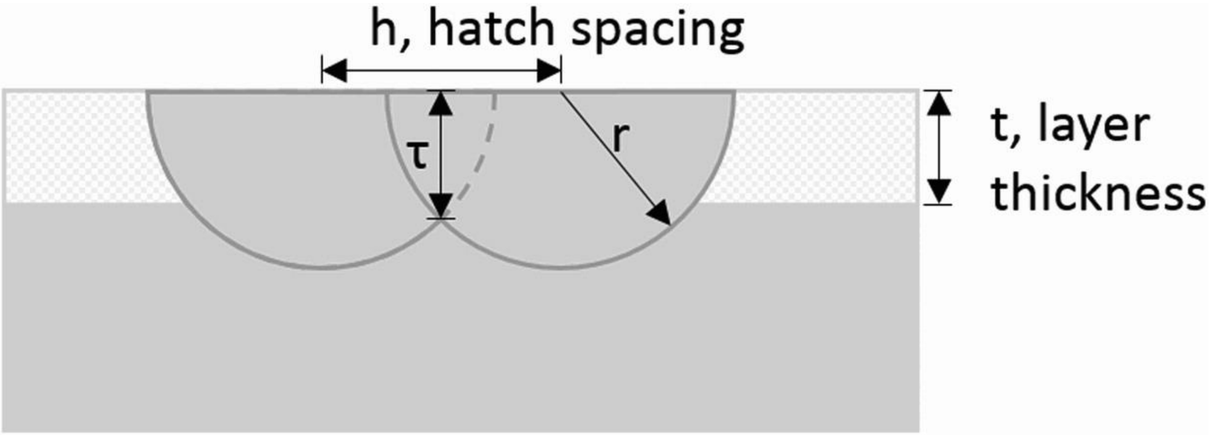

Figure 4 represents hatch spacing (h) and layer thickness (t). Cross-section of the melt pool has a radius (r) and an overlapping height (τ) between two melt pools [41]

Saedi et. al [40]conducted a study to check the effects of laser power and scanning speed on $Ni_{50.8}Ti_{49.2}$ alloy. They concluded that proper densification of a part required a combination of high laser power with high scanning speed or low laser power with low scanning speed. Higher energy density also enhanced the texture formation due to solidification in a specific crystallographic axis. Wei et. al [42] observed discontinuous scanning track can cause a non-uniform microstructure of AZ91D particles. Additionally, non-uniform microstructure and poor bonding between particles can be caused due to overlapping regions, which occur when hatch spacing is more than the track width.

Based on the detailed review by Chowdhury et.al[34] Table 3. provides a summary of different process parameters such as laser settings, scanning settings, powder attributes, temperature parameters, and their effects on the L-PBF process.

Process parameters categories	Specific parameters	Effect of the parameters
Laser power	Laser spot size, pulse frequency, and type of laser beam	Determines the energy density and melt pool dynamics. High power leads to higher melt pool penetration
Scanning Settings	Scanning speed, scanning method, hatch spacing	Scanning settings affect the part surface, and can cause residual stress. Scanning method can be changed to improve densification results.
Powder attributes	Powder morphology, PSD and layer thickness	Finer particles and small layer thickness enhance fusion between particles and increase laser penetration. This improves powder flowability and densification. Powder bed density contributes to high thermal conductivity and better mechanical properties of the part
Temperature parameters	Powder bed temperature and Feeding unit temperature.	Powder bed temperature is also influenced by powder morphology and PSD and it varies depending on laser absorptivity of the powder bed.

Table 2 Overview of different process parameters and their effects on the L-PBF process [34]

1.3 Materials in L-PBF

Metal powder materials used in the LPBF process are usually single metals, alloys, and superalloys of materials such as nickel, titanium, aluminium, copper, iron, and various other alloys [43], [44]. They are produced using 5 different techniques, i.e Gas atomization (GA) process, mechanical attrition and alloying, Solid state reduction, Rotating electrode process (REP), and chemical processes. Table 2. highlights the most commonly used materials, their benefits, and applications studied in different industries so far.

The surface texture of a part produced in L-PBF is influenced by powder properties. These properties can be categorised into three groups: **particle morphology, physical properties, and microstructural properties** [45], [46]: -

1. **Particle Morphology**. –

Particle Morphology comprises size, shape, and surface roughness. They contribute to the flowability, packing characteristics, bulk density, and uniformity of particles.

- Particle size: - Uniform particle size ensures even distribution of powder particles on the bed. Excessively fine particles can cause agglomeration, while irregular size affects the surface topography of the particle.
- Particle shape: - Spherical-shaped particles and smooth surfaces contribute to the consistent particle density, reducing interparticle friction and improving the part quality.
- Surface roughness: - Surface roughness affects the flow and fatigue strength of the final part.

2. **Physical Properties**: -

Physical powder properties include density, flowability, and particle size distribution.

- Apparent density: - This is the mass per unit volume of the powder particles, including their spatial arrangement. It influences the packing density, interparticle forces, and agglomeration of powder particles.
- Tap density: - It is the maximum packing density of powder particles when subjected to a mechanical vibration, and it helps determine powder behavior during recoating.
- Flowability: - Improved by reducing Van der Waals forces between particles. An optimal flow can be improved by adding additives such as surfactants or nanoparticles.
- Particle size distribution (PSD): - PSD determines how the powder is distributed on the powder bed and ensures high packing density (PD) of the final part. A balanced mixture of fine and coarse particles can minimize gaps between particles and ensure good flowability and reduced porosity of the particles.

3. **Microstructural properties**: -

- The powder’s microstructure affects the mechanical properties of the build part.
- It is managed by controlling the temperature of the powder bed, reducing thermal gradients and stresses during the manufacturing process. Oxygen and outside contamination must also be controlled to avoid agglomeration.

Metals and alloys	Advantages	Applications	REF
Titanium (Ti) and titanium-based alloys **such as Ti6Al4V, Ti–4.2Fe–6.9Cr (TFC) and Ti–4Fe–6.7Cr–3Al (TFCA)**	Strong mechanical properties, High corrosion resistance, light in weight	Used in biomedical applications such as orthopaedic implants	[34], [47], [48]
Nickel (Ni) and nickel-based alloys such as IN625, IN718, Waspaloy, Vitallium, Ni–Cr and **Ni–Ti alloys**	Excellent mechanical properties, high elasticity and ductility, high tensile strength	Used in aerospace, chemical and petrochemical industries, medical, automotive and metal processing mills	[47], [49]
(Fe) and its alloys such as **316 Stainless steels, Fe–Ni and Fe–Nd–B**	Compatibility with MRI machines making it easier for biomedical use, high biodegradability compared to other materials. low cost and easy to manufacture	Used in automotive, biomedical and aerospace applications and dentistry	[34], [47], [50]
Aluminium (Al) and its alloys such as **Al-Cu/Al-Cu-Mg, Al-Zn-Mg**	Good heat resistance, high tensile strength, good corrosion resistance.	Used in marine applications, and power electronics	[51]

Table 3:- Different types of materials processed in L-PBF and their applications

1.4 Defects found in L-PBF process

The dynamic interplay of processing parameters causes defects to arise at any stage during the L-PBF process and affect the part geometry at a physical or structural scale. These defects can be categorized as: -

- Powder related
- Processing induced
- Post-processing related
- Nanoscale defects
- Equipment-related defects

This study only focuses on minimizing defects caused by process parameters, specifically due to laser power and scanning speed. Therefore, in the next section, we will review some defect types that are directly influenced by these parameters[52].

Common defects found in the L-PBF process

1. Balling: -

Balling is the formation of balls or droplets of metal instead of a smooth layer of molten pool. Poor contact between the melt pool and the powder substrate, combined with high viscosity, enhances surface tension, causing little spherical droplets of a semi-solid and liquid to form instead of a fully liquid melt pool. [34], [52]. Fig 5. gives an illustration of balling for a single powder layer.

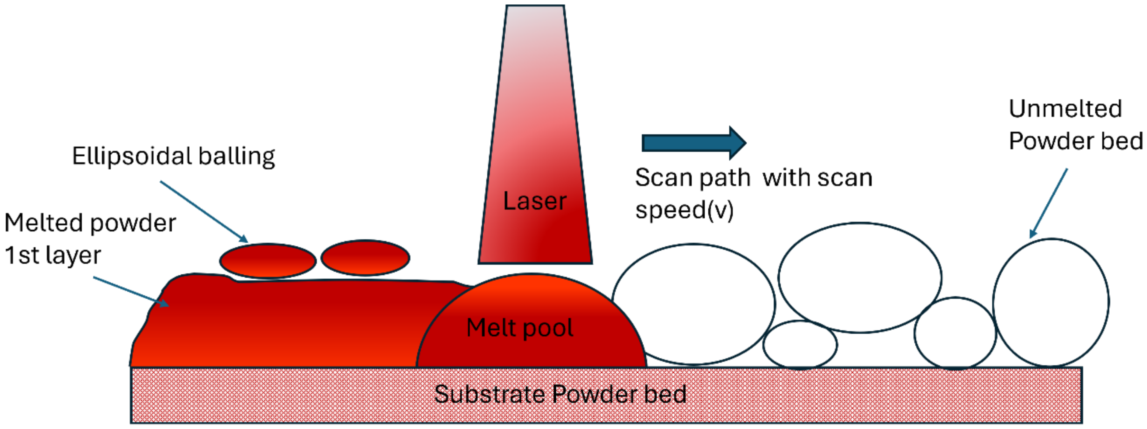

Figure 5 Balling effect (adapted from [53])

Li et.al [54] experimented to observe balling effects on pure nickel (Ni) and 316 L stainless-steel powder for single track, single powder layer, and multiple powder layers. Two types of balling phenomena were observed: ellipsoid and spherical. Ellipsoid balls measured about 500um, whereas the spherical balls were smaller and only measured 10um, hence not affecting the part quality as significantly. On the other hand, ellipsoidal balls caused coarseness and were shown to have hindered the powder recoating process. The influence of different laser power, scan speed, and layer thickness combinations on balling was investigated and can be seen in Fig. 6. A thinner layer thickness incurred decreased balling phenomena and improved wettability as seen in Fig. 6q. whereas in Fig. 6r. scan speed was kept constant at 100m/s and only increased at the intervals of 0.15-0.8 m/s. There is no significant increase in balling except for enlarged pores when the scan speed is 0.8mm. Fig 6s. investigated the effect of balling on increasing laser power. At P= 190 W only a few spherical balls are observed compared to laser power 70 W, which cannot produce continuous scan tracks. Through these observations, it was concluded that the combination of higher laser power (150-190W) and lower or fixed scan speed induced high energy density, which helped reduce balling and improve wettability, resulting in the scan tracks being more continuous. Additionally, increasing the oxygen content in the build atmosphere helped reduce balling.

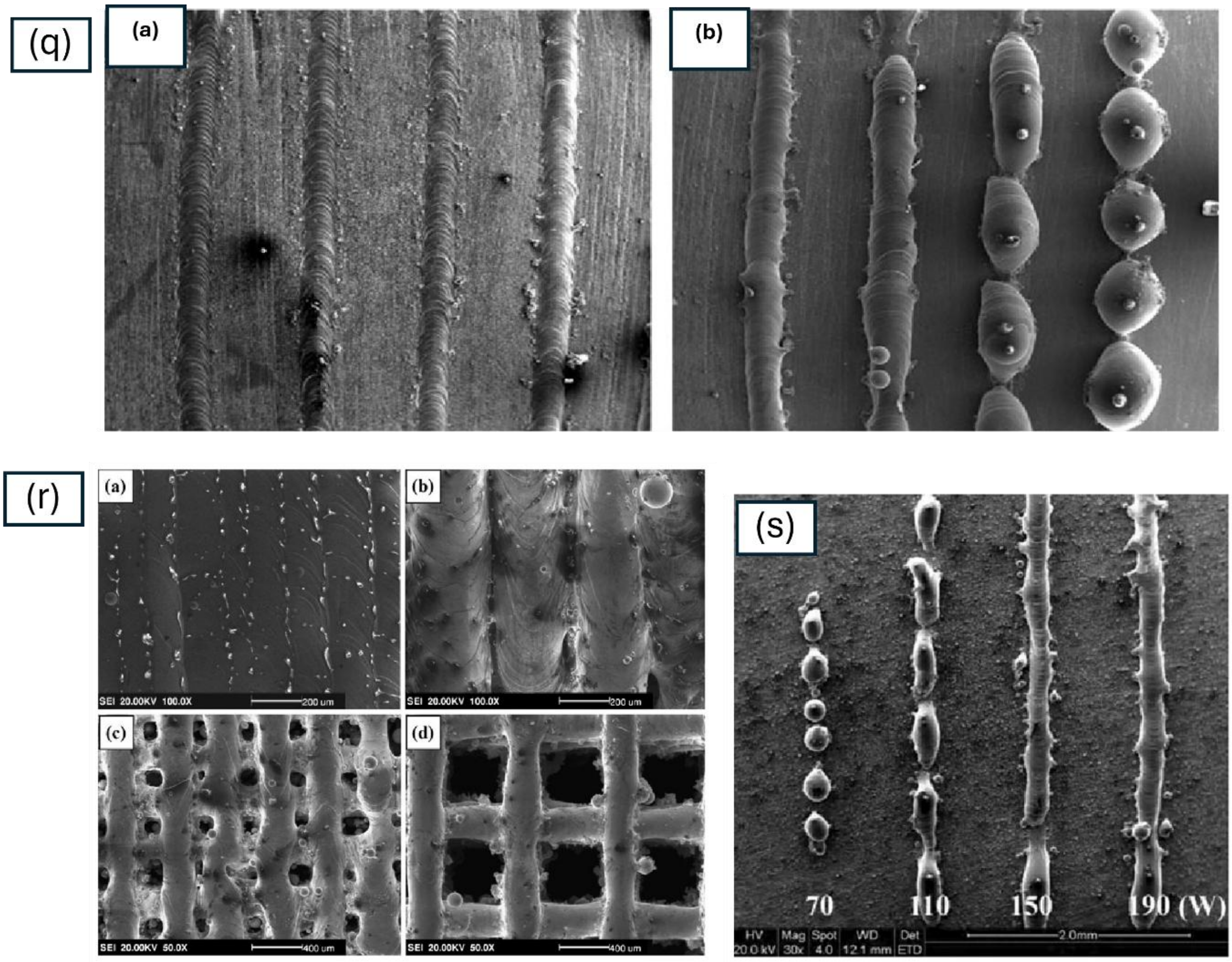

Figure 6. Balling phenomena observed in Ni and 316L powders for different process parameters. (q) Effect of increasing layer thickness: (a) Continuous scan tracks at 0.05 mm layer thickness showing minimal balling; (b) Single continuous scan track at 0.1 mm layer thickness with pronounced balling. (r) Effect of increasing scan speed: (a) 0.15 mm/s, (b) 0.3 mm/s, (c) 0.4 mm/s, (d) 0.8 mm/s. Increased scan speed leads to increase in balling. (s) Effect of increasing laser power: balling observed at 70 W, 90 W, 110 W, and 150 W. Higher laser powers produce more stable melt pools and reduced balling effect. [54].

2. Keyhole Porosity: -

Keyhole porosity is the formation of a deep, narrow void in the melt pool due to the relationship between the laser and material during the L-PBF build process. At high energy densities, recoil pressure arises due to quick vaporization caused by laser fluence. This causes a large amount of vapor depression in the metal at one focal point during fusion between successive layers, causing a hole-like structure to form in the melt pool [55]. Wang et.al [56] studied keyhole pore formation for Ti-6Al-4V powder through Multiphysics simulation. As seen in Fig 7. the results show two phases of keyhole formation. First, there is instant bubble formation caused due to unbalanced forces (combination of drag force, pressure differences, and velocity gradients) on the keyhole wall. Then these bubbles are pinned to the solidification front/base of the melt pool, due to localized evaporation at the keyhole's bottom. The bubbles are unable to escape to the surface due to high-speed drag force. Eventually, this will cause unstable and non-uniform recoil pressure, making the keyhole collapse and finally the formation of keyhole pores.

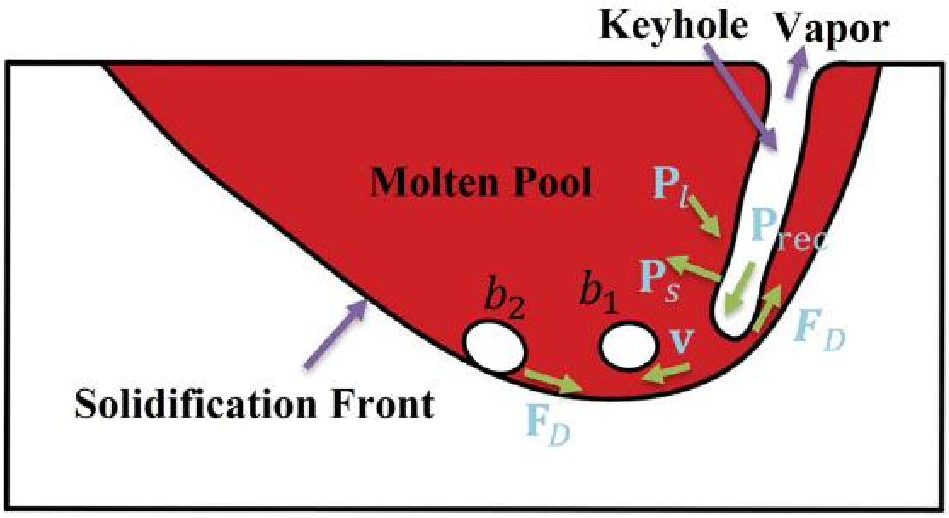

Figure 7 Key hole pore illustration. (P_{rec}) represents recoil pressure, P_l represents pressure due to fluid motion, P_s represents pressure from surface tension, and F_D represents drag force. b1 and b2 are instant bubbles pinned on the solidification front due to keyhole instability [56].

Huang et.al [55] characterized that these key pore formations change based on the area energy densities. The Area energy densities (AED) can be represented as the following formula

$$\text{AED} = \frac{P_l}{v_l\, d_l} \tag{2}$$

where P_l is laser power v_l is scan velocity, and d_l represents laser spot size. As AED increases, keyhole depth increases, meaning laser penetration of the material is too high. Energy density is sensitive to process parameters; hence they need to be adjusted for optimal melt pool formation. High laser power can increase energy density; however, combined with an increase in laser scan velocity and low ambient pressure, can decrease keyhole porosity. [55], [56]. A study conducted by Guo et. al [57] also states that the higher the laser power higher the penetration; however, they can be managed by adjusting laser scanning speed and laser spot size. Adjusting these parameters will decrease energy density, thereby decreasing keyhole pore formation significantly.

3. ***Surface Roughness: -***

Surface roughness in L-PBF is caused due a variety of factors such as process parameter settings, material properties, oxidation by atmospheric gases during build process and powder adhesion. They can be classified into two types: - Top surface roughness and side surface roughness. Side surface roughness occurs due to 'stair stepping effect', which is a phenomenon observed especially in curved surfaces on the build part. It is caused due to various factors such as inclination angle, layer thickness, part orientation and powder adhesion. Top surface roughness on the other hand can be due to other defects such as balling, spattering and overlapping of scan tracks [58], [59].

In some cases, higher scanning speeds can improve some of the surface roughness quality while in some cases, maintaining the scanning speed and increasing the laser power can reduce surface roughness. Additionally, reducing hatch spacing plays an important role in preventing overlapping tracks, thus reducing surface roughness. In conclusion, it is crucial to strike a balance between various process parameters to keep the top surface roughness and side surface roughness minimized [25], [26],[58]. Although surface roughness cannot be completely eradicated by managing processing parameters only, as the fabricated part will need some post-processing methods to produce the desired surface. Yildiz et.al [60] concluded in his experiments that rough or fine polishing of the surface during post-processing can improve the quality of the part without compromising the strength of the material.

4. ***Cracking (due to residual stress)***:-

Due to thermal expansions and contractions of a material increase in thermal strains and stress can occur. This accumulates high residual stresses in the material, causing deformation, fatigue, and crack initiation. Thermal stress is caused due to uneven heating and uneven thermal expansion and shrinkage, while structural stress is caused due to phase transformations in the L-PBF process. When stresses exceed the yield strength, plastic deformation will occur, leaving the solid part with distortions or cracks. Premature cracking can also be triggered due to other defects, such as a lack of fusion or pore formation [61] [62]. Different processing parameters can be tested under tensile loading for optimal material selection and low crack initiation level. Besides that, even higher ductility processing conditions can be utilized for low cyclic stress applications. Lower laser power can improve the cooling rate during solidification because it produces smaller grains and dendrite cells, which branch the cracking out more, in turn improving fatigue resistance. [62]

5**. *Lack of fusion***: -

These defects look like asymmetrical, elongated pores extending beyond 50 μm as shown in Fig 8. They can be caused due to unmelted powders or insufficient overlap between layers, which can lead to premature initiation to cracking and eventually interfere with the fatigue life of a built part[52], [63] Tang et.al [64] proposed a defect model to predict lack of fusion defect, which highlights proper selection of processing parameters such as the hatch spacing, layer thickness and choosing near optimal melt pool dimensions can help reduce lack of fusion defect. The melt pool needs to be deeper than the layer thickness, and its width should be more than hatch spacing. The proposed equation to predict lack of fusion is

$$\left(\frac{H}{W}\right)^2 + \left(\frac{L}{D}\right)^2 \leq 1 \tag{3}$$

where H and L are process parameters, hatch spacing and layer thickness, respectively. W and D represent melt pool dimensions width and Depth respectively; lastly L is layer thickness. When the correlation between process parameters or melt pool dimensions do not fulfill the given condition lack of fusion is formed. Cacace et.al [65] studied the ranges of optimal energy densities to prevent lack of fusion defects using Monte Carlo simulations. They experimented on a range of hatch spacing and scanning speed combinations for steady power values at P=150 W and P=200W. Parameter combinations with high power gave optimal (low) energy density values to reduce the probability of lack of fusion. The important factor was primarily having high laser power, other parameters and the build rate can fluctuate in small amounts without causing significant lack of fusion defect.

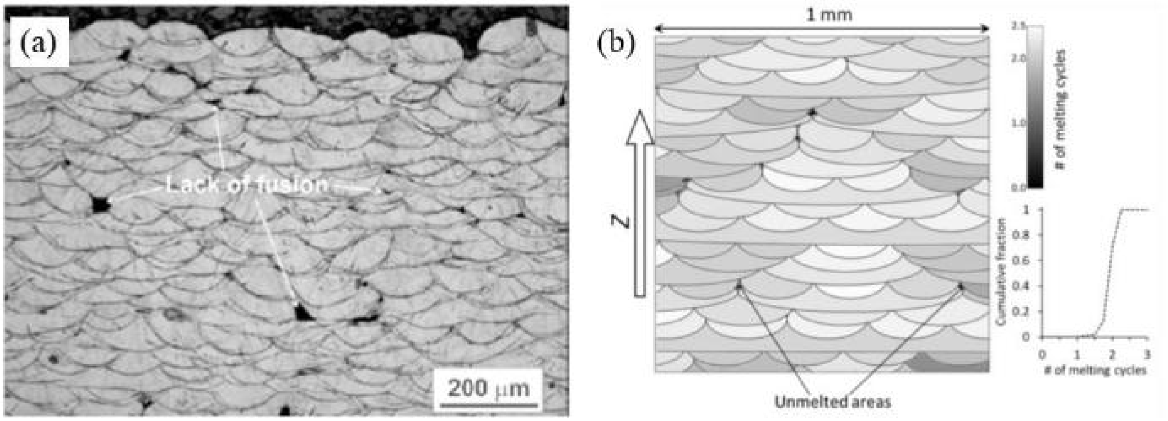

Figure 8 Schematic and optical image of a cross-section of melt pool showing lack of fusion defect [52]

6. ***Spattering***: -

Spattering occurs during laser and metal interaction in the build process when particles are ejected from the melt pool. It forms when a laser beam hits the melt pool and forms a deep depression, causing quick vaporization and the generation of a metal plume. The metal plume applies a force on the rear wall of the melt pool, and droplets of metal are ejected from its surface. There can be two types of spattering: droplet spatter and powder spatter. Droplet spatter, also known as hot spatter, occurs due to an unstable melt pool caused by recoil pressure. Molten metal is ejected from the melt pool surface in the form of jets and reduced to droplets by metal vapor because of the Marangoni effect, driven by surface tension gradients. Furthermore, powder spatter, also known as cold spatter, arises when unmelted powder particles around the melt pool are ejected because it gets swept along with protective gas flow and the impact of metal vapor [66] [67]. Fig 9. represents the schematic diagram of spattering showing the occurrence of both powder and droplet spatter.

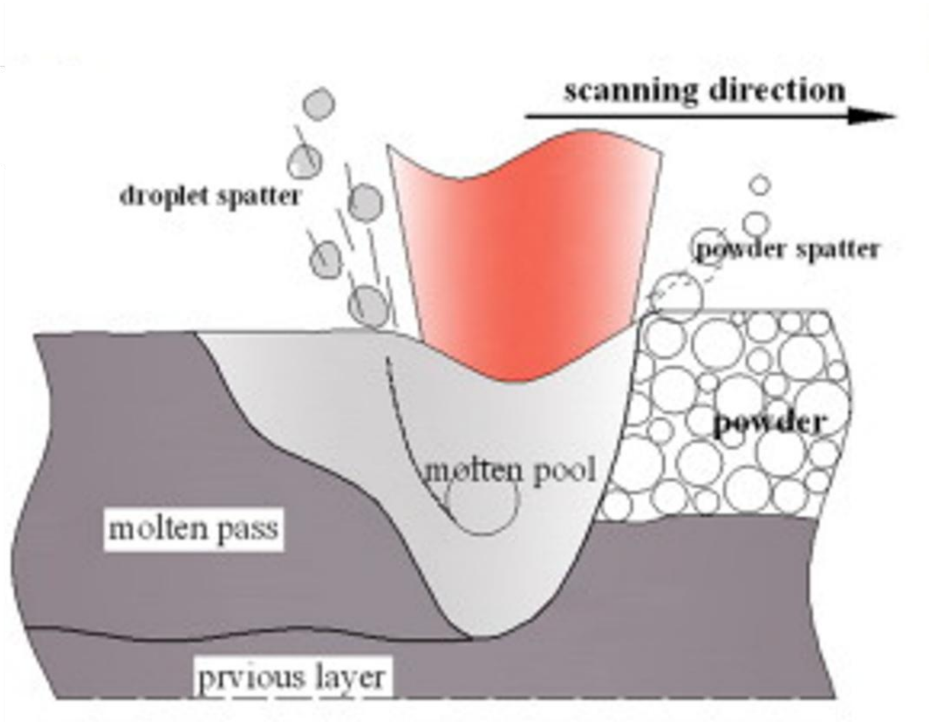

Figure 9 Schematic diagram of Spattering [67]

Spatter is technically unpreventable in L-PBF as it is a byproduct of the process; however it may be reduced to an extent by controlling process parameters[66]. Multiple parameters such as Laser power, scanning velocity, laser spot diameter, and layer thickness, affect spattering. Chen et.al.[68] found that high laser power can increase spatter and it can be managed by keeping the melt pool temperature between melting and boiling points. To achieve this, it is important to regulate the laser power, adjust the energy density, and ensure the laser beam is evenly distributed. Alternatively, Luo, et.al [69] demonstrated that if laser power is higher than 150 W, spatter can be significantly reduced due to the melt pool being deep enough and well penetrated. For scanning speed, the effects are different on cold and hot spatter. Higher scanning speeds may help reduce hot spatter, but it can increase cold spatter. In regards to laser spot size, the bigger the spot diameter, the more spatter is suppressed as it stabilizes the melt pool. Lastly, when it comes to layer thickness, the spatter reduces when the layer size is twice of the powder particle diameter, as it improves the melt pool stability and improves heat dissipation[66]

1.5 Analysing L-PBF using FEM

Finite element method (FEM) is a type of numerical method used to compute physical and mathematical problems that depend on a finite set of parameters. It is more useful than other analytical methods, which are generalizations of reality and are only applicable in a few situations in real-time. A mesh of finite elements discretizes a structure and helps in the visualization of any mathematical model, making it easier to analyze the structure and study its physics, such as stresses involved, thermal analysis, flows, and other unknown patterns[70]. Due to benefits such as ease of simulation, decreased computational time, FEM is a desirable, a high-fidelity simulation method and an excellent alternative to real-time L-PBF printing process, especially in research contexts.[71].

FEM is based on fundamental equations of heat transfer and solid mechanics equations to study thermal and structural responses in materials.

Thermal Analysis

During thermal analysis, the heat transfer emerging from powder-laser interaction is studied. Consider the temperature of an object is $T(x, y, z, t)$at given position (x,y,z) at time t.Then the governing heat conduction equation is given as [72]:-

$$\frac{\partial T}{\partial t} - \frac{\lambda}{c\rho}\nabla^2 T = \frac{W}{c\rho} \tag{4}$$

Where: - $\rho = \ density\ of\ the\ object$ $\lambda =$ thermal conductivity

$c = \ specific\ capacity$ $W = \ heat\ source\ intensity$

Furthermore, The three boundary conditions applicable to equation (4) are:-

a. temperature distribution over objects surface for all time instances.

b. The heat flux density normal to the object at any point and

c. convection and conduction conditions along any point of the object's boundary.

They are expressed as the equation: -

$$-\lambda\frac{\partial T}{\partial n} = -q + \gamma\left(T - T_f\right) \tag{5}$$

Where: -

$T = \ ambient\ temperture$

$\gamma = the\ coefficient\ of\ heat\ exchange$

$\frac{\partial T}{\partial t} = \ directional\ derivative\ along\ surface\ normal\ indicates\ rate\ of\ temperature\ change$

$q = \ heat\ flux$

The initial temperature distribution of the object at t=0 is given by the equation

$$(T)_{t=0} = f(x, y, z) \tag{6}$$

Mechanical analysis

The temperature field $T(x, y, z, t)$ from equation 4is applied as a temperature load to the mechanical model. This thermal load induces thermal strains, leading to stresses and deformations due to thermal expansion and contraction of the material [73].

Some of the important governing equations for mechanical analysis are summarised below Equation (7) gives the governing equation of mechanical equilibrium, which states that internal and external stresses must balance out [73].

$$\nabla\boldsymbol{\sigma} + \boldsymbol{F_v} = 0 \tag{7}$$

Where $\boldsymbol{\sigma} =$ cauchy stress tensor $\quad \boldsymbol{F_v} = body\ force\ per\ unit\ volume$

The stress-strain relationship is given by the Cauchy stress-strain formula

$$\boldsymbol{\sigma} = C\colon\boldsymbol{\varepsilon} \tag{8}$$

Where $\boldsymbol{\varepsilon} = total\ strain$

The total strain is further divided into 3 components

$$\varepsilon = \varepsilon_e + \varepsilon_p + \varepsilon_{th} \tag{9}$$

Where $\boldsymbol{\varepsilon_p} = plastic\ strain \quad \boldsymbol{\varepsilon_{th}} = thermal\ strain$

Several researchers have employed FEM based models to study different aspects of the L-PBF process and conduct thermal and mechanical analysis of materials under various conditions. Ullah et.al [73] used FEM software Abaqus to study melt pool dimensions and predict geometric distortions for AlSi10Mg powder. He validated melt pool dimensions by simulating it in Abaqus using a double ellipsoid Goldak heat source model. Song et.al [71] simulated the entire L-PBF process using the AM module in Abaqus and compared the simulated residual stress values to XRD results.

1.6 Importance of in-situ process monitoring techniques

So far, we have established how crucial the relationship between process parameters is and the effect of it on the melt pool. This highlights the need for process monitoring to closely observe and control these parameters. Process monitoring can be performed both in situ (during the build process) and well as ex situ (post-mortem analysis after the build process). In Situ measurements can be categorized into five levels as explained in Table 4 . [74]

Monitoring levels	Monitoring process	Monitoring parameters
Level 0	Measurements are done using embedded sensors to take care of the operating conditions of the process and detect anomalies or unstable conditions	Operating parameters of the machine, such as pressure in the chamber, external temperature, oxygen content, signals from motors, inert gas flow, build plate temperature, and installed filter conditions,

Level 1	Measurements are done in the build area once or more per layer.	Ensuring uniform powder distribution, preventing powder bed contamination, checking dimensional accuracy, and surface topography
Level 2	Monitoring beam and powder bed interaction on the current layer	Thermal history and other defects forming as by-products
Level 3	Monitoring beam material interaction and fusion of the particles i.e. melt pool	Melt pool geometry and temperature distribution
Level 4	Monitoring interacting between layers	Gather information under the currently processed layer through X- ray images, ultrasonic and acoustic emissions

Table 4 Five levels of in situ level monitoring

In situ monitoring techniques offer a deeper and more precise way to measure process parameters during the LPBF process and help us optimize them in real time. Combining in-situ monitoring with machine learning analysis enables effective management of large amounts of data and optimizes relationships between process parameters and material properties, leading to improved part quality[3]. Furthermore, this can help design control strategies for the minimization of defects or controlling processing conditions. However, in situ monitoring techniques have their challenges when it comes to managing the large size of data, storage of data, and real-time monitoring. For example, X-ray computed tomography (XCT) generates high volumes of data, which compromises its spatial resolution, hence hindering its ability to detect defects. Hence, integration of ML makes it easier and swifter to monitor in-process defects [3], [75].

1.7 Types of Machine Learning in In-Situ Monitoring of L-PBF

For the detection of anomalies in in-situ monitoring, both supervised and unsupervised learning methods have been studied. Supervised learning, such as Convolutional Neural Networks (CNN), Support Vector Machine (SVM), and Multilayer Perception (MLP), along with high-speed cameras or vision sensors, can effectively predict defects such as porosity level, balling, and undermelting, with an accuracy of 90- 92%[3], [76]. Scime et al [77] used computer vision to predict locations of poor build quality and detect unique anomalies due to the scan pattern that wouldn’t have been noticed by conventional methods.

Due to their clustering, dimensionality reduction, feature learning, and detecting outliers, unsupervised learning can be convenient in defect detection, especially when a large amount of data is involved. Unsupervised learning methods such as K-means clustering or Gaussian mixture model (GMM) can detect defects related to hotspots in optical images.[3] [75]. Some more unsupervised techniques, such as Principal Component Analysis (PCA), have also been applied to manage the large data volumes from in situ imaging. In a separate study, Scime et. al [78] used feature extraction techniques such as Scale Invariant Feature Transform (SIFT) and Bag-of-Words (BoW) to enable scale-invariant representations of melt pool appearances, and these unsupervised insights were further used to train a supervised classification model capable of recognizing melt pool types not seen during training. However, supervised learning tends to offer higher predictive accuracy and has been explored in research extensively, likely due to its reliable performance across various applications. Furthermore, Arindam Paul et.al. [79] explored various other ML algorithms such as random forests, XGBoost, Ada boost and ERT to create a closed-loop control system for laser path, speed, and temperature parameters of the DED process. ERT showed the least error in the predictive model as compared to other methods, as it seemed to increase bias and decrease variance. Through this method, he was able to essentially increase the simulation speed and bring real real-time control model for the process.

1.8 Machine learning in Process Optimization and Control

ML is no longer limited to process monitoring and defect detection as new emerging research is moving towards process optimization via smart control strategies. More interest is being shown in analysing/recognising defect patterns and creating a control system that can at least predict adjustments to essential process parameters such as laser power or velocity. This can prevent defect occurrence, hence improving the part consistency as well as increasing productivity and reducing material waste [80]. Yao. Et al[81] made an optimal control policy to manage layer-by-layer defect formation using Markov's decision process. The layer defects were computed using multifractal analysis, which captures a spectrum of irregular patterns in the process. They are quantified using Hotelling T^2 method, which is a multivariate technique shown to represent the defect index of every layer within the build process. Fig 10. depicts the process of the algorithm to take a corrective decision if the defect level exceeds the control limit (purple area) in each layer. A more industry-based control architecture was proposed by Reiff et.al [8]where control systems such as PLC and CNC are integrated with Field programmable gate array (FPGA). An integrated three-dimensional map stored in the PLC controls the relationship between process parameters, and this was controlled in real time using a Gaussian Radial basis (RBF) network. The simulation results in this case showed a 48% reduction in powder bed temperature. Masinelli et al[82]. recently proposed the use of reinforcement learning (RL) to control defects by tracing their propagation through acoustic emission (AE) signals. More research is needed in this field as it is still largely unexplored.

1.9 Reinforcement Learning in a Control Policy

Reinforcement learning has attracted increasing attention for its potential learning to monitor and optimize process outcomes. Due to its ability to learn iteratively, it functions as an ideal feedback mechanism for the monitored process. In this way, we not only monitor/detect defects while processing we can also possibly train the processes to take their own corrective measures, basically making the algorithms self-learning [82] [3].. But what is Reinforcement learning? We know, Supervised learning has labels or training set and the algorithm has to categorize the data based on previously trained data, while in unsupervised learning, the data is unlabeled so the algorithm uses pattern recognition, cluster formation and classification However, in Reinforcement learning, the algorithm tries to maximize its reward signal based on the learning experience from its environment. It works more like semi-supervised learning, as there is no predefined data[10]

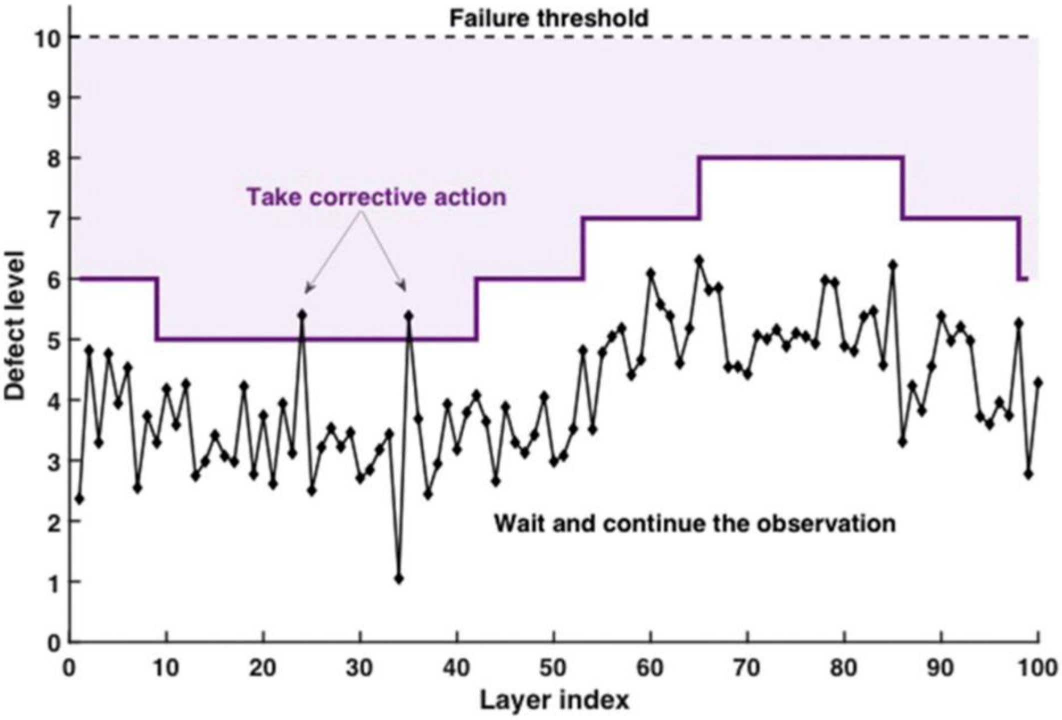

Figure 10 control policy action by Yao et.al [81]

To maximise rewards, a reinforcement learning agent should favour actions that it has learned to be successful from previous experiences. However, to identify these successful actions, it must also explore previously unchosen actions. Once the agent learns the actions that yield the highest rewards, it tends to exploit them to maximise future rewards. However, it must also explore other actions in order to make better long-term decisions and discover potentially better strategies. It is sort of similar to a human brain, which tends to learn from experience and has to explore actions they have not used before to get better results. Interaction is involved between active decision-making agents and their environments, where the agent will achieve a goal despite the uncertainty in its environment. Decisions are based on what the algorithm has already experienced using exploration and exploitation.[10] Reinforcement learning has been tested or implemented successfully in a few games, such as tic-tac-toe, or the Go game. There are various reinforcement learning methods, such as epsilon greedy, Q learning, or Proximal policy optimization (PPO), and extensive research is ongoing to implement this for L-PBF process optimization. Francis Ogoke et. al [12]was able to create a control policy using PPO to optimize power and velocity process parameters and maintain melt pool depth for single-layer deposition using different scan trajectories. Dharmadhikari et.al. [7] used Q learning method to find optimal P-V parameters to maintain a steady-state melt pool depth. Wasmer et al.[83] established the viability of using acoustic emission (AE) signals combined with reinforcement learning and CNNs for in situ defect detection in L-PBF. Their system accurately classified build quality based on AE patterns, enabling real-time monitoring of porosity-related defects.

1.10 Role of melt pool and Importance of Melt pool monitoring

A melt pool is generated when a laser scans across the powder bed, causing molten metal to form. The melting and bonding of powder involve various physical and thermal phenomena. The physical processes, such as surface tension, recoil pressure, gravitational forces, and capillary movement at melt pool boundaries, can cause the melt pool to change its shape and size. While thermal processes such as the heating effect, Marangoni effect, and heat transfer that occur during laser and powder interaction affect the melt pool stability and solidification.[32]

Melt pool dimensions and geometry are a reflection of the interaction between process parameters, scanning path, laser power, powder feedstock, material phase transitions, and flow phenomena of the material during the build process. This complex interplay between these factors facilitates the melt pool melting mode, which will influence how solid solid-liquid interface moves during the solidification process. These melting modes then affect the microstructures and defect formation in the melt pool. [34], [84]

There are two melting modes described, keyhole mode and conduction mode, and they occur during high laser energy density and low laser energy density, respectively. Due to heat conducting downwards in conduction mode, a shallow and wide bowl-like shape of melt pool is created, and the solid-liquid interface migrates in the direction of the printing process. This creates less spatter, fewer defects, and a smooth, stable melt pool. On the contrary, in keyhole mode, due to high energy density, the material vaporises, creating a deep hollow cavity due to high laser penetration and multiple internal reflections inside the cavity. The solid-liquid boundary in this case conducts laterally as the melt pool solidifies. This kind of melting mode can create more instability and is quite risky, but also suitable for denser parts.[84]

Melt pool shape and microstructural characteristics, such as grain geometry, size, orientation, and phase dispersion, are closely interrelated and dependent on each other, and accurate prediction of these characteristics is important for controlling large-scale part properties, such as its mechanical properties. Thermal conductivity, heat transfer conditions, solidus temperature, and nature of liquid flow influence solidification behavior and microstructural evolution of a material. [84], [85]

The melt pool consists of three distinct zones: The topmost zone, called the deposition zone (DZ), the underlying remelting zone (RZ), and the heat-affected zone (HAZ) at the base, and their measured microhardness follows the order $\mathrm{HV_{DZ}} = \mathrm{HV_{RZ}} > \mathrm{HV_{HAZ}}$ (HV stands for Vickers Hardness test)[84] [86]. A study conducted on Ti-6Al-4V by Yang et.al [86]on these three distinct zones of the melt pool show the effect of rapid solidification of molten metal. Temperature gradient (G) and solidification rate (R), which determine the grain structure and dimensions, are interconnected to each other by different combinations of “G*R and G/R”. A high G*R causes finer microstructures, while a high G/R causes coarser grain formation. As seen in Fig 11. the grain morphology (cellular, Planar, equiaxed, and columnar dendritic) is determined by this (G) and (R) relationship.

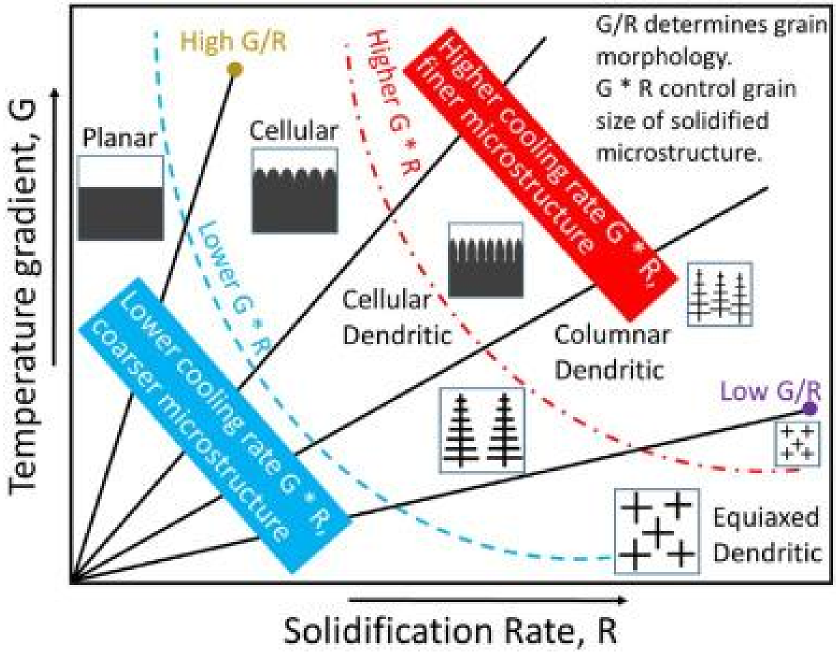

Figure 11 Impact of temperature gradient and solidification rate on the grain morphology and size of the solidified material [84]

Cooling rate is another important factor in determining grain composition and crystal structure during solid-state phase transformation and also affects melt pool geometry. Rapid cooling leads to acicular martensite (α') formation in alloys, which is said to be a metastable state, while slow cooling leads to the formation of lamellar (α) phases. Microstructural-related problems can also be combated through remelting and reducing scan speed to reduce metastable phases.[84], [85], [86]Inconsistent melt pool geometries give rise to defects mentioned in section 1.4. In our case, the melt pool geometry, especially melt pool depth needs to be measured to be able to control or predict process parameters and find a way to optimize them. There have been many designs and experiments to make process optimization through melt pool geometry using in-situ monitoring, but machine learning is the most favourable method as they can be easier to deploy than some traditional methods which are data subjective and confined to specific material or specific AM processes [3]

2 Materials and methods

The L-PBF process is highly influenced by parameters such as laser power and scan speed, which influence melt pool characteristics and thus the part quality. As shown in the motivation section of Fig 12. the specific goal is to maintain melt pool depth by finding optimal laser power (P) and scanning speed (V) parameters, eventually aiming to reduce waste and enhance productivity by minimizing the occurrence of defects due to deformations such as displacements, residual stresses or warping.

The methodology section presented in fig 12. aims to use simulation-based approaches, supported by machine learning techniques, to develop a control framework that identifies optimal P and V parameters. Flow3D AM simulations are employed to simulate a melt pool for virtual observation and analysis. A powder bed is simulated by using powder properties, particle size distribution, and heat source intensity profile, all specific to our desired material, stainless steel 316L. The post-processing phase provides melt pool depth details, eliminating the need for costly physical experiments. The second step is creating a part-scale simulation using Finite Element Modeling (FEM) through Abaqus. FEM analysis, performed using AM modeler plugin in Abaqus, captures the physical phenomena within the L-PBF process by offering insights into its thermal and mechanical behavior. Through this we were able to evaluate deformations for various laser and scanning combinations. These simulations create a data-rich foundation for further statistical and machine learning analysis.

A key step in our simulation methodology is the application of Response Surface Methodology (RSM) to analyze how laser power and scan speed influence deformations. This statistical approach also served to validate the displacement response obtained from simulations. The core of the control strategy is built around a Reinforcement Learning (RL) algorithm. We use Q learning method, where the agent interacts with a simulated environment and receives feedback in the form of rewards. The agent explores different state action pairs, trying to find the lowest deformation values, gradually converging to the optimal power and velocity value over thousands of episodes. The Q learning agent acts as a control system that learns to choose process parameters that minimize part deformation and maintain melt pool stability.

The future work as mentioned in fig 12. could focus on automating and testing control strategies directly within Abaqus, and integrating them with actual L-PBF experiments for more real-time feedback and validation. This would enable active control and immediate feedback to adjust parameters on the fly, improving process reliability and reducing defects.

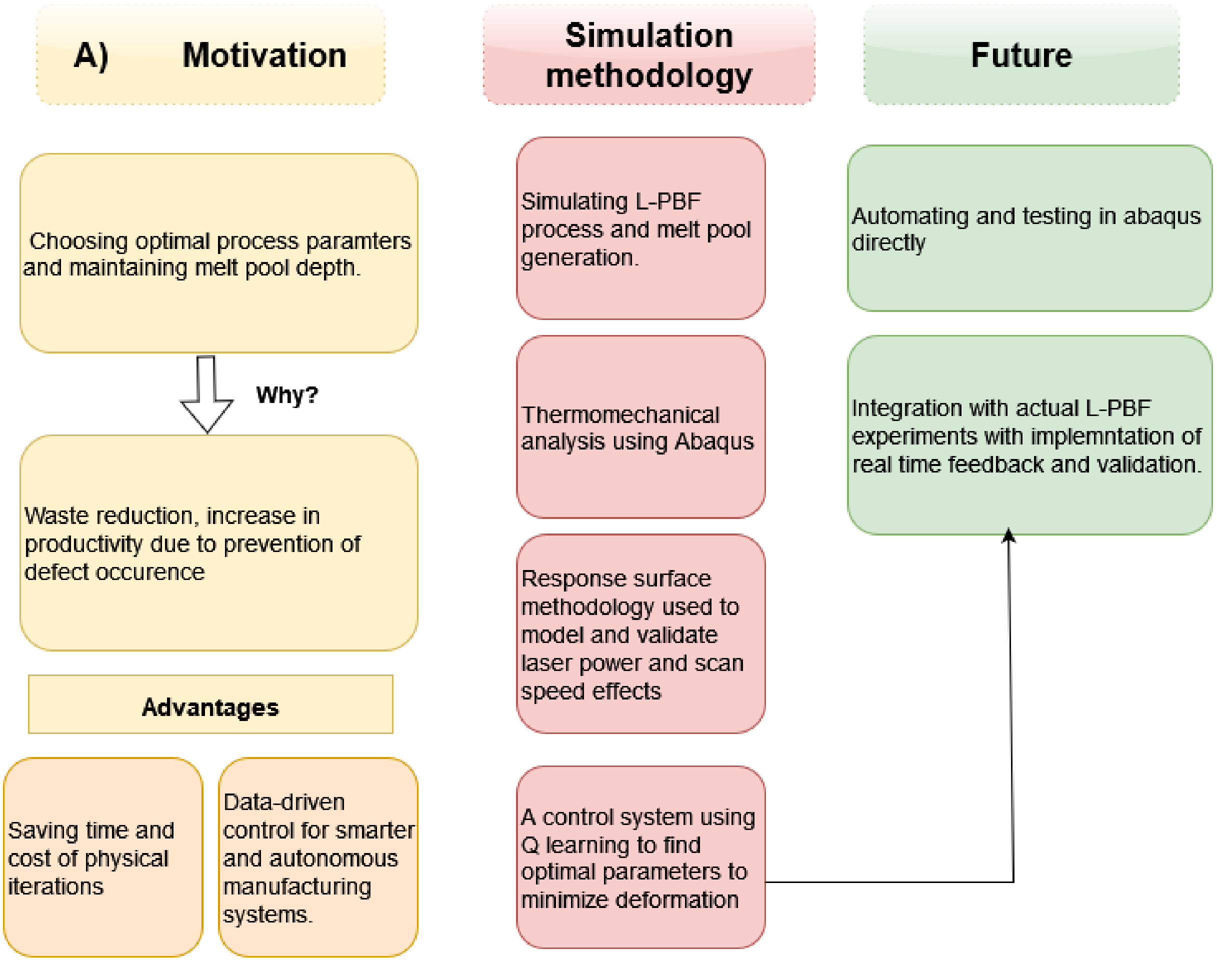

Figure 12 Motivation, method, and future application of the thesis

2.1 SS 316L powder material

SS316L is an alloy of Fe and due to its excellent mechanical properties, corrosion-resistant behaviour, and improved tensile strength, it is one of the most popular materials in additive-manufactured parts for energy, biomedical, and various other industries, as mentioned in Table 2 (section 1.3). Extensive research has been conducted by researchers on its microstructural and mechanical properties, the effect of corrosion, and process parameter optimization. Fig 13 shows Fe and Fe alloys account for 32.3% of research studies among other powder materials used in L-PBF[47]. A study provided by Chaudry et.al [87] investigated heat accumulation on SS316L parts using FEM, which may be employed further in the optimization of process parameters to mitigate the said heat accumulation.

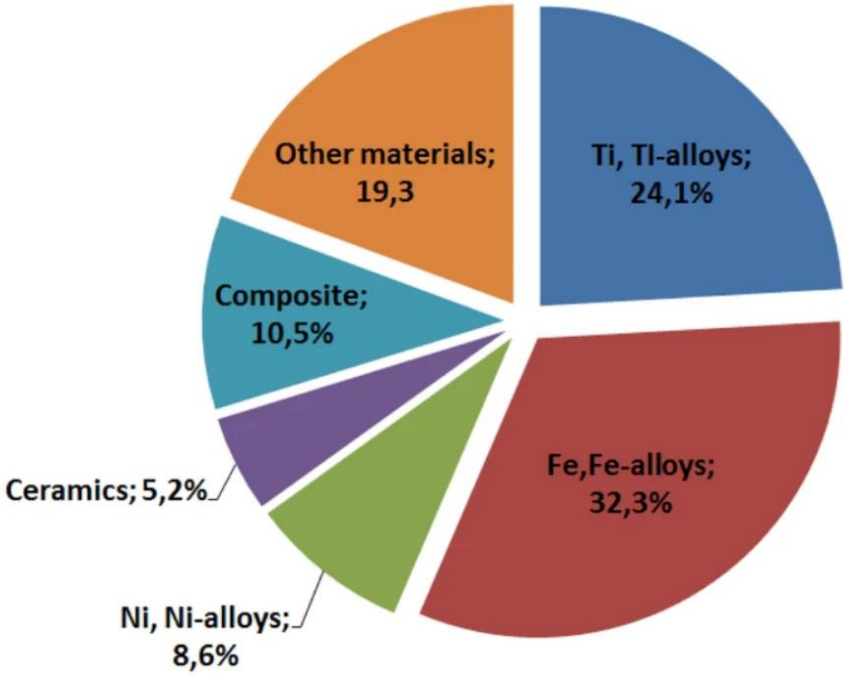

Figure 13 Pie chart for the percentage of Research published for different powder types used in L-PBF[47]

2.2 Building melt pool using Flow 3D AM

About Flow 3D

FLOW-3D is a Computational fluid dynamics (CFD) software platform developed by Flow Science Inc. (USA), and it is specialised in solving thermo-fluid behaviour in L-PBF, enabling modelling of fluid flow, heat transfer, and phase change phenomena[88]. In this thesis, we use Flow 3D AM due to its near-accurate prediction of melt pool dynamics. Haapa [2] was able to successfully simulate powder bed for IN718 with 52% accuracy, hence we know that through predictive modelling in this software, it is possible to develop a fundamental insight into melt pool behaviour within the powder bed.

Modelling in DEM

The powder bed was generated with the base FLOW-3D software along with the DEM module. The DEM module is modelled based on the Lagrangian particle model and describes how discrete particles interact with each other, as well as with fluid, void, and boundary. While real particles can be non-spherical and elongated to reduce complexities, we consider our particles to be idealised solid spheres with some mass. There are several things to consider when particles interact with each other, such as their viscoelastic behaviour (using Voigt Linear Spring dashpot), interparticle friction (Coulomb friction coefficient, static and sliding friction), particle-wall friction, and adhesion. [85]

The DEM module allows users to specify dynamic and static friction coefficients as well as adhesive forces. Particle properties are also configured within the DEM module, including parameters such as density, coefficient of restitution, particle size, adhesion, and laser spot size.

How DEM models Particle behaviour.

1. **Contact Force**

Consider two particles i and j in contact; the total translational force (gravitational, tangential, and normal) exerted on the particle is given by [88]:-.

$$m_i \frac{dui}{dt} = \sum_{j\neq i}\left(\boldsymbol{Fij}^n + \boldsymbol{Fij}^t + \boldsymbol{F}_{ij}^{a}\right) + \boldsymbol{F}_i^{B} \qquad (10)$$

The rotational force is defined as $I_i \frac{d\omega i}{dt} = \sum_{j\neq i}(\boldsymbol{M}^t ij + \boldsymbol{M}^r ij)$ (11)

where $\boldsymbol{M}^t = torque\ due\ to\ tangential\ force$

and $\boldsymbol{M}^r = torque\ due\ to\ rolling\ resistance.$

And to capture elastic deformation and energy dissipation, we use the Voigt Linear Spring dashpot model. The normal contact forces can be denoted as: -

$$\boldsymbol{Fij}^n = [\![-k_n \delta ij^n nij - \eta_{nu} ij^n,\ \delta\_\{ij\}\textasciicircum n > 0$$

$$0, \qquad\qquad otherwise]\!]$$

Where the damping coefficient is $\eta_n = \frac{2\ln e_n\sqrt{m_{ij}k_n}}{\pi^2+(\ln e_n)^2}$ (12)

and k is spring constant.

(details and definitions of all variables can be found in nomenclature).

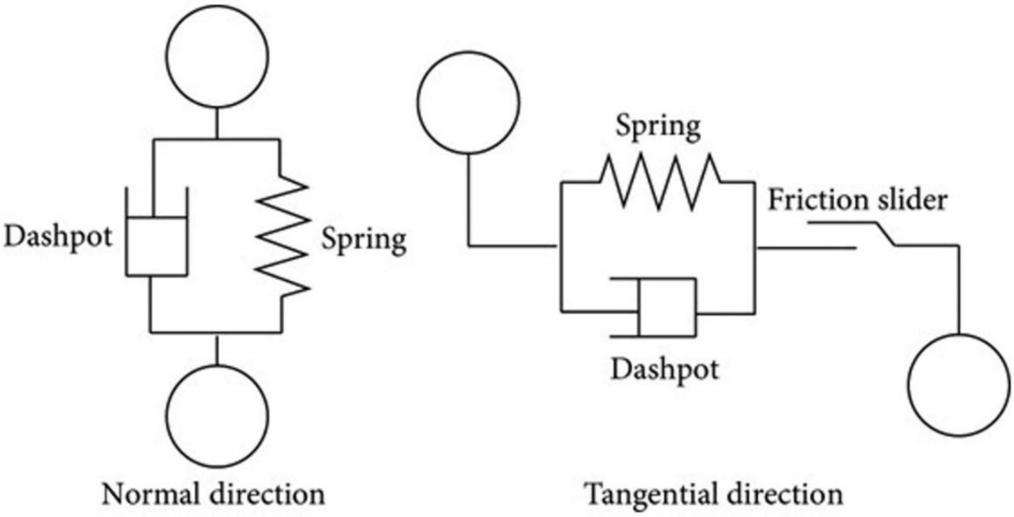

Figure 14 Voigt dashpot model in normal and tangential direction used in DEM simulation [89]

This Fij^{n} contact forces can be divided further in tangential and normal direction defined using coefficient of restitution (e) as shown in Fig 14.[2], [89]

2. Contact Detection and Modelling

To define the resolution of the model meshing process is important. In DEM simulations, the simulation area is divided into mesh cells, where the cell size must be greater than the maximum particle size. Similarly, to capture fine geometric details, a finer mesh than the geometric features is required. The way it works is that at a given time step, each particle only checks for contact with other particles in the closest neighbouring cells from its own cell. FLOW-3D uses ISEARCHOPT=0, which is a position-based exploration technique and searches the particles based on index-based proximity. ISEARCHOPT=1 is another technique based on cell index search-based technique. FAVOR is another vastly used numerical method used to represent geometry in a computational grid by occupying a fraction of each cell/face. Mesh boundaries require assigned boundary conditions, which define how particles interact with edges [2], [88], [90].

Once the contact is detected, contact modelling occurs where the rebound velocity and direction of particle-particle and particle-wall interaction are dependent on the degree and orientation of their overlap, the stored elastic force, and energy dissipated through viscous damping. The overlap represents how particles deform and is influenced by the Young's Modulus E and the spring constant k, depending on which type of contact model is used. The overlaps happen at dimensions measured in nanometers; therefore, the simulations only take short time steps to capture contact events. The overlap should not exceed 0.1–0.5% of the radius of the largest particle is recommended to improve computational efficiency. [2], [91].

3. Parametrisation

The necessary input parameters are determined by the type of contact modelling and the intricacy of the contact model. Some of the user-defined inputs are elastic forces that are represented by a spring constant k [N/m]. Friction is characterized by static and dynamic coefficients for both particle–particle μ_{Spp}, , μ_{Dpp} and particle–wall μ_{Spw}, μ_{Dpw} interactions. Adhesive behaviour between particles is represented using surface energy (SE) in [J/m²]. Particle size distribution and density are also included. Studies suggest a further calibration and validation of the powder bed using qualitative or quantitative methods, but it was not feasible in this scope of work. Therefore, most of the input parameters and SS316L powder properties we will need to simulate the powder bed are obtained from peer-reviewed sources to ensure physical realism. [2]

Particle input parameters and chemical composition of SS316L

The chemical composition of our powder material is as follows:.-[92]

Element	**Fe**	**Cr**	**Ni**	**Mo**	**Mn**	**Si**	**C**	**N**	**P**	**S**
Wt (%)	Bal	16.0–18.0	10.0–14.0	2.0–3.0	2.0	0.750	0.030	0.100	0.045	0.030

Table 5 Chemical composition of 316L used in this study.

*μ_{spw} = Static friction Coefficient particle wall #μ_{Spp} = Static friction Coefficient particle particle
#μ_{Dpp} = Static friction Coefficient particle particle * μ_{Dpw} =dynamic friction coefficient particle wall
Rolling and sliding friction is considered instead of static and dynamic friction, as found in literature

Parameters	**Symbol**	**Unit**	**Value**	**Ref**
Restitution coefficient	e	-	0.64	[93]
Spring constant	k	N/m2		
***Coefficient of friction (particle wall)**	* μ_{Spw}	-	0.2	[94]
***Coefficient of friction- (particle wall)**	* μ_{Dpw}	-	0.18	[94]
***Coefficient of friction particle- (particle- particle)**	#μ_{Spp}	-	0.09	[93]
***Coefficient of friction particle (particle- particle)**	#μ_{Dpp}	-	0.6	[93]
Adhesion	SE	J/m^2	0.001	[93]
Particle size range	-	µm	10-70 µm for coarse and 1-20 µm for fine particles	[2], [92]
Angle of internal friction (AIF)	φ (◦)	-	28.6	[95]
Bulk density	ρ	kg/cm³	7960	[92]
Viscosity	-	kgms−1	7 × 10−3	[90]
Powder layer thickness	-	µm	30	
Absorptivity	-	-	30%	[92]

Table 6 Particle and simulation parameters of SS316L used in Flow 3D AM simulations

Particle size distribution

The sizes of powder particles used in L-PBF are commonly in the range of 10-70 µm for coarse particles and 1-20 µm for very fine particles[2], [92]. The part performance depends on the size and shape of the particles as well as their flow and densification abilities. The aspect ratio of the particles matters too because larger spherical particles flow more than smaller ones, while smaller particles dissolve faster than the larger ones. Optimizing PSD is said to improve processing speed, surface roughness, and dimensional accuracy according to many studies[2], [96] The Powder size distribution is often described on the normal distribution as shown in Fig. 15. as D10, D50, and D90. These are percentile values that give a statistical representation of how fine or coarse the powder is. D50 or the median, refers to the particle diameter where 50% of the particle population is smaller than this value. D10 is the particle diameter where 10% of the particle population is smaller than. Similarly, 90 percent of the particle population lies below the D90 particle diameter. D10 has the finest particle diameters in the distribution, while D10 has the coarsest [88], [96].

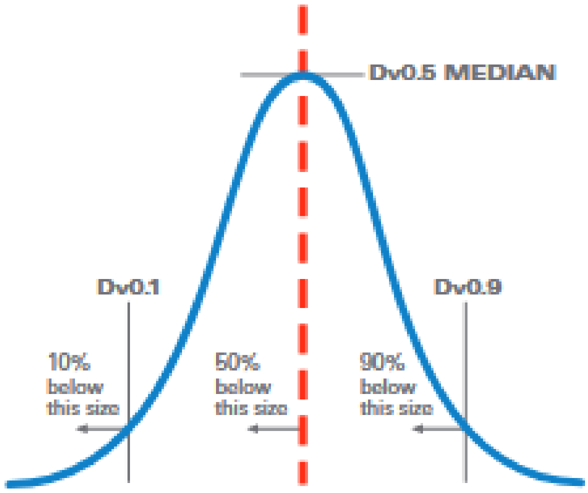

Figure 15 PSD described in literature. D10 refers to 10% particles are very fine have small diameter than this size. D50 is the median where 50% particle diameter is smaller than this size and they may be medium sized, D90 means 90% of the particle diameter fall under this value. [96]

The particle size distribution for SS316L where obtained from literature and the size classes were approximated as D10: 19 µm. D50: 30um and D90: 46um which means our finest particles are below 19 µm and the largest particles are under 46um giving us a fairly balanced distribution.[92], [97]. The graph below is a rough approximation of particle concentration according to size classes.

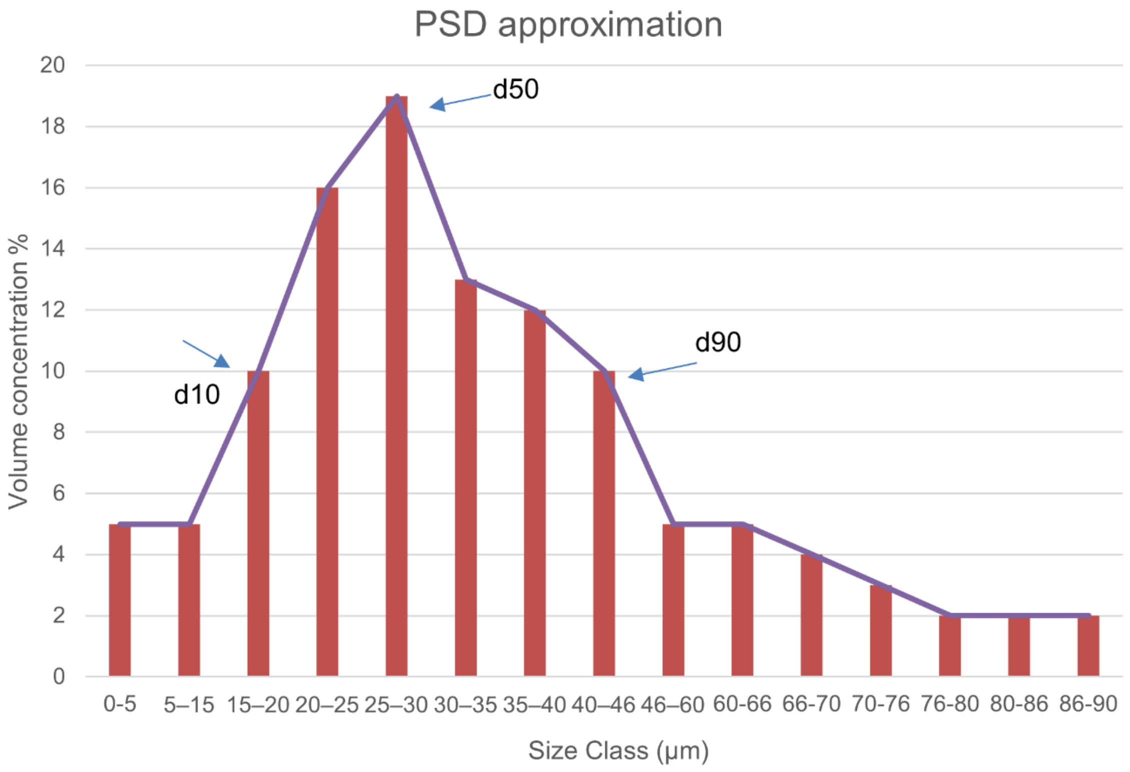

Figure 16 PSD approximation for D10: 19 µm. D50: 30um and D90: 46um[92], [96], [97]

Multiphysics modelling in FLOW-3D

Figure 17 shows the core FLOW-3D software that offers a large selection of physics models and analysis tools that can be integrated into the powder bed simulation. As shown in the simulated powder bed below, the physics chosen are Gravity, Viscosity, Phase changes, Heat transfer, Surface tension, and density evaluation.

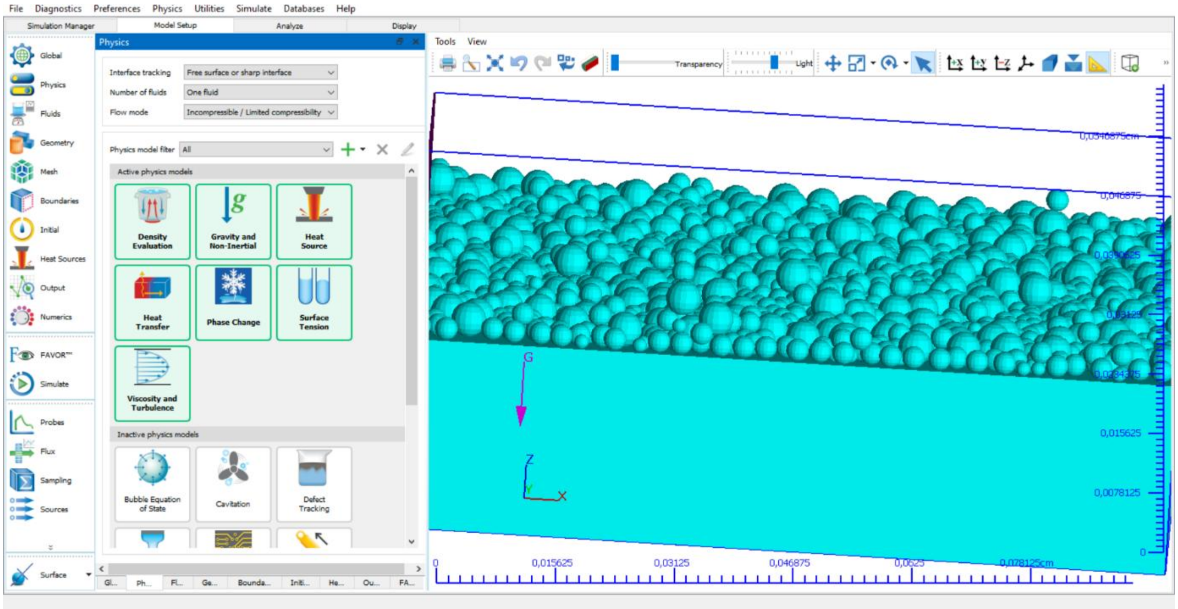
Interface tracking: Free surface or sharp interface
Number of fluids: One fluid
Flow mode: Incompressible / Limited compressibility
Physics model filter: All

Figure 17 Multiphysics model applied on powder bed created in flow 3D.

An important model we need to define is the heat source, which in our case is a laser. We've used a Gaussian distribution in the simulation, and the mesh size is critical for achieving reliable energy resolution. The cell size should be small enough to capture the steepest gradient region of the laser spot, and 2-3 cells should span the laser spot to accurately represent the intensity distribution.[98]

2.3 Part-scale simulation to study deformation using Abaqus

Software

For our FEM simulations, we used Abaqus, which is a comprehensive finite element analysis (FEM) software suite used for simulating a wide range of linear and nonlinear engineering problems. It supports various physics domains, including structural, thermal, electrical, acoustic, and fluid analyses. With a vast library of elements and material models, Abaqus can handle complex geometries and simulate the behaviour of materials like metals, polymers, composites, concrete, and soils. In nonlinear simulations, it automatically adjusts load increments and convergence criteria to ensure accurate and efficient solutions.

Using Abaqus, we have aimed to get accurate thermo-mechanical predictions on a simulated workpiece. We performed two types of simulations for heat transfer analysis and stress and displacement analysis to identify any possible residual stresses in the component as well as the temperature distribution of the moving heat source(laser)[99]

Part modelling

To replicate a real-life experiment, the L-PBF part we created a basic solid 3D deformable workpiece of 1mm x 1mm x 1mm, size, and a slightly larger substrate size of 5mm x 7mm. The material properties of SS316L were assigned to both the part and the substrate using sections, and most of the material properties were taken from literature [92], [97]. Key input parameters used were Temperature, conductivity, density, elasticity, expansion coefficients, latent heat plastic values, and specific heat. A detailed table is given in Appendix 1.B

Since the laser beam will create high energy density on the powder layer path, a fine, structured hex mesh has been used for the workpiece, with a slightly coarser mesh has been used for the substrate. A symmetric (fixed) boundary condition has been applied to the substrate for the structural simulation, while a thermal Dirichlet boundary condition has been applied to the heat transfer simulation. A master slave constraint between the workpiece and the substrate replicating an L-PBF simulation is used for both thermal and structural models. Fig 18 shows the stages of the part modelling mentioned so far.[99]

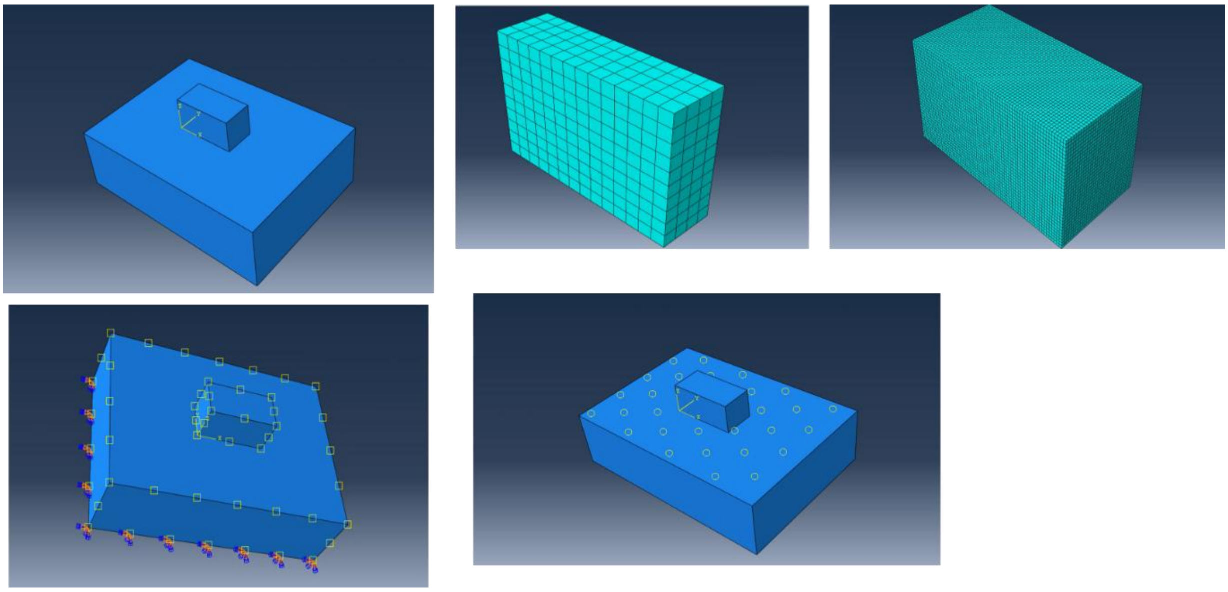

Figure 18 Abaqus simulation stages. Top left:- Assembly of substrate and workpiece after creating a part. Top right:- Coarse and fine meshes for substrate and workpiece, respectively. Bottom right:- Boundary conditions on substrate (structural model). Bottom right- Tie constraint between the bottom of the workpiece (slave) and top of the substrate (Master)

Heat source models

We have two types of heat source models in Abaqus (1) Concentrated heat source (CHS) or (2) Goldak's Double ellipsoid model. In our simulation, we decided to use CHS, which is the simplest, computationally fastest, and most straightforward model. In the CHS model, the distribution of the intensity of the heat flux is not defined in a fixed direction at a specific time. Instead, the laser spot is considered to be moving, with concentrated heat flux along a predefined path. This approach offers a simplified method for simulating a point energy source that follows a designed laser scanning trajectory. The moving heat source is assumed to follow a Gaussian distribution, forming the basis of widely used surface and volumetric heat source models. The equation governing the surface heat source model is defined as[100]:-

$$Q_s(x, y, t) = \alpha I_0 \exp\left(-2\,\frac{(x-x_c)^2+(y-y_c)^2}{r^2}\right) \tag{13}$$

Where Q_s= surface heat flux α= optical absorptivity, I_0= max beam intensity, x_c and y_c are the beam positions in x and y directions from its radius given by r. Max beam intensity I_0 is given by the equation.

$$I_0 = \frac{2P}{\pi r^2} \tag{14}$$

The volumetric heat source model is used to measure volumetric heat flux $Q_v$in a 3D space, and it is defined as [100]: -

$$Q_v(x,y,z,t) = \alpha\beta I_0 \exp\left[-2\frac{(x-x_c)^2+(y-y_c)^2}{r^2} - \beta(z_c - z)\right] \tag{15}$$

where β= coefficient of optical extinction centre (which means the area where laser is primarily absorbed) and z_c= beam centre along z direction. Fig 19 shows an illustrative diagram of the L-PBF process with a moving heat source [100], [101], [102]

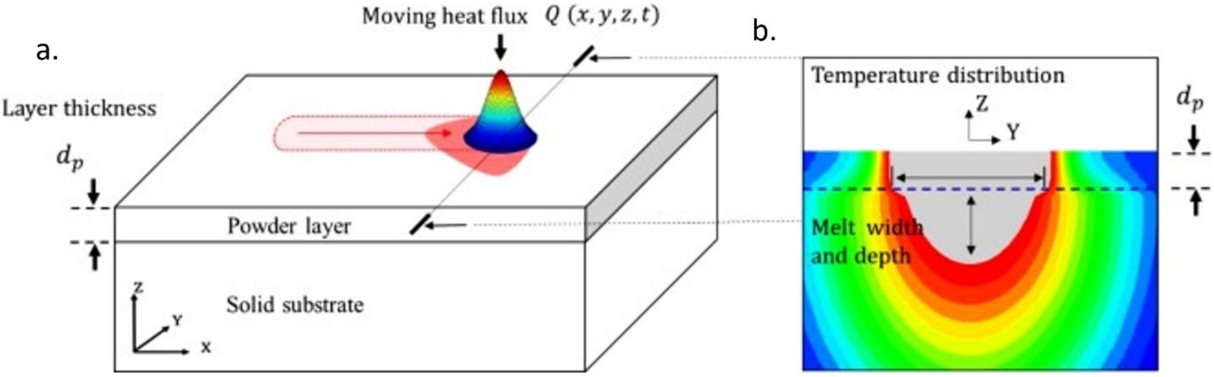

Figure 19 a. Schematic diagram of the melting process with a moving heat source. The intensity profile shows a Gaussian distribution .b. Cross Cross-section temperature profile of the melt pool generated [100]

Am Modeller plug-in

The Additive Manufacturing (AM) Modeler plug-in in Abaqus has features are specifically designed to model the L-PBF simulation process through its existing subroutine architecture and keyword interface. They are made accessible through table collections using reserved string identifiers beginning with "ABQ_AM".

To accurately capture the physical phenomena involved in AM, the AM Modeler provides two core simulation tools:

1. Progressive element activation for simulating the step-by-step deposition of material.
2. Moving heat fluxes for modelling the thermal effects of the electron beam during the process.

As illustrated in Fig 20a. The AM Modeler introduces three data types in the data setup section to manage the input data for L-PBF simulations:

1. Event Series:

   This defines both the spatial path and time-dependent behaviour of an event. It must include columns for time (t) and position (x, y, z), and may also include additional user-defined dependent variables. In our simulations, two separate event series files are used, i.e, Roller and Laser path:

   - The roller event series defines the motion of the powder recoater.

  - The Laser path event series defines the trajectory and heat input of the moving laser. This can either be user-defined or predefined. We used a G-code software replicator G to predefine our laser and roller path.

2. Parameter Table:
   This table is a predefined collection of parameters that is required to execute an event. For example, we can define the parameter moving heat source or material deposition using table collections later in the plugin.
3. **Property Table:**
   This is used to define material or process properties that may vary with temperature, field, and state-dependent variables. For instance, the absorption coefficient in the moving heat source model is defined through a property table.

Table Collections:

Table collections, as seen in Fig. 20.c can be used to define the parameters from the parameter table that will be used in the simulation. In our simulation, we define the material deposition table collections and select the roller so that the powder deposition process can be captured in the simulation. The moving heat source event series and the type of energy distribution(Goldak or Concentrated) can also be defined similarly. [103]

Furthermore, in the Model Setup and Simulation Setup section of the Am modeller, you can plot and view the event series on the workpiece and assign the material arrival from the roller event series, heating from the laser path event series and cooling if required.

G code

In L-PBF simulations using the Abaqus AM Modeler, G-code-like event series data is used to define the motion and characteristics of key process components such as the heat source or the powder recoater. Fig 20b. shows a typical line of event series data for our workpiece generated using Replicator G software, which slices STL files to generate G-code. It can be interpreted as follows: at 10 seconds into the simulation, the laser moves to the position (0.043 mm, 0.436 mm, 0.015 mm) in the X, Y, and Z directions, respectively, and applies a power of 150,000 W. For the recoater process, instead of power there's roller velocity.

Such data is typically fed into the simulation through an event series file that combines time-position information with process parameters like power or amplitude. Fig. 21shows an outline of the plotted event series on our workpiece for a single layer.[103]

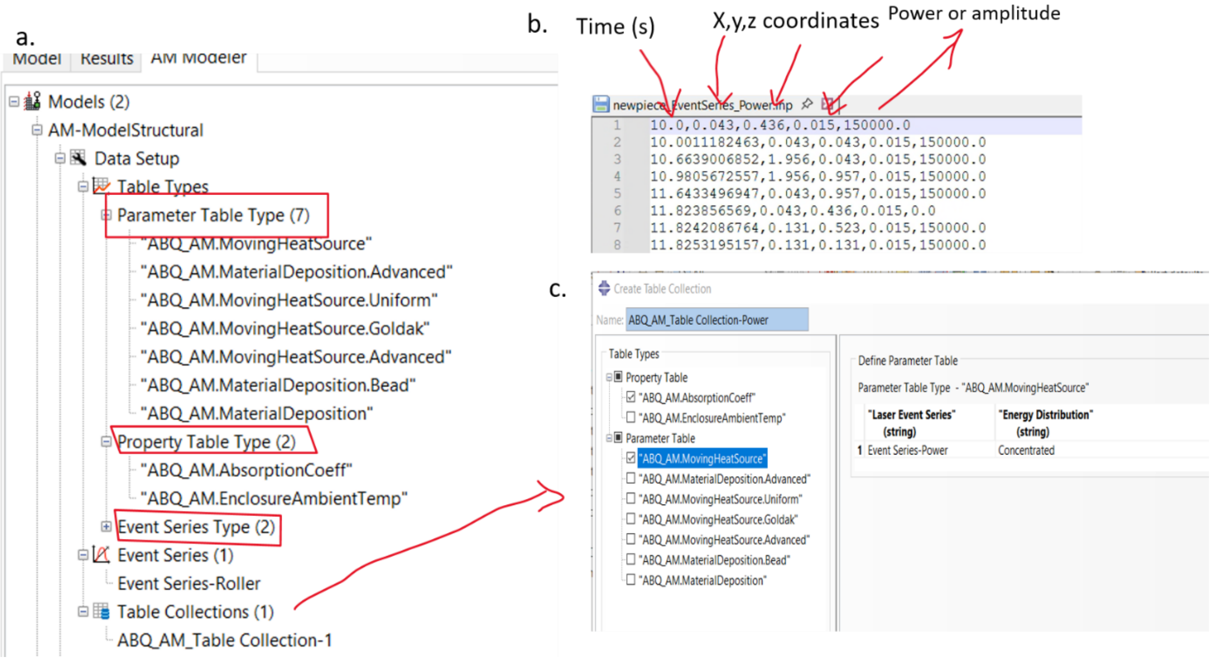

```
10.0,0.043,0.436,0.015,150000.0
10.0011182463,0.043,0.043,0.015,150000.0
10.6639006852,1.956,0.043,0.015,150000.0
10.9805672557,1.956,0.957,0.015,150000.0
11.6433496947,0.043,0.957,0.015,150000.0
11.823856569,0.043,0.436,0.015,0.0
11.8242086764,0.131,0.523,0.015,150000.0
11.8253195157,0.131,0.131,0.015,150000.0
```

Name: ABQ_AM_Table Collection-Power

☑ "ABQ_AM.AbsorptionCoeff"
☐ "ABQ_AM.EnclosureAmbientTemp"
☑ "ABQ_AM.MovingHeatSource"
☐ "ABQ_AM.MaterialDeposition.Advanced"
☐ "ABQ_AM.MovingHeatSource.Uniform"
☐ "ABQ_AM.MovingHeatSource.Goldak"
☐ "ABQ_AM.MovingHeatSource.Advanced"
☐ "ABQ_AM.MaterialDeposition.Bead"
☐ "ABQ_AM.MaterialDeposition"

Parameter Table Type - "ABQ_AM.MovingHeatSource"

	"Laser Event Series" (string)	"Energy Distribution" (string)
1	Event Series-Power	Concentrated

Figure 20 a:- AM modeller data types: Parameter table, property table, and Event series. b:- An illustration of how to interpret Event series c:- Table collection section where moving heat source can be defined along with the type of energy distribution desired.

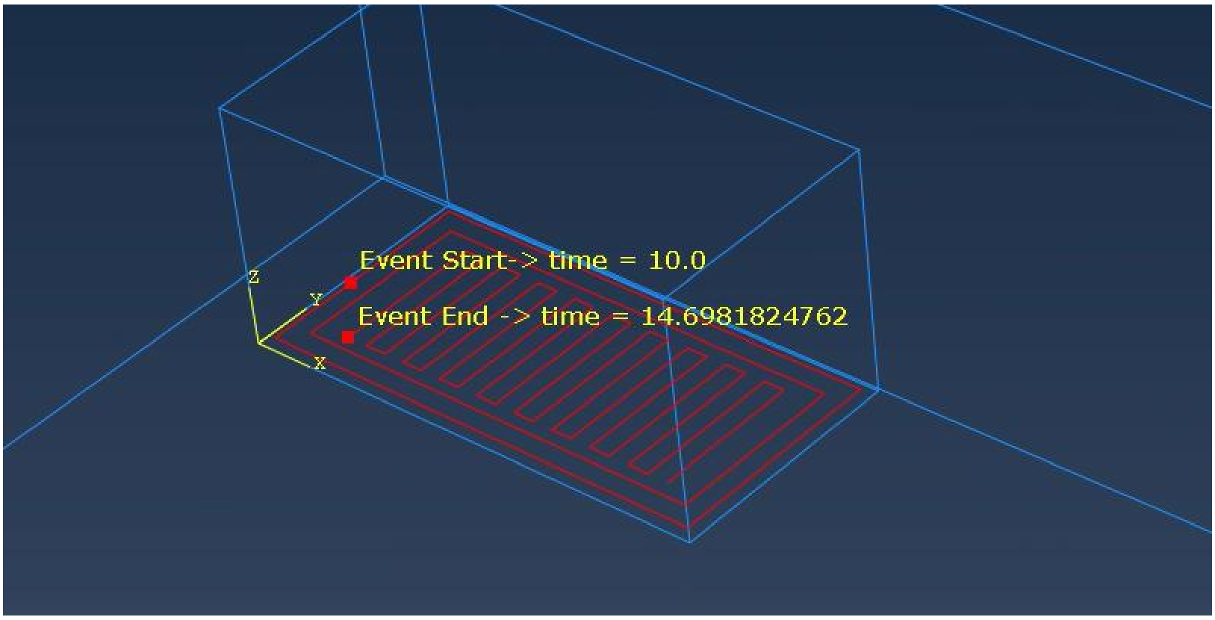

Figure 21 A single-layer Event series plot on work piece can be viewed through model setup section in AM modeller

2.4 Off policy Q learning

Imagine you walk every day to school during the monsoon and do not take an umbrella because you estimate your car ride to school is only 10 minutes away. On day 3 however, a manhole is opened in the middle of the road, causing floods, and the estimated time to reach school has increased, supposedly to 20 minutes. Your initial estimate of 10 minutes to reach school is now too optimistic. Will you wait to increase your estimate to 20 minutes or wait till you reach school to update your estimate to 20 minutes? Just like the human brain would learn the situation and change the estimate to 20 minutes, temporal difference prediction (TD) in Reinforcement learning also has the ability to learn immediately and converge to a new estimate faster than any other RL methods, such as Dynamic programming or Monte Carlo methods. [10]

The value of a state $V(S)$ for a policy π is initialised for $\forall s \in S^+$ arbitrarily, where $S \subseteq S^+$ denotes the set of all non-terminal states. The increment to $V(S')$ at the next time step is performed immediately depending on the reward R. The value of the current state is then updated using the TD update rule as [10]:

$$V(S) \leftarrow V(S) + \alpha[R + \gamma V(S') - V(S)] \tag{16}$$

where α is the learning rate, and γ is the discount factor that deems the importance of future rewards. The term inside the brackets is known as the TD error, representing the difference between the current estimate value and the sum of the reward and the discount value of the next state (which is the target value we aim to achieve).

TD prediction does not aim to improve the policy or take better actions, but rather to evaluate the given policy by learning more accurate estimates of state values through experience.

TD prediction updates the value of a state $V(S)$ based on the reward received and the estimation value for the next state S'. On the contrary, Q learning is an off-policy TD control algorithm that applies the TD control method by learning the value of taking a specific action a in a particular state S.

Q-learning focuses on the state-action pair $Q(S, a)$, and learns the optimal policy by estimating the cumulative discounted return for taking action a in a state S, regardless of whether the agent acts randomly or follows a greedy (best-action) policy during training. The algorithm updates its estimates using the Q-learning update rule [10]

$$Q(S, a) \leftarrow Q(S, a) + \alpha\left[R + \gamma \max_{a'} Q\,(S', a') - Q(S, a)\right] \tag{17}$$

where α is the learning rate, γ is the discount factor, R is the reward received after taking action a, and $\max_{a'} Q\ (S', a')$ is the maximum predicted future return from the next state S′. Over time, Q-learning converges to the optimal Q-values, allowing the agent to make optimal decisions even in probabilistic environments with delayed rewards. [10] .

Due to the benefits of off-policy flexibility, early convergence, and ease of implementation in Q-learning, we decided to use it in this study as a control system that learns to choose optimal P & V process parameters with minimized deformation, thereby maintaining the melt pool depth. Fig 22 represents the visualization of the Q learning method in our agent-environment interaction. In this setup, the laser acts as the agent, while the L-PBF process, simulated using finite element modelling (FEM), serves as the environment. The state S is defined by a discrete pair of (P, V) representing the laser power and scan speed. At every step, the agent chooses an action that alters this state by adjusting either or both parameters (e.g., increasing or decreasing power or speed). After each action, the agent receives a reward R or a penalty based on the resulting deformation. The optimal outcome in this process is to guide the agent toward state–action pairs that minimize deformation.

Through repeated interaction and learning, the agent updates its estimates of the Q-values, which represent the total expected reward for taking a specific action in a particular state. Over time, the agent learns a policy that favours actions leading to minimal deformation.[7]

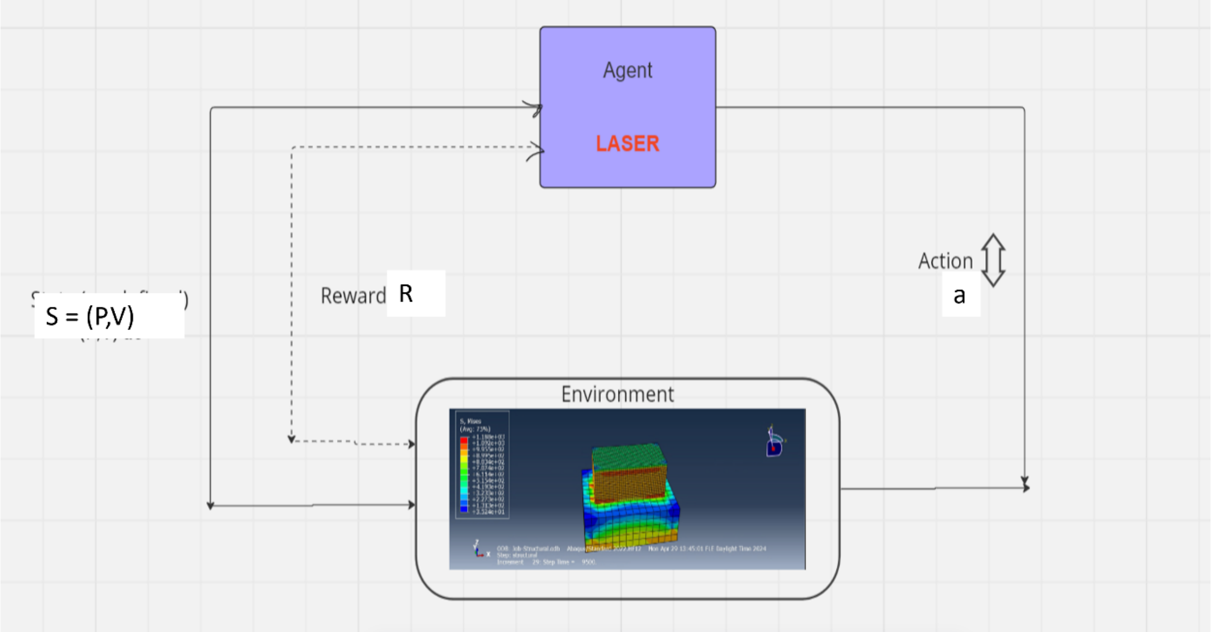

Figure 22 Visualization Q learning method in agent environment interaction. Laser acts as an agent and the L-PBF process that was simulated using FEM acts as the environment. State S is a discrete pair of (P,V) The action performed brings a change in (P,V) and is rewarded R or penalised based on the best state action pair with the lowest deformation (Fig adapted from Dharmadhikari et.al.[7].)

3 Results

This section shows the results of the methodology mentioned above. Section 3.1 included results of melt pool creation from Flow 3D, including predicted melt pool depth values using Response surface methodology. Section 3.2 shows simulation results generated from the Abaqus model, and their corresponding displacement values, which were then validated using RSM. Finally, a plot of rewards obtained per episode was extracted to study the Q learning behaviour.

3.1 Melt pool simulation Results

Using the parameters for particle interaction and DEM simulation setup mentioned in section 2.1 a powder bed was initially generated, followed by post-processing to simulate a melt pool for a single layer at a scanning speed of 700 mm/s and laser power of 150 W. The simulated melt pool was then validated against experimental results from the literature. The experimental melt pool had a width of 110 µm and a height of 100 µm, while the simulation results yielded a 20.91% deviation from the literature, with melt pool widths and heights of around 81 and 87 µm [92]. Fig 23a presents SEM images of the experimental sample (V = 700 mm/s, P = 150 W), and Fig 23b shows a comparison between the simulated and experimental results.

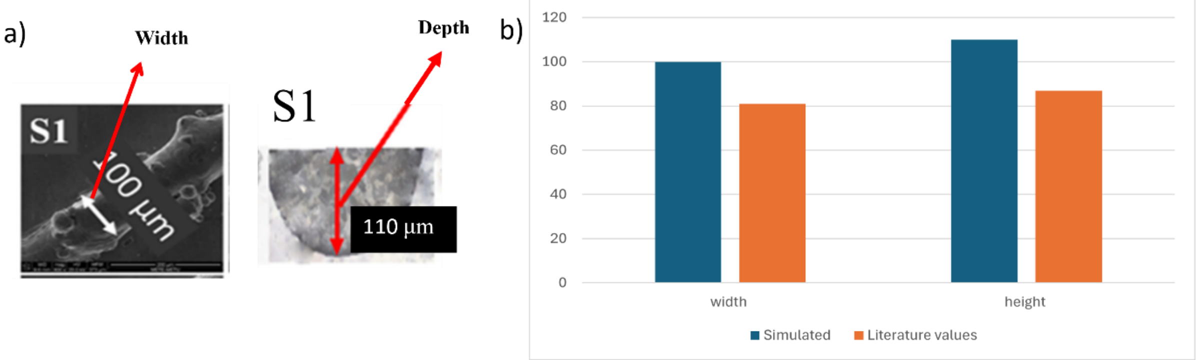

Figure 23 a.) SEM images of experimental sample from literature with V=700 mm/s and P=150 W b) Comparison of simulated and validated values, melt pool width and height

Based on this, additional simulation studies were conducted for 4 more combinations of scanning speeds and laser powers as outlined in Table 7.

Furthermore, Figs 24-28 present the post-processed melt pool images and the recorded melt pool depth values.

Simulation conditions	Laser Velocity V (mm/s)	Laser Power P (W)	Powder Layer thickness (µm)
Case 1	700	150	30
Case 2	400	75	30
Case 3	1000	75	30
Case 4	1000	300	30
Case 5	400	300	30

Table 7 Flow 3D Simulation setup conditions

Case 1

The post-processed images shown below are of the simulated melt pool (in red) with a scanning speed of 700 mm/s and laser power of 150 W, resulting in a depth of 87 µm. Figure 24a presents the cross-section in XZ direction, while Figure 24b displays the top view of the melt pool

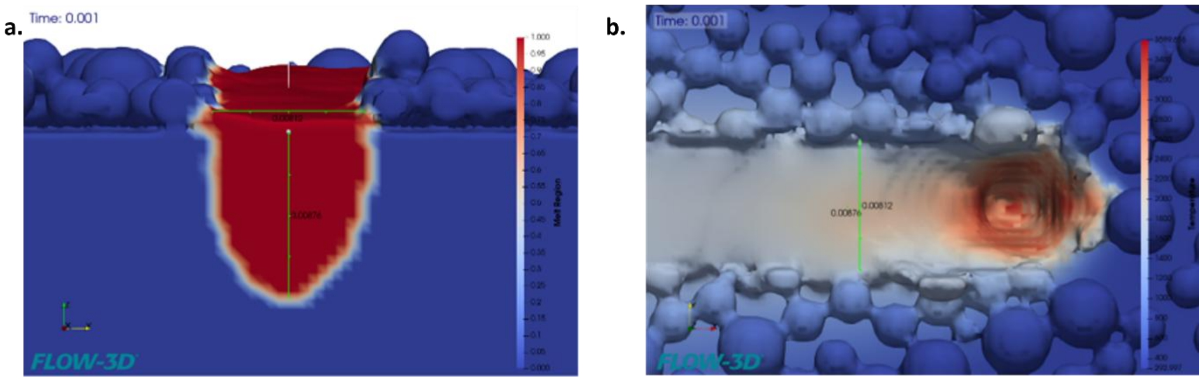

Figure 24 a. Cross section of Melt pool for Case 1 in XZ direction b. Top view of the melt pool

Case 2

Fig 25 are post-processed images of the melt pool generated with 400 mm/s scanning speed and 75 W laser power. The melt pool depth was recorded to be 49 µm.

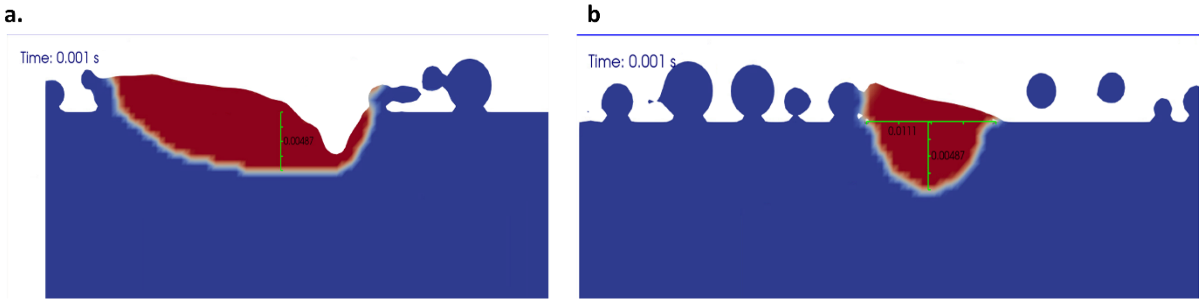

Figure 25 a. Cross section of melt pool in XZ direction for Case 2 b. Cross section of melt pool in YZ direction

Case 3

Fig 26 are post-processed images of the melt pool generated with 1000 mm/s scanning speed and 75 W laser power. The melt pool depth was recorded to be 24 µm.

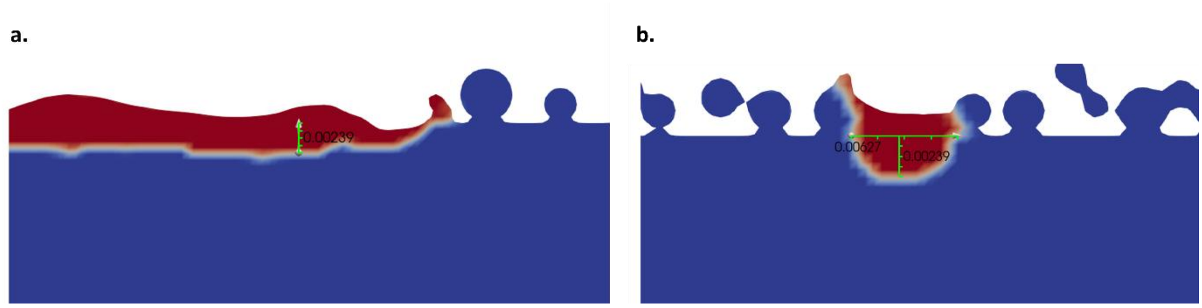

Figure 26 a. Cross section of melt pool in XZ direction for Case 3 b. Cross section of melt pool in YZ direction

Case 4

Fig 27 are post-processed images of the melt pool generated with 1000 mm/s scanning speed and 300W laser power. The melt pool depth was high and recorded to be 136 µm.

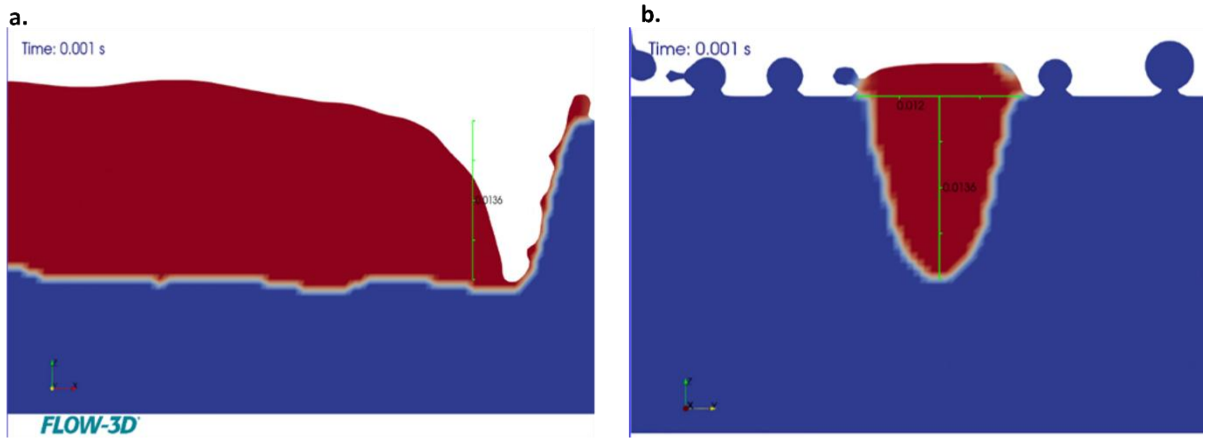

Figure 27 Cross section of melt pool in XZ direction for Case 4 b. Cross section of melt pool in YZ direction

Case 5

Fig 28 are post-processed images of the melt pool generated with a low scanning speed of 400 mm/s and the highest laser power of 300W. This case caused overpenetration because the melt pool went beyond the boundaries of the domain, which means the domain isn't enough to fully capture the physical phenomenon in the powder bed. The melt pool depth was approximately measured between 250- 270 µm

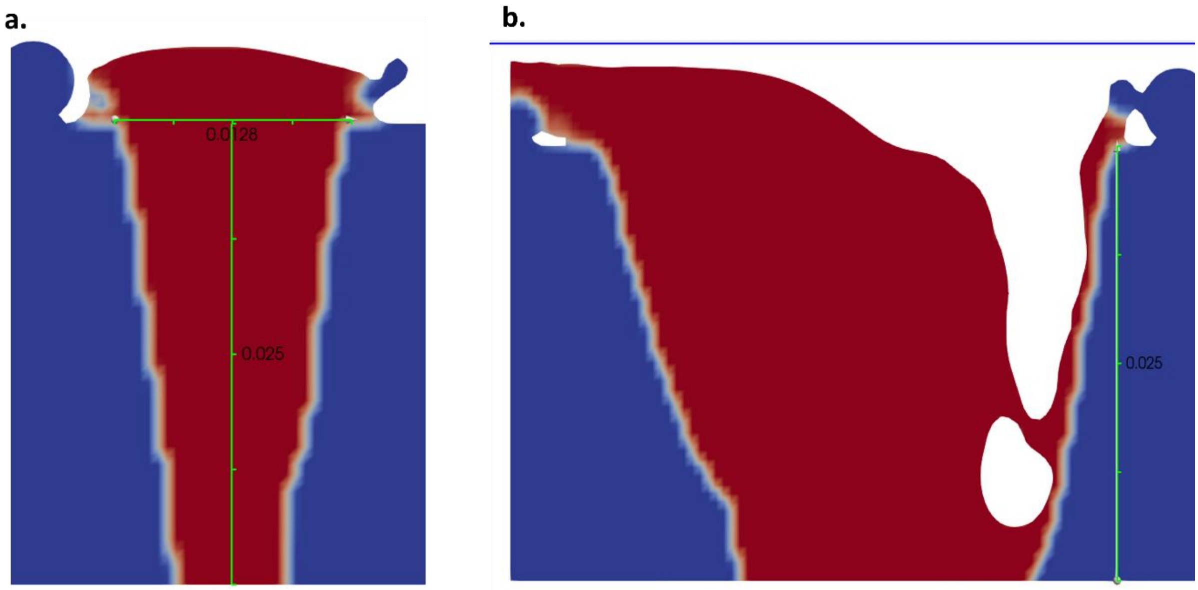

Figure 28 Cross section of the melt pool in XZ direction for Case 5 b. Cross-section of the melt pool in YZ direction

3.1.1 Melt pool depth prediction using response surface methodology

To have a larger data range for Laser power and scanning velocity, we decided to include more process parameter combinations with the simulation setup conditions mentioned in Table 8 below: -

Extended parameter conditions	Laser Velocity (mm/s)	Laser Power (W)	Powder Layer thickness (µm)
Case 6	1000	150	30
Case 7	400	150	30
Case 8	700	300	30
Case 9	70	75	30

Table 8 Additional Laser velocity and Laser power parameters

Due to time constraints, conducting Flow 3D simulation for all these parameter combinations would be impractical, therefore Response Surface methodology was employed to statistically predict the melt pool depths.

Response Surface Methodology (RSM) is a critical and reliable, analytical and quantitative s tool used for modelling and optimizing responses especially when several variables are involved. When the goal is to understand the relationship between input variables and to identify the conditions that yield an optimal outcome RSM is a valuable tool.

In several RSM problems the response function needs to be approximated using a low order polynomial in a specific sample region. When the response behaves linearly, a first-order model is approximated which can be denoted as[104]

$$y = \beta_0 + \beta_1 x_1 + \beta_2 x_2 + \varepsilon \tag{18}$$

where ε can be referred to as error function.

If curvature exists in the response surface a higher order polynomial is preferred, such as a second-order model with 2 variables which is denoted as[104]:

$$y = \beta_0 + \beta_1 x_1 + \beta_2 x_2 + \beta_{11} x_1^2 + \beta_{22} x_2^2 + \beta_{12} x_1 x_2 + \varepsilon \tag{19}$$

The main objectives of these models are to help approximate the true but unknown response function, allowing researchers to explore the topography of the response surface, such as local maxima, minima, and ridge lines, and efficiently determine the optimal max or min response. RSM relies on a well-planned experimental design and uses least squares estimation to fit the polynomial models. This approach is particularly useful in materials and manufacturing processes, where understanding how inputs affect output quality is critical for process optimization and control [104]. An example of RSM applications in manufacturing process is designing experiments to optimise surface quality of a machined part in a CNC operation by optimizing parameters such as cutting speed, feed rate, and depth of cut. Some approaches, such as factorial design of experiments, are used to define the upper and lower boundaries of each variable involved in the machining process. They are then employed to improve the optimization process using either first or second-order models[105].

To model the effect of laser scanning speed (v) and laser power (P) on the resultant melt pool depths **for** our remaining parameters, we approximated the relationship between the parameters using a second-order multiplicative polynomial function given as:

$$f(v,P) = (a_1 v^2 + b_1 v + c_1)(a_2 P^2 + b_2 P + c_2) \tag{20}$$

The fitted coefficients were determined using Excel's Solver tool, using the GRG Nonlinear solving method (due to the nonlinear nature of our model), which works by computing the gradient of the error and updating coefficients iteratively until an optimal solution is reached. The function was evaluated across the dataset, and Solver iteratively adjusted the six coefficients to minimize the sum of squared error between predicted and simulated melt pool depths. Once the coefficients were optimized, the fitted RSM model was applied to predict melt pool depth values for the extended parameter ranges. This approach allowed us to capture the nonlinear interaction between laser scanning speed and power with high accuracy, as validated with simulation data. The fitted coefficients calculated were: -

$$a1 = -6.7 \times 10^{-6} \quad b1 = -0.00097, c1 = 0.277832$$

$$a2 = 1.12 \times 10^{-5} \quad b2 = 0.000797 \quad c2 = -0.01976$$

Table 9 gives us the predicted melt pool depth function for Case 6-9 parameter conditions (refer to Table 8). The last column refers to the squared error between predicted and simulated melt pool depths

*$(a_1v^2 + b_1v + c_1) = e$ **$(a_2P^2 + b_2P + c_2) = f$

Scan Speed (v) [mm/s]	**Laser Power (P) [W]**	**Melt pool depth (from simulations)**	**e***	**f ***	**Melt pool function (mm²)**	**Melt pool predicted (×1000)**	**Squared error**
700	150	0.087	0.177051	0.351333	0.062204	62.204	0.00061484
1000	150	-	0.113664	0.351333	0.039934	39.934	7.70372E-34
400	150	-	0.228322	0.351333	0.080217	80.217	0
700	300	-	0.177051	1.225468	0.216971	216.971	0
1000	300	0.136	0.113664	1.225468	0.139291	139.291	1.08308E-05
400	300	0.27	0.228322	1.225468	0.279801	279.801	9.60554E-05
700	75	-	0.177051	0.102906	0.01822	18.22	0
1000	75	0.024	0.113664	0.102906	0.011697	11.697	0.000151372
400	75	0.049	0.228322	0.102906	0.023496	23.496	0.000650471
							Sum of square error= 0.001523569

Table 9 Effect of process Parameters on melt pool depth function.

3.2 Displacement analysis via FEM simulations

Table 10 presents both the simulated and predicted melt pool depth values for all combinations of laser power (P) and scanning velocity (V).

Using these values, nine part-scale L-PBF simulations were performed in Abaqus and their maximum and minimum displacement magnitudes were obtained. Figures 29-37 show the results of the simulations obtained and their effects on our workpiece and the substrate.

Total no of part scale simulation cases	Laser Velocity (mm/s)	Laser Power (W)	Melt pool depth (µm)
Sim Case 1	700	150	87
Sim Case 2	1000	150	39.934
Sim Case 3	400	150	80.2
Sim Case 4	700	300	216.971
Sim Case 5	1000	300	136
Sim Case 6	400	300	270
Sim Case 7	700	75	18.22
Sim Case 8	1000	75	24
Sim Case 9	400	75	49

Table 10 Laser velocity and Laser power values

Sim Case 1

Fig 29 illustrates the deformation results from Abaqus obtained for P= 150W and V= 700mm/s . The color contour represents the magnitude of displacement (UT, Magnitude), where red denotes the highest deformation and blue the lowest. The maximum deformation of approximately 3.76×10^{-2} mm occurs at the top surface of the workpiece, while the substrate remains largely undeformed. This simulation helps visualize stress accumulation and distortion due to thermal effects during fabrication.

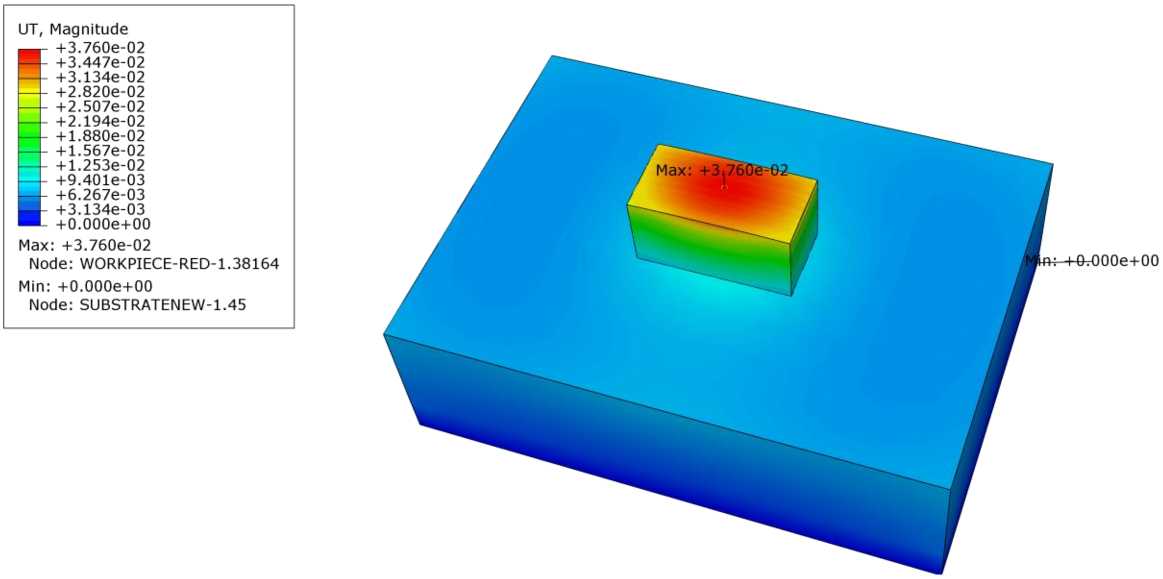

Figure 29 Structural simulation for Sim Case 1 for P= 150W and V= 700mm/s. Max deformation occurs at the top of the workpiece, while the substrate remains undeformed. Colour contours indicate the displacement gradient from 0 to 3.76×10^{-2} mm.

Sim Case 2

Figure 30 illustrates the deformation results obtained from Abaqus for P = 150 W and V = 1000 mm/s. The maximum deformation of approximately 3.93×10^{-2} mm occurs at the top surface of the workpiece, with a concentration at the center of the top layer. This simulation helps visualize stress accumulation and distortion due to thermal effects during fabrication.

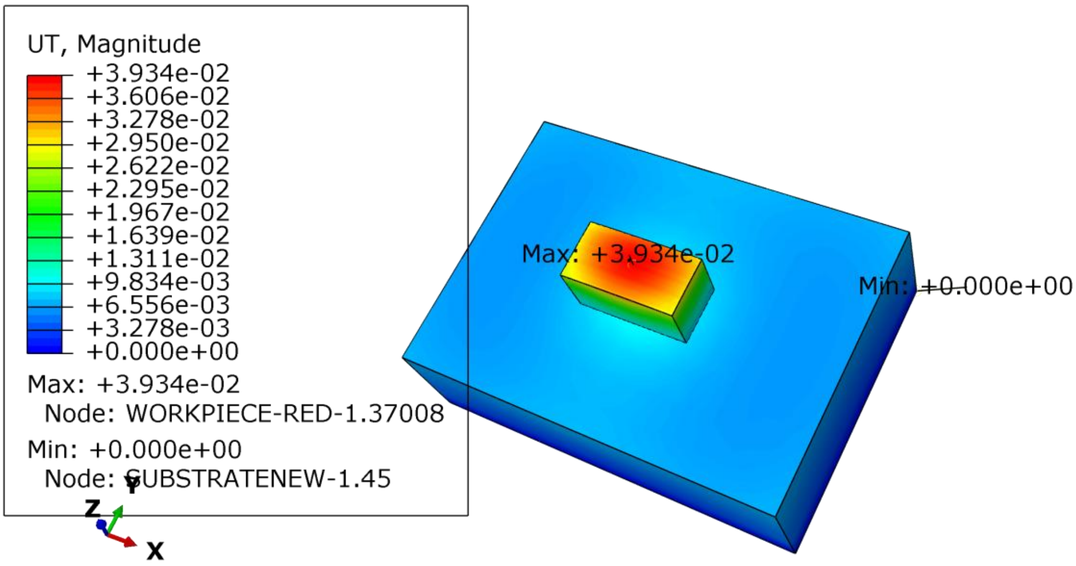

Figure 30 Structural simulation for Sim Case 2 for P= 150W and V= 1000mm/s. Max deformation occurs at the top of the workpiece, while the substrate remains undeformed. Colour contours indicate the displacement gradient from 0 to 3.93 × 10^{-2} mm.

Sim Case 3

Figure 31 illustrates the deformation results from Abaqus obtained P= 150W and V= 400mm/s. The maximum deformation of approximately 3.834 × 10^{-2} mm pretty similar to Sim 1 and Sim 2.

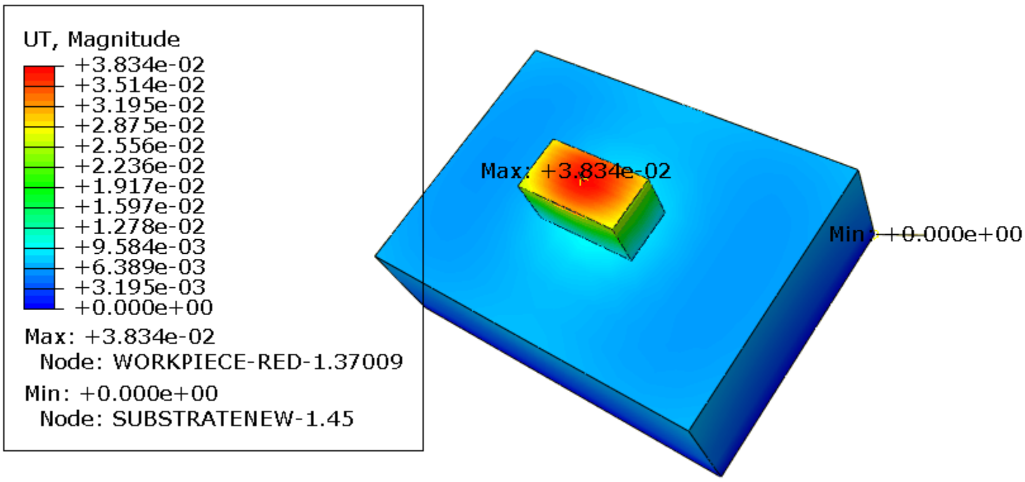

Figure 31 Structural simulation for Sim Case 3 for P= 150W and V= 400mm/s. Max deformation at 3.83 × 10^{-2} mm.

Sim Case 4

Figure 32 illustrates the deformation results from Abaqus for P= 300W and V= 700mm/s.

High displacement of 6.516×10^{-2} mm is concentrated at the centre of the top of the layer could be due to high laser power.

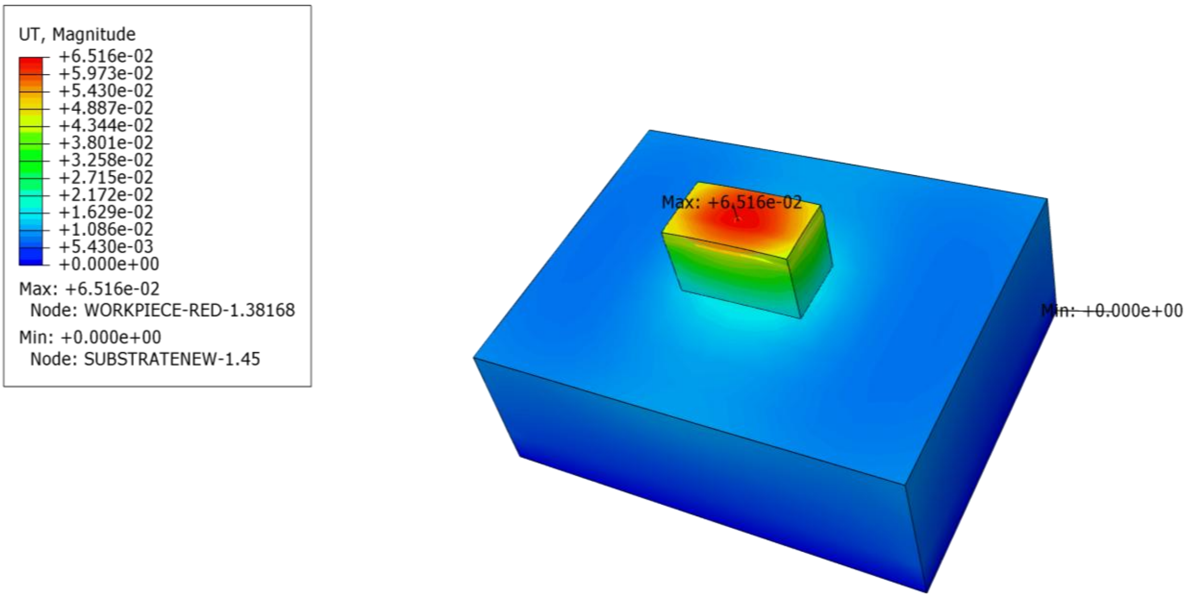

Figure 32 Structural simulation for Sim Case 4 for P= 300W and V= 700mm/s. High deformation of 6.516 × 10^{-2} mm occurs at the top of the workpiece.

Sim Case 5

Figure 33 illustrates the deformation results from Abaqus for P= 300W and V= 1000mm/s. High max deformation of 6.008×10^{-2} mm is concentrated at the centre of the top of the layer, similar to Sim case 4, albeit a little lesser due to the slight increase in scanning speed.

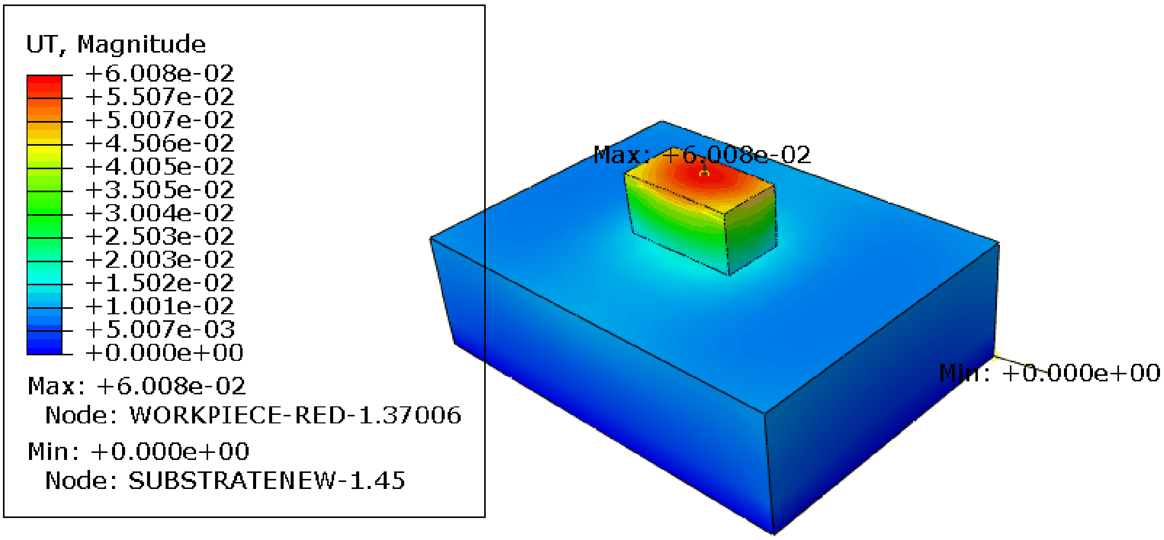

Figure 33 Structural simulation for Sim Case 5 for P= 300W and V= 1000mm/s. High max deformation occurs at the middle of the top layer of the workpiece

Sim Case 6

Figure 34 illustrates the deformation results from Abaqus for P= 300W and V= 400mm/s. The results are identical to Sim case 4 with a max deformation value of 6.515×10^{-2}mm.

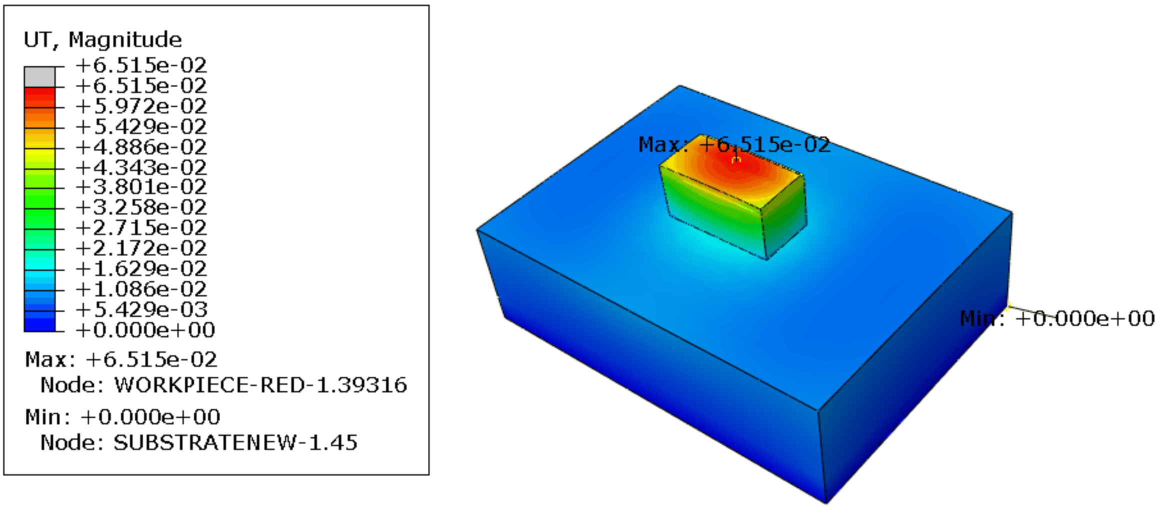

Figure 34 Structural simulation for Sim Case 6 for P= 300W and V= 400mm/s. High max deformation occurs in the middle region of the top layer of the workpiece

Sim Case 7

Figure 35 illustrates the deformation results from Abaqus for P= 75W and V= 700mm/s. A low maximum deformation value of approximately 1.923×10^{-2} mm can be seen at the top surface of the workpiece, and top layers of the substrate seem to show a small deformation value of 3.250×10^{-3}.

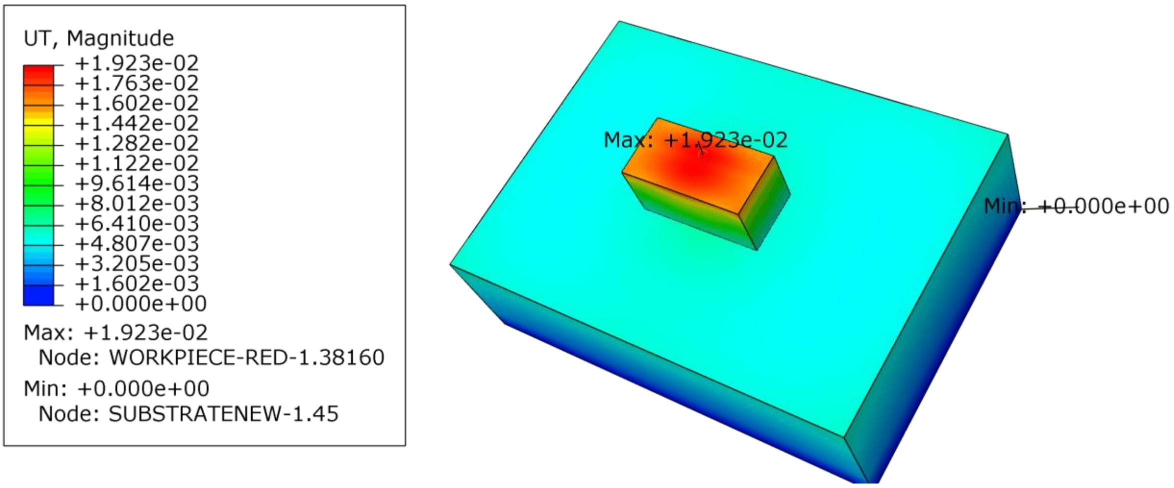

Figure 35 Structural simulation for Sim Case 7 for P= 75W and V= 700mm/s. Max deformation of 1.923×10^{-2} mm occurs at the middle area of the top layer of the workpiece. The substrate also shows slight deformation of 3.250×10^{-3}.

Sim Case 8

Figure 36 illustrates the deformation results from Abaqus for P= 75W and V= 1000mm/s .

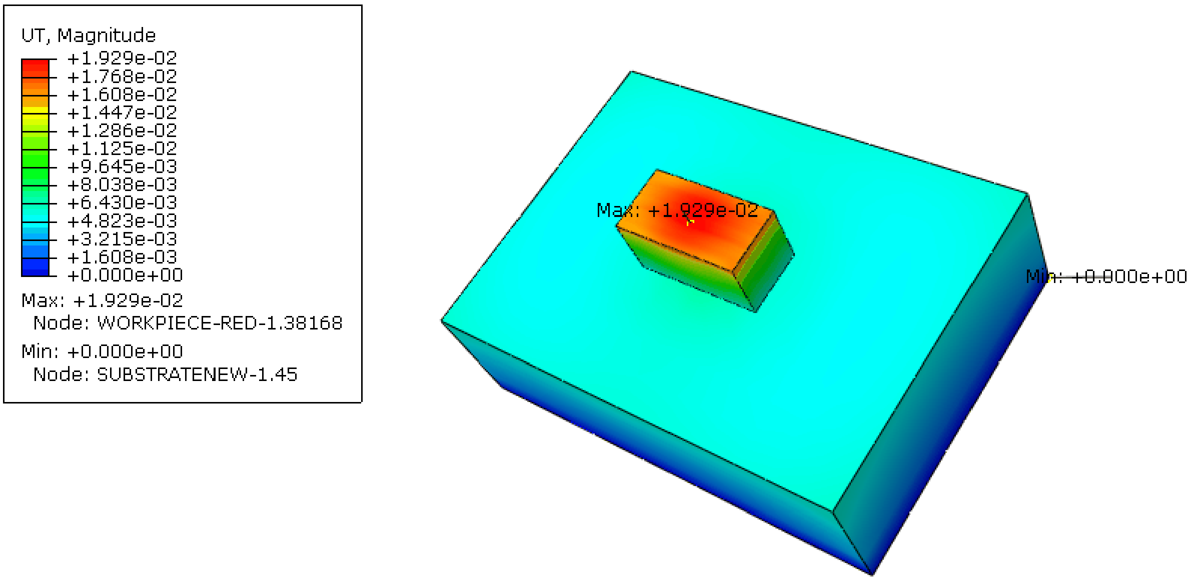

Figure 36 Structural simulation for Sim Case 8 for P= 75W and V= 1000mm/s. Max deformation of 1.923 $\times 10^{-2}$ *mm occurs at the top layer of the workpiece. The substrate also shows a slight deformation of 3.250* $\times 10^{-3}$.

Sim case 8 is identical to Sim case 7, with a low maximum deformation value of approximately 1.929 $\times 10^{-2}$ mm, and top layers of the substrate seem to show a small deformation value of 3.215 $\times 10^{-3}$

Sim Case 9

Figure 37 illustrates the deformation results from Abaqus for P= 75W and V= 400mm/s. The max deformation occurred is the lowest among all sim cases with a value of 1.897 $\times 10^{-2}$ mm is seen at the top surface of the workpiece, and top layers of the substrate seem to show a small deformation value of 3.16 $\times 10^{-3}$

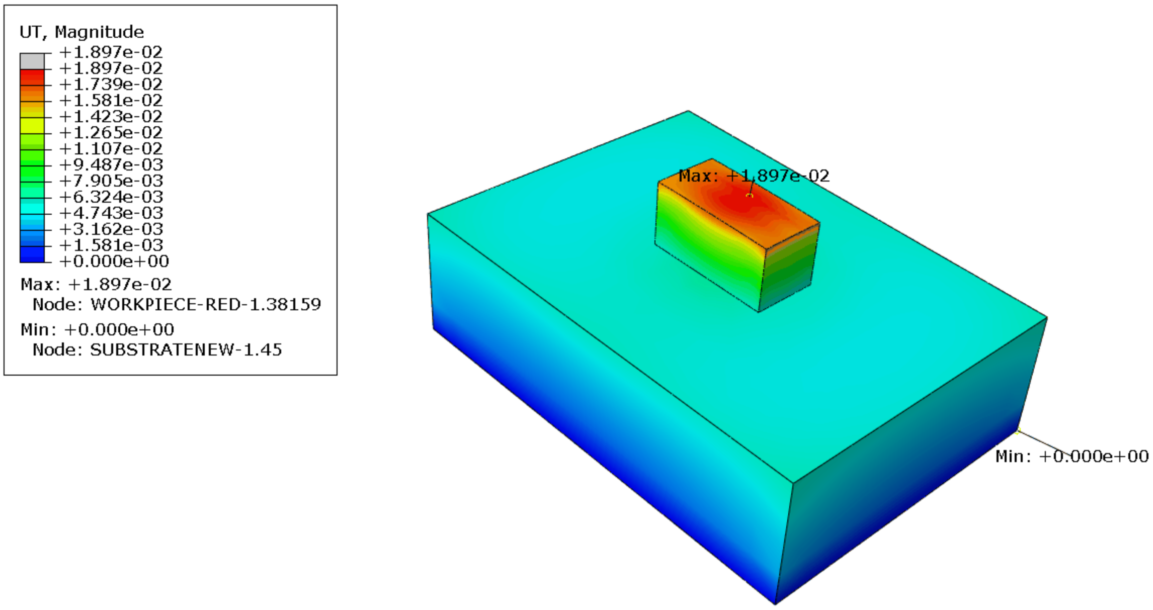

Figure 37 Structural simulation for Sim Case 8 for P= 75W and V=400 mm/s. Lowest deformation of 1.897 $\times 10^{-2}$ *mm occurs at the the top layer of the workpiece. The substrate also shows a slight deformation of 3.16* $\times 10^{-3}$*mm.*

3.2.1 Displacement response surface methodology

Similar to the melt pool depth prediction and analysis done in section 3.1.1 RSM was not only used to statistically analyse how laser power and scanning speed affected deformations, but also served to validate the displacement response obtained from simulations. The second-order multiplicative polynomial function to approximate the parameter relationship was of the same form as equation 20:

$$f(v,P) = (a_1 v^2 + b_1 v + c_1)(a_2 P^2 + b_2 P + c_2) \tag{21}$$

The fitted coefficients found using GRG nonlinear solving method are as follows

Where $a1 = -5.3 \times 10^{-5}$ $b1 = -0.005572, c1 = 2.321736$

$a2 = -0.0016$ $b2 = 0.143259$ $c2 = -1.90826$

Table 11 gives us the displacement function as well as the comparison of simulation-derived and model-predicted melt pool sizes. The components of the formula $(a_1 v^2 + b_1 v + c_1)$ and $(a_2 P^2 + b_2 P + c_2)$ breaks down how each parameter, P and V, was modelled using the function, resulting in the predicted displacement. The squared error between the simulated and predicted values are also listed to measure the model's overall accuracy.

v mm/s	**P (W)**	**Displacement simulation values**	**v*($a_1v^2 + b_1v + c_1$)**	**p* ($a_1v^2 + b_1v + c_1$)**	**Displacement Predicted**	**Squared error**
700	150	3.76E-02	2.450429	15.8759	38.9029	1.70E+00
1000	150	3.93E-02	2.345583	15.8759	37.2383	4.42E+00
400	150	3.93E-02	2.459275	15.8759	39.0433	0.4946
700	300	6.52E-02	2.450429	26.2507	64.3256	0.6962
1000	300	6.01E-02	2.345583	26.2507	61.5733	2.2299
400	300	6.52E-02	2.459275	26.2507	64.5578	0.3510
700	75	1.92E-02	2.450429	7.9100	19.3829	0.0234
1000	75	1.93E-02	2.345583	7.9100	18.5536	0.5423
400	75	1.89E-02	2.459275	7.9100	19.4529	0.3057
					Sum of Squared error	1.08E+01

Table 11 Effect of process Parameters on Deformation function

3.3 Q learning Results

Based on the visualization done in section 2.3, it has been established that our agent is the laser and our domain is the L-PBF environment, governed by a reward function. The agent can operate in the state space (P, V) and is discretized as follows:

- Scan speed v∈ [40, 100] mm/s with an interval of 0.1 in between
- Laser power P∈ [75,300] W with an interval of 0.1 W

To move to the next state S' The agent could perform one of nine discrete actions at each step, defined as combinations of incremental increases, decreases, or no changes in v and P (which can be considered a null action), as shown in Figure 38. Each action tells the agent how to modify (P, V)

P ↑	P ↓	P ↑	P ↑	P ↓	P	P	P ↓	P
V ↑	V ↑	V ↓	V	V ↓	V ↑	V ↓	V	V

Figure 38 Nine discrete actions in action space A. Increase is denoted by upward arrow and decrease is denoted by downward arrow

From the L-PBF process perspective, repeating the same (P, V) values neither explores alternative process conditions nor contributes to deformation reduction, offering no benefit. Therefore, actions that leave both parameters unchanged are excluded to avoid inefficient learning or poor results.

The updated (P, V) is then passed to the reward function (v, P), which is our displacement from equation (21)

$$f(v, P) = (a_1 v^2 + b_1 v + c_1)(a_2 P^2 + b_2 P + c_2)$$

Then we introduce the conditionality that: -

if f > 0:

return $\frac{1}{f}$

As $\frac{1}{f}$ value increases, the f value decreases, lower the displacement f, the higher the reward received.

Similarly, if f ≤ 0, then the state is being penalized by -1

This reward is then used to guide future action selection via exploration or exploitation, and update the Q table using equation 17.[10]

$$Q'(S, a) \leftarrow Q(S, a) + \alpha \left[R + \gamma \max_{a'} Q\,(S', a') - Q(S, a)\right]$$

Where:

Q'= updated Q values

S: Current state defined by (v, P)

a: Action taken in state S.

R $= R(S, a)$: Immediate reward after taking action a in state S

$R(S, a) \ = \ reward\ fucntion \ \ = f(v, P)$

S': Next state after action

$\gamma \ \max_{a'} Q\,(S', a')$=maximum expected reward for all future actions a' from state S'

α = Learning rate

γ =Discount factor

Role of Hyperparameters

Hyperparameters are chosen before training to guide the agent's learning behaviour to minimize deformation. In our study, we used five hyperparameters[7] : -

1. **Learning rate (α)**- Takes values between 0 to 1 and determines how quickly the Q value is updated in response to new information. A small value, such as $\alpha = 0.01$, encourages gradual learning, while a larger value encourages quicker learning; however, these values can be unstable or noisy. In our study, the learning rate is set at $\alpha = 0.01$ to encourage gradual learning.
2. **Discount factor (γ)**:- It controls the balance between future and immediate rewards. A higher discount rate focuses on long-term rewards. A mid-range discount factor, such as $\gamma = 0.5$, strikes a balance between short-term and long-term rewards. Hence, we have used both long-term discount factor $\gamma = 0.7$ and the mid-range $\gamma = 0.5$ in our algorithm.
3. **Exploration rate (ε)**:- Often called the exploration-exploitation trade-off parameter, as it governs the trade-off between the agent exploring new actions and exploiting the best action learned so far[7], [10]. In our study, the exploration rate has been varied to examine its impact on convergence behaviour and its effects on reward progression. Over time, ϵ was decayed multiplicatively by a factor of 0.9995. The decay rate reduces exploration over time, allowing the agent to explore less randomly and exploit the learned Q values for more stable rewards.
4. **Number of Episodes**: - It’s the full learning cycle an agent experiences. More episodes provide more convergence but raise the computation time. In our study we have gradually increased the episodes from 50,000, 200000 and 1000000 episodes to study the convergence behaviour and computation time.
5. **Max Steps**: - Refers to the number of actions the agent can take in an episode. Although there are nine defined actions in the action space, the action that does not change v and P is not considered meaningful since repeating (P, V) doesn’t generate new deformation outcomes. Therefore, only 8 steps are considered in each episode.

3.3.1 Learning Curve Analysis

For our algorithm, the Q-table was initialized with all values set to 10.0 to encourage early exploration. At each step, the agent selected an action using an epsilon-greedy policy to evaluate the learning behaviour of the Q learning agent. A plot of rewards obtained per episode was generated for hyperparameters. Learning rate (α), Discount factor (γ), Exploration rate (ε), Number of Episodes, Max steps per episode.

The hyperparameters were tweaked for different configurations as shown in Table 15: -

Configurations	Learning rate (α)	Discount factor (γ)	Exploration rate (ε)	Episodes	Max steps/episode	Epsilon decay
Config A	0.01	0.5	0.2 (decayed over time)	50000	8	0.9995
Config B	0.01	0.5	0.4	200000	8	0.9995
Config C	0.01	0.7	0.7	1000000	8	0.9995

Table 12 Q learning Hyperparameters for three different configurations

Config A rewards vs episodes

Fig 39 shows the graph of the number of training episodes vs reward obtained by the agent in each episode for Config A. The reward was smoothed using a moving average to reduce noise and data fluctuations.

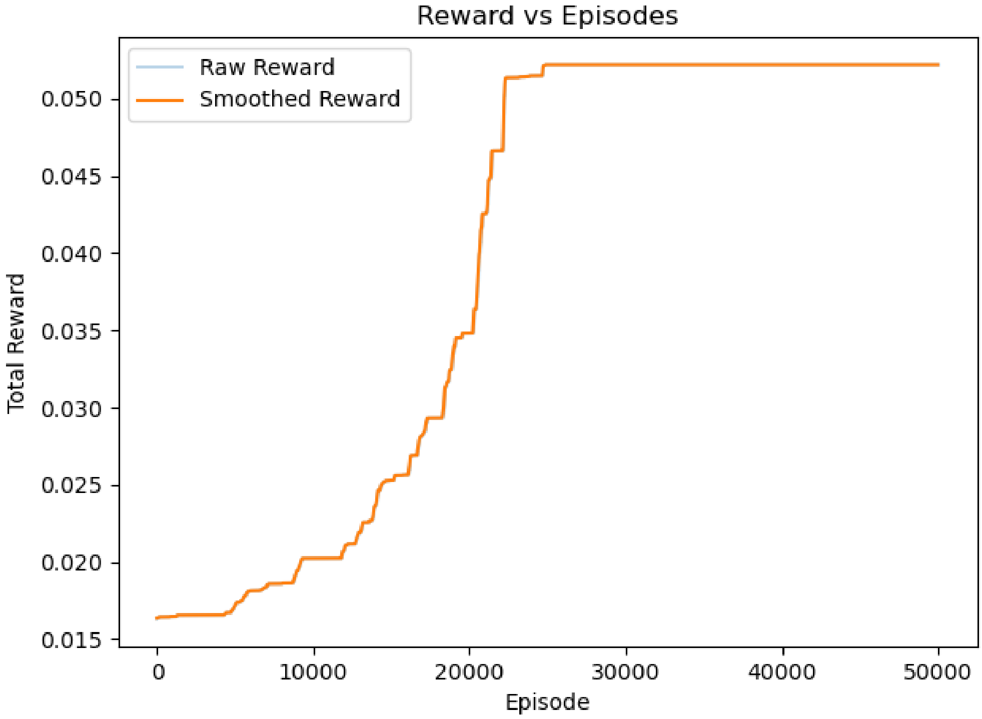

Figure 39 Rewards vs episodes graph for Configuration A

Epsilon (ε) is 0.2 over 50,000 episodes, with 8 steps per episode, incorporating ε-greedy exploration with a 20% chance of random action selection.
The discount rate (γ) is set to the mid-range to ensure a balance between rewards. As shown in the graph, the rewards show and steady increase, eventually stabilising with an increase in episodes.

Config B rewards vs episodes

Fig 40 shows the graph of number of training episodes vs reward obtained by agent in each episode for Config B. Here all hyperparameters such α, γ, and max steps was kept unchanged from the previous Config A, except for the number of episodes and ε, which was increased to 0.4. They were increased from 50,000 episodes to 200000 to check the convergence behaviour. As shown in the graph, the rewards show moderately convergent behaviour.

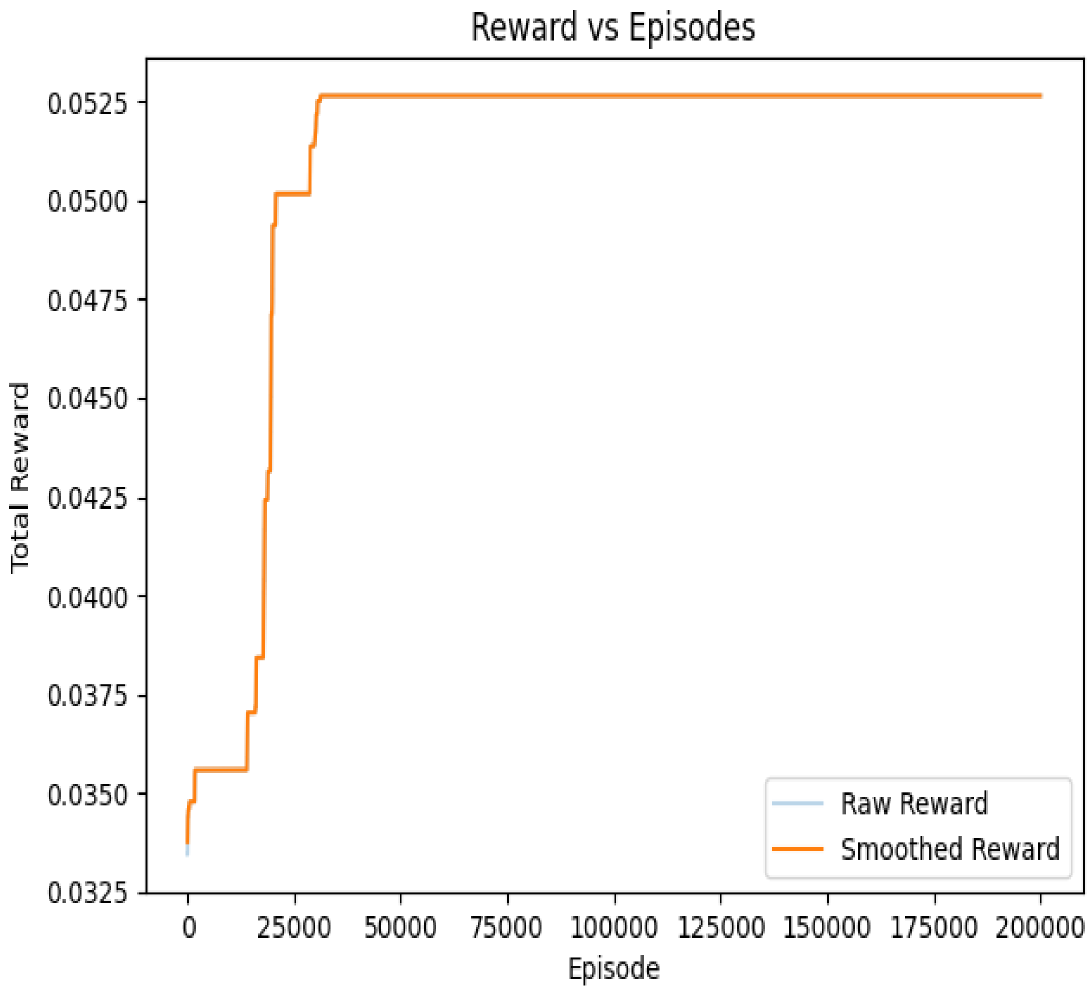

Figure 40 Rewards vs Episode graph for config B

Config C rewards vs episodes

Fig 41 shows the graph of the number of training episodes vs reward obtained by agent in each episode for Config C. Here, hyperparameters ε, γ, and number of episodes were all increased to 0.7, 0.7 and 1000000. Similar to Config B, the rewards in Config C also showed rapid convergence, almost around the same episode, however, it took a longer computation time.

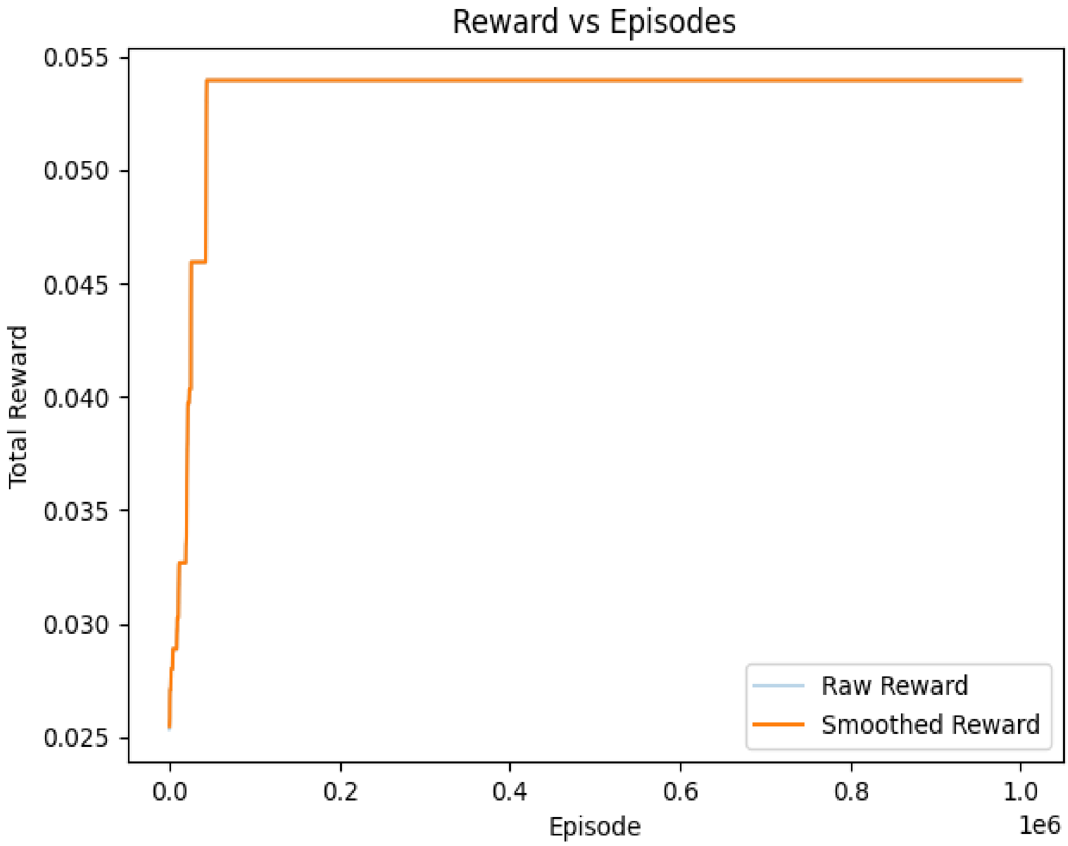

Figure 41 Rewards vs episodes for Config C

4 Analysis and Discussion

This section presents a detailed analysis of the Q-learning agent's performance in optimizing laser power (P) and scan speed (V) parameters for the L-PBF process. The results from the melt pool depth prediction and displacement simulations are interpreted alongside the agent's reward evolution, policy behavior, and Q-value distributions. Key patterns in learning dynamics and their implications for parameter optimization in additive manufacturing are discussed, supported by reward trends and Q-value heatmaps.

4.1 Simulated and predicted melt pool depths

In section 3.1, the flow 3D melt pool simulations for Case 2 and Case 3 show narrow penetration and a shallow melt pool. This could occur because there is not enough energy input due to the scanning speed and laser power being too low. It could cause a plethora of defects, such as lack of fusion, weak mechanical properties and so on.

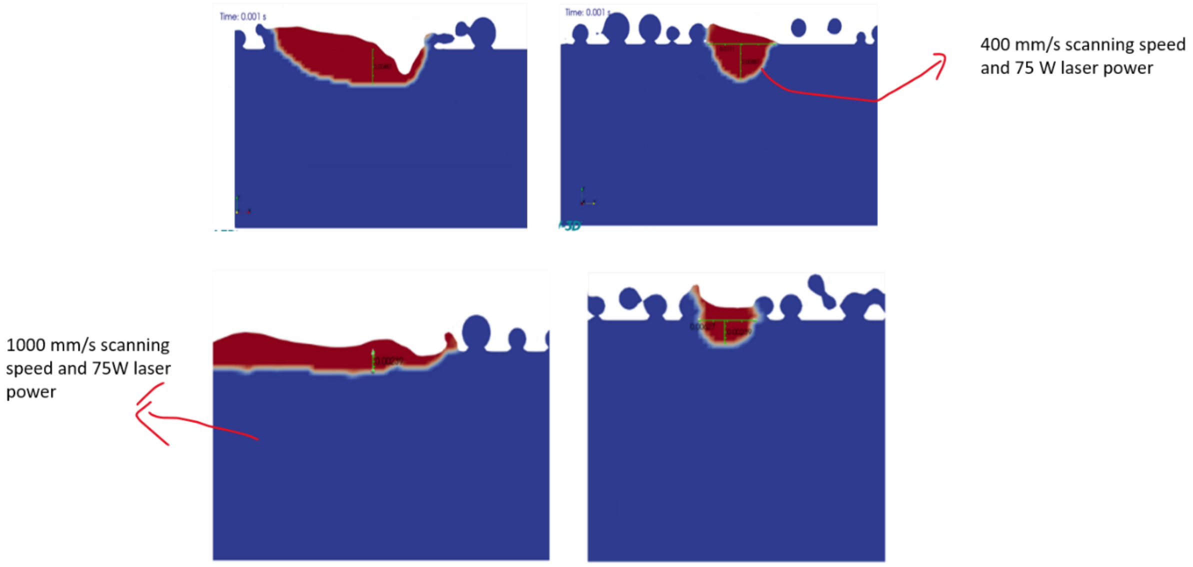

400 mm/s scanning speed and 75 W laser power

1000 mm/s scanning speed and 75W laser power

Figure 42 Melt pool simulation case 2 at V= 400 mm/s and P= 75W and case 3 at V= 1000 mm/s and P= 75W show narrow penetration and shallow melt pool depth.

For **Case 5** with a low scanning value and too high laser power, overpenetration might be due to excessive input energy, causing a keyholing-type defect. The melt pool observed in this case is roughly between 270 to 300 µm. For simplicity purposes, we decide to approximate it to 270 µm. The simulation was accurate in measuring high displacement for this case and it was validated by the statistical model as well.

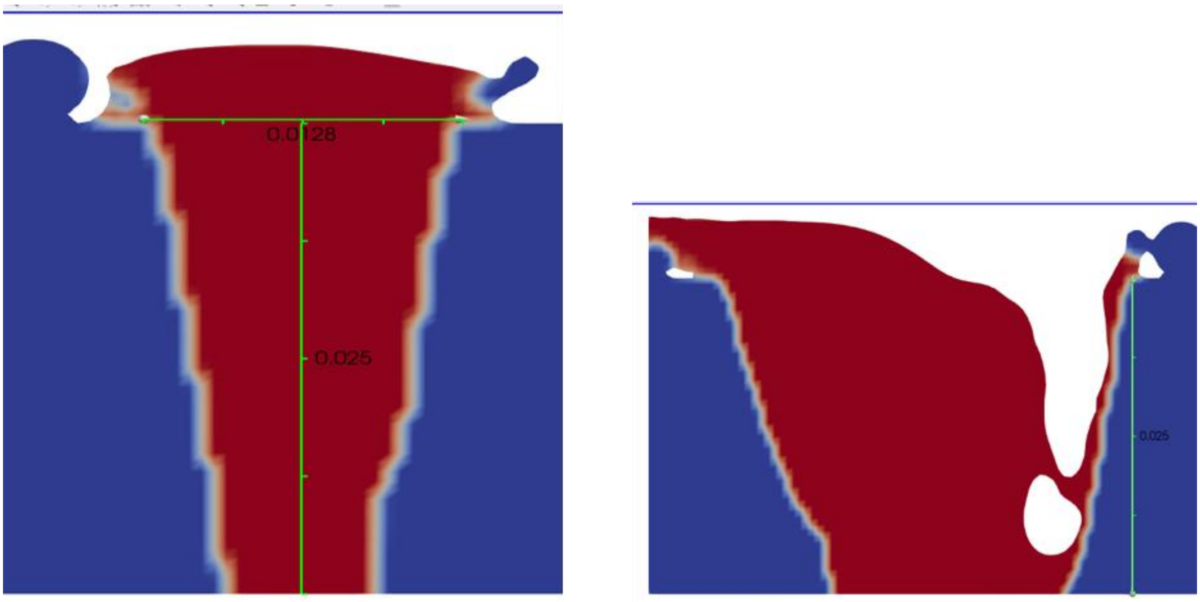

Figure 43 Case 5 with too high laser power leading to overpenetration

In section 3.2.1, Table 10. we predicted melt pool depth values for some combinations of laser power and scanning speed using response surface methodology. From Fig 44 we can see the effects of scanning speed on the predicted melt pool depth values. The trend exhibited a nonlinear behaviour, where melt pool depth initially increased and reached a peak, and then decreased with increasing scanning speed. This relationship was modelled by fitting a second-order polynomial curve. This suggests that high scan speeds lead to a shallow melt pool depth due to reduced laser material interaction time and decreased input energy where as low scan speeds can cause overheating or an unstable melt pool.

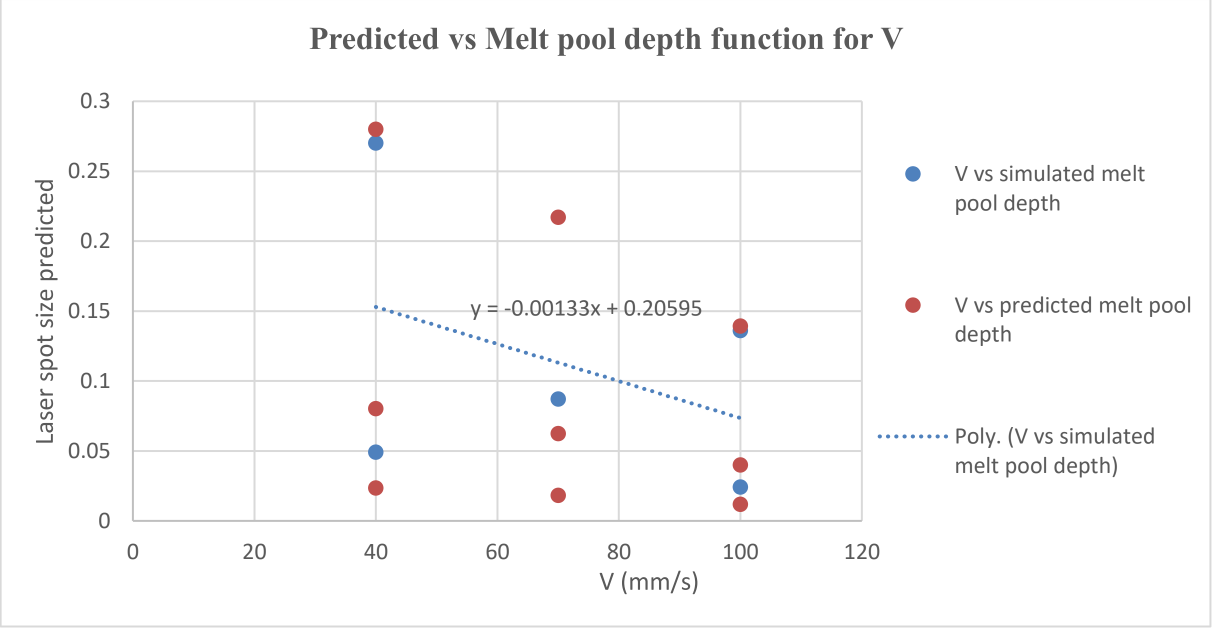

Figure 44 Graph showing relationship between Velocity (mm/s)v and melt pool depth function.

Similarly, from Fig. 45 we can see the effects of laser power on the predicted melt pool depths. The response surface revealed a convex relationship, where the melt pool increased nonlinearly with increasing laser power. The curvature suggests that higher laser powers lead to a disproportionately larger melt pool depth, which can cause overpenetration and an unstable melt pool, as high laser power suggests higher energy density of the system. On the other hand, lower laser power gives a shallow melt pool depth. Both of these conditions could lead to defects.

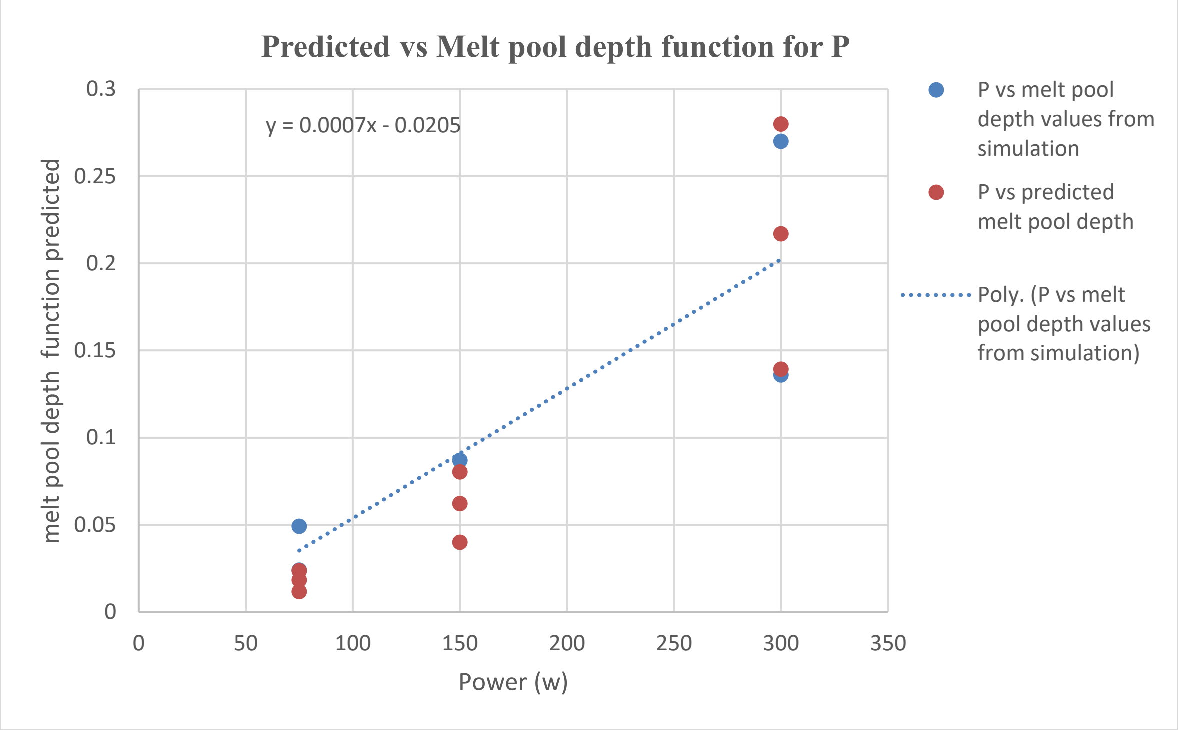

Figure 45 Graphical representation of laser power (W) vs melt pool depth values, where blue dots indicate Power vs simulated depth values and orange dots indicate Power vs predicted values.

Discussions

Both Flow 3D and Response Surface Methodology are effectively capturing the complex relationship between the input parameters and melt pool depth.

- From the simulated results, Case 3 with the melt pool depth of 49 μm is the smallest melt pool depth at V = 100 mm/s and lowest power P = 75 W.
- Predicted melt pool depths using RSM also resulted in a minimum melt pool depth was observed at highest scanning speed v = 100 mm/s and lowest power P = 75 W, while a maximum occurred at v = 100 mm/s and P = 150 W, consistent with the simulation trends.

- Hence, both predicted and simulated values suggest moderate scan speed combined with moderately high power is optimal for a desirable melt pool depth.

4.2 Predicted and simulated deformation values

In section 3.2, the deformation results for the nine part-scale L-PBF simulations performed in Abaqus were shown. Fig 46 shows the largest and smallest displacement observed out of all the simulations conducted. The smallest displacement of 1.89×10^{-2}mm was found at V= 400 mm/s P= 75W; however largest displacement of 6.516×10^{-2} mm was recorded to be identical for two sets of (P, V) combinations: (1) V= 400 mm/s P= 300W, (2) V= 700 mm/s P= 300W

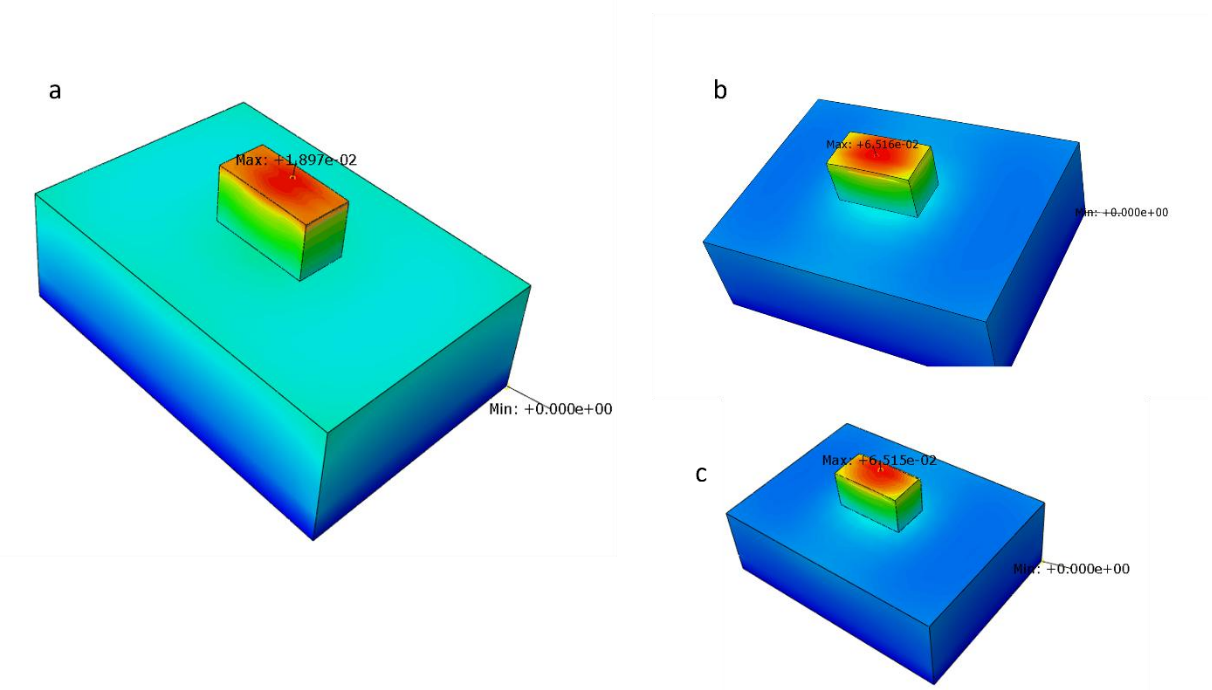

Figure 46 a. Smallest recorded displacement at 400 mm/s and 75 W. Maximum displacement reaches approximately 1.89 $\times 10^{-2}$ *mm, concentrated near the on top layer of workpiece. Figures 43 b and 43 c share the largest displacement results at V= 400 mm/s P= 300W and V= 700 mm/s P= 300W. Maximum displacement reaches approximately* 6.52×10^{-2} *mm, concentrated near the on top layer of the workpiece c. largest displacement observed from simulation at V= 400 mm/s P= 300W W. Maximum deformation for both reaches approximately* 6.52×10^{-2} *mm*

The predicted displacement values derived using the Response Surface Methodology (RSM) show strong alignment with the Abaqus simulation results across all simulated cases, as illustrated in Fig 47. the bar chart compares the predicted and simulated deformations, showing only minor deviations while overall consistency remains good. Moreover, as shown in Table 11 (Section 3.2.1), RSM successfully differentiates between cases where the highest simulated deformation values were similar, depicting the model's sensitivity to nuanced trends. The highest predicted displacement value lies at 6.45×10⁻² mm at V= 400 mm/s P= 300W.

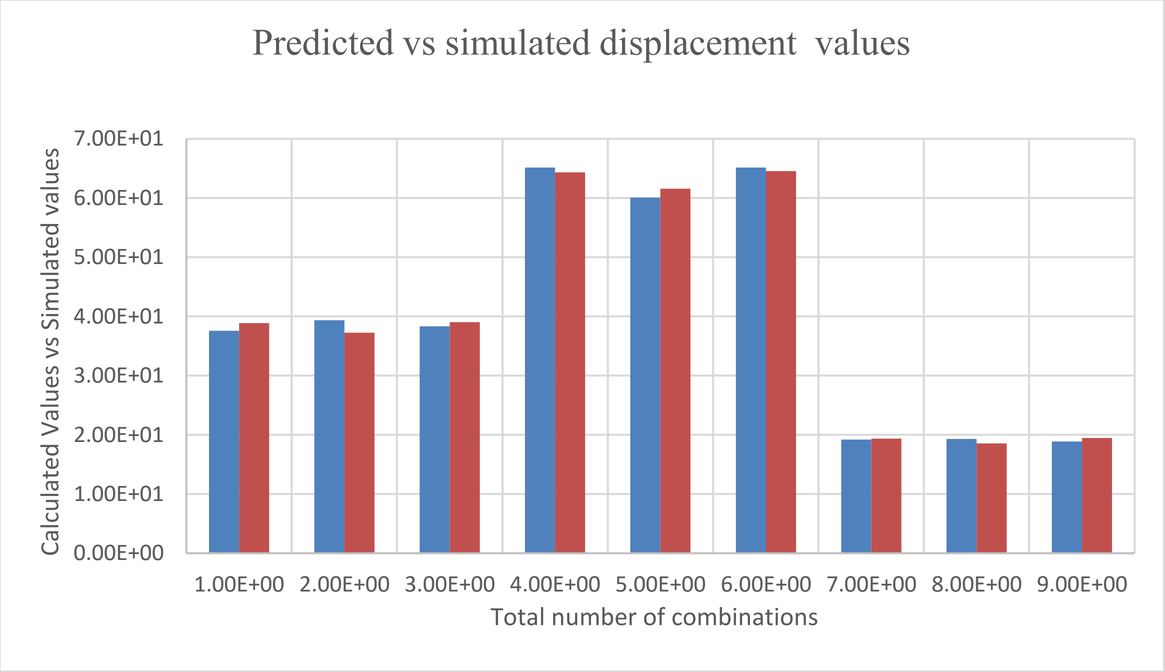

Figure 47 Comparison of simulated and predicted deformation values for nine input parameter sets (scan speed and laser power)

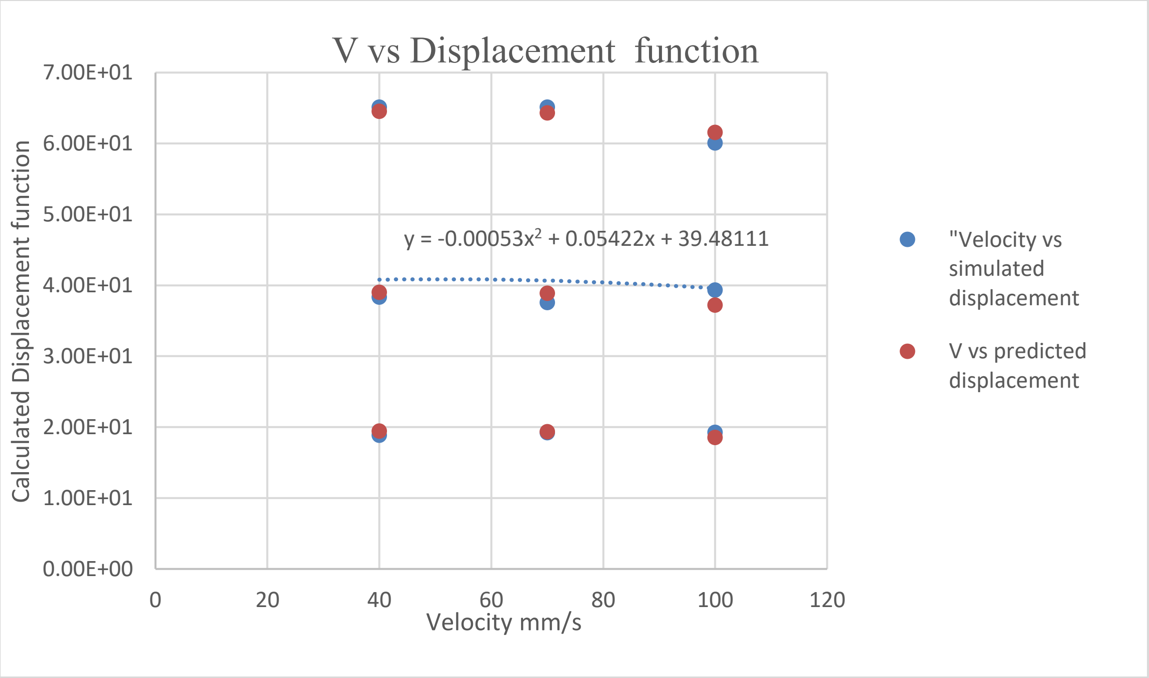

Figure 48 Graphical representation of laser power (W) vs displacement function, where blue dots indicate Power vs simulated displacement values, and orange dots indicate Power vs predicted displacement values

Now, let us look at the behaviour of process parameters on predicted displacement values. Fig 48 represents scanning speed vs the displacement function. The plotted curve shows a non-linear dependence of displacement on scanning speed because initially the displacement function increases with velocity and then decreases. Another interesting feature of this graph is that overlapping data points and a randomly scattered plot make it difficult to find the relationship between velocity and displacement.

Fig 49 represents displacement vs laser power (W) also shows a **nonlinear trend** because initially the displacement function increases with power and then decreases very slightly. Unlike the scattered behaviour or values in the scanning speed vs displacement function, the power vs displacement function shows a clear upward trend.

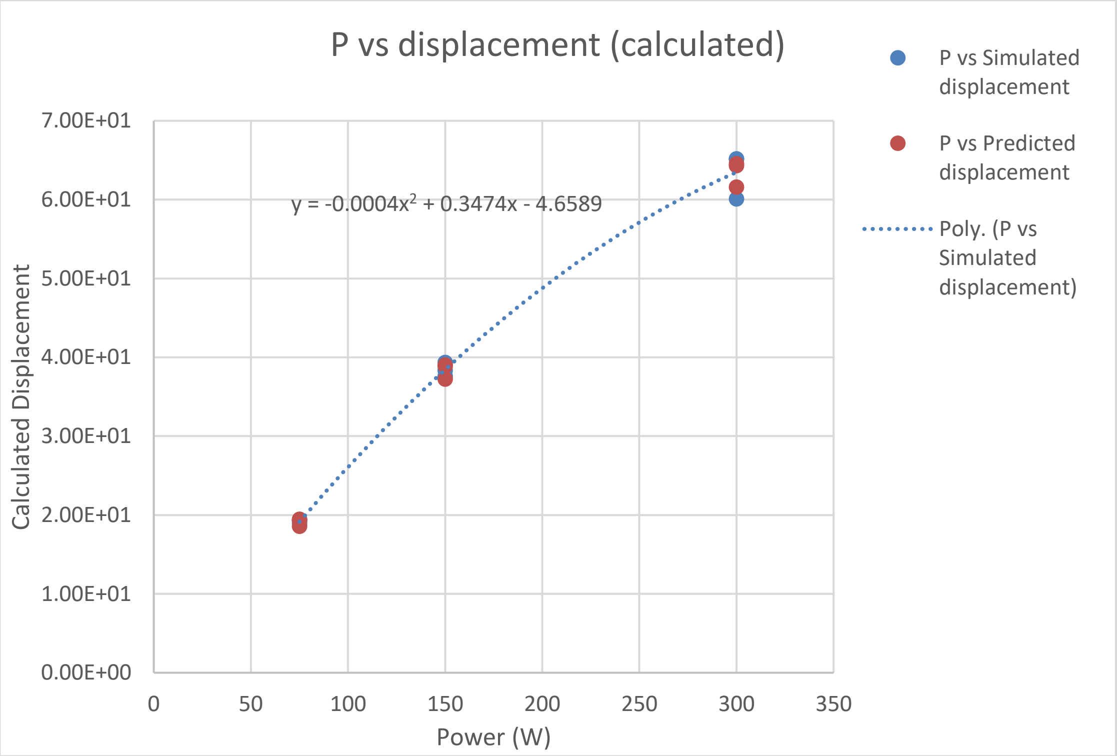

Figure 49 Graphical representation of laser power (W) vs displacement function where blue dots indicate Power vs simulated displacement values and orange dots indicate Power vs predicted displacement values

Discussions

- There is a key difference in the simulated and predicted displacement values. The lowest predicted displacement is at v= 100mm/s, and P= 75W the predicted displacement value reaching approximately 1.855×10^{-2}mm. However, in simulation values the combination V= 400mm/s, and P= 75 W shows the lowest observed displacement. There could be few reasons for this
  (1) RSM being a smooth mathematical fit which is technically an approximation so it might fail to capture localised nonlinear behaviour that FEM can.
  (2) Furthermore, simulation captures more detailed physics of thermal and mechanical feedback, leading to lower deformation at low scanning speeds due to longer cooling times and reduced stress.
- The highest predicted displacement value lies at 6.45×10^{-2} mm at V= 400 mm/s P= 300W due to RSM´´s sensitivity to nuanced trends.
- When plotted against laser power, displacement shows an upward trend as opposed to scanning speed, which shows a scattered data distribution. This could suggest that laser power has a more dominant influence on deformations, indicating higher power leads to higher displacements. Scan speed on the other hand might have a lesser influence or it could be dependent on the laser power. Thus, deformation should be considered a result a complex relationship between P, V parameters rather than its effects in isolation.
- Both the shallow melt pools from section 4.1 with process parameter combinations of V= 400 mm/s, P= 75W, and V= 1000 mm/s, P= 75W, respectively, also show the lowest displacement in both prediction and simulated deformation analysis. Melt pools with lower displacement values might be dimensionally accurate, have less residual stress, and improved fatigue life, but if they are too shallow, it can cause other defects, such as lack of fusion, that may compromise the part's integrity. Therefore, it is not sufficient to base a study on a single type of defect; a comprehensive evaluation considering multiple defect types is essential for process optimization.

4.3 Interpretation of Q learning results

To visualize the agent’s learning progression over time, the total reward per episode was plotted for 3 Configs, as represented in Table 12 in section 3.3. Additionally, a moving average (window size = 50) was applied to smooth fluctuations and highlight long-term trends. Fig. 50 represents a graph of the number of training episodes vs the reward obtained by the agent in each episode for Config A. We saw the convergence to happen gradually over time and stabilise with an increase in episodes. The agent has learned a reasonably good policy around episodes 25,000- 27,000 with a reward of 0.0528, so it stops exploring new actions that give better rewards and starts exploiting the optimal action. It starts getting consistent reward of 0.0538 for selecting the best state action pair i.e "increase in v and decrease in P", and V= 100 mm/s and P= 75W. There is also a noticeable staircase structure in the rewards space, which might suggest that the agent gets stuck in the local maxima; however, we can see the agent improving eventually in chunks.

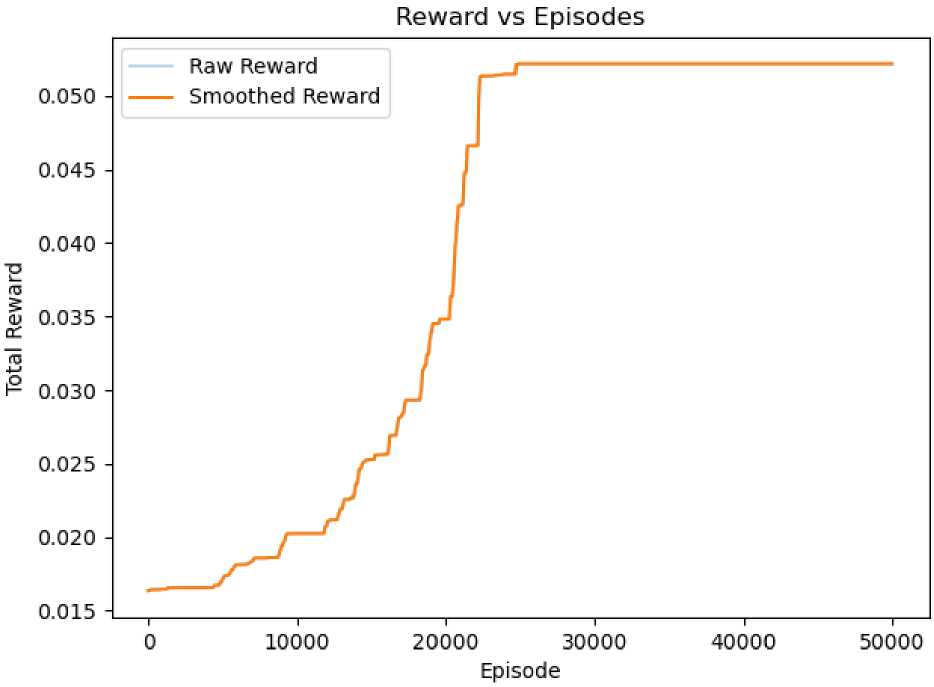

Figure 50 Graph for Rewards over 50,000 episodes. The hyperparameters are described in config A. The Graph shows convergence around episodes 25,000- 27,000 with a reward of 0.0528

In Fig. 51, the graphs of episodes vs rewards obtained for config B and C are shown. The agent has converged quite swiftly compared to config A, considering the number of episodes. The convergence occurs around episodes 28,000- 30,000 for config B and at 150000 for config C, which is quite early if we compare it to the number of episodes in it. It starts getting a consistent reward of 0.0538 for selecting the best action "increase in v and decrease in P", and the optimal state is V= 100 mm/s and P= 75W. Config B & C also show less staircase structure, which suggests less abrupt jumps in performance and stable convergence towards optimal policy. More episodes indicate longer training and finer updates to the Q values, allowing a more balanced exploration-exploitation tradeoff.

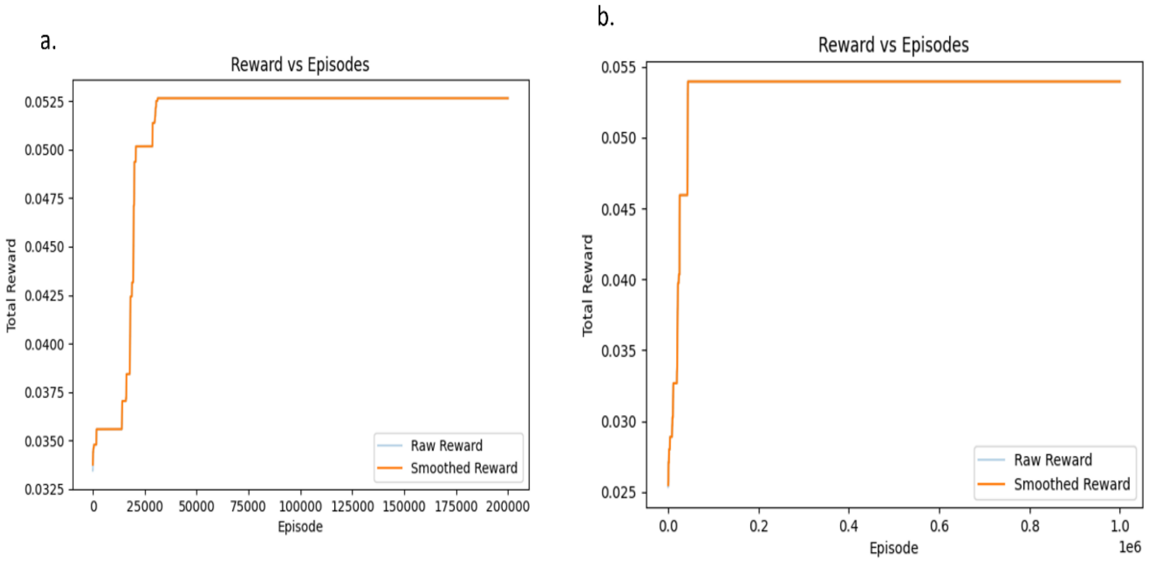

Figure 51 a. Graph for Rewards over 200000 episodes shows convergence around episodes 28,000- 30,000 with a reward of 0.0538. The hyperparameters are described in config B

b. Graph for Rewards over 1000000 episodes shows convergence around episodes 150000 with a reward of 0.0538.

Effect of hyperparameters on the convergence behaviour

For all 3 configurations mentioned in Table 12, the hyperparameters Exploration rate epsilon (ε), Discount factor (γ), and number of episodes were changed. However, learning rate (α), Max steps/episode, and Epsilon decay were left unchanged. The effect of each hyperparameter on the convergence behaviour of rewards vs episodes is discussed [7], [10]

Discount factor (γ): - In config A, when the discount factor (γ) is mid-range at 0.5. Slow and gradual convergence was observed, likely because the agent is neither too greedy nor too farsighted and prioritises stable learning. If the (γ) was too high, the agent would’ve had high fluctuation due to focus on long-term rewards, while if (γ) was too low, it would lead to a bad policy. In config C, when the discount factor is (γ) is at 0.7 the agent seems to converge the fastest; however, it is hard to know if it is due to the influence of only the discount factor, or increase in episodes or the exploration (ε) rate. Hence, it is safe to say that mid-range (γ) between 0.5- 0.7 is optimal.

Exploration rate (ε): - From Config A, B, and C that the exploration rate has been set to the values 0.2, 0,4, and 0.7, respectively. As observed, the convergence increases with an increase in exploration rate ε. Over time, ε was decayed multiplicatively by a factor of 0.9995 so that the agent becomes more confident and relies on greedy action selection, hence gaining more stable convergence.

No of Episodes: - Increase in the no of episodes was increased gradually. Higher episodes lead to faster convergence, a smoother curve, and less staircase structure. Hence increase in episodes also contributes to stable learning and improvement in policy learning.

Discussions

- The total reward per episode was plotted for 3 Configurations, which show quicker convergence with changes in different hyperparameter values, suggesting that this algorithm shows good learning behavior. All three configurations consistently converged to the best state action pair to be “increase in v and decrease in P” and V= 100 mm/s and P= 75W, thereby aligning with the intended outcome of the reward function.
- The stabilization of the reward values toward the later episodes confirms that the Q-learning algorithm successfully converged toward an optimal policy, where the agent consistently selected high-reward actions in known good regions of the state space.
- In Config A, B, C, the hyperparameter Exploration rate epsilon (ε), Discount factor (γ), and number of episodes were increased, and all encouraged rapid convergence; however more in-depth study is required to know if the increase in convergence is due to the influence of individual parameters or all hyperparameters together.
- The best state in the algorithm is v= 100 and P= 75 W with the high rewards between 0.00528- 0.00538. The algorithm is successfully learning that the lowest displacement will be at these values and it matches our predicted values using RSM.
- This algorithm is still quite computationally intensive, especially when the number of episodes were increased to 1000000 for Q learning. Basic Q learning is a tabular method suitable for small action spaces and does not work well with large datasets. If we plan to expand this research more with structural RL algorithms or Deep Q networks combined with a neural network will be beneficial[106].

5 Conclusions and Limitations

This study successfully met its primary objectives centred around understanding melt pool behaviour, simulating melt pool depth and powder bed fusion process, and building a control system for selecting optimal melt pool values to minimise deformation.

We introduced the concept and working principle of L-PBF, recognised the significance of melt pool dynamics and studied how variation in process parameters can lead to formation of defects. We also highlighted the importance of process monitoring and optimization and outlined the significant machine learning methods discussed in literature to achieve this.

Some important insights we gained from fulfilling our objectives include: -

1. Simulation of melt pool depth using Flow 3D and prediction and validation of melt pool depth through Response surface methodology (RSM).
    - The melt pool profiles were simulated and predicted for nine combinations of laser power and scan velocity. Both Flow 3d simulations and RSM captured the relationship between process parameters and melt pool depths effectively and in agreement with each other.
    - Optimal depths were seen at moderately high powers (P) and moderately high scan speed (V). This reduced the need for extensive physical experimentation, significantly saving time and resources.
2. Simulating the L-PBF process using FEM and studying the resulting deformations. Through the structural simulations in Abaqus, we found the displacement magnitude which indicated the highest and lowest deformations in our L-PBF process. Through RSM we were statistically able to validate these displacement values and compare both responses.
    - The predicted and simulated displacements although being close in values differed in deformation trends, likely due to the RSM making smooth approximations while FEM capturing detailed physical phenomena.
    - Low deformation is observed at high scan speeds and low power, they may lead to other defects, highlighting the need to balance deformation with other defects for improved part quality.
3. Control System design was developed by using Q-learning algorithm which is a reinforcement learning method to learn the optimal scan speed and laser power for minimizing displacement.

- The method successfully converged to the most favourable state action parameter set (v = 100 mm/s, P = 75 W and an increase in V decrease p), matching well with results predicted using Response Surface Methodology (RSM), indicating the effectiveness of the learning approach.
- Hyperparameters such as Exploration rate (ε), Discount factor (γ), and number of episodes showed accelerated learning behaviour and converged quickly as they were slightly increased.
- Despite being successful, this tabular Q-learning approach was computationally intensive especially when the number of episodes was increased to 1000000 and future implementations would benefit from using more advanced and scalable methods such as Deep Q-Networks (DQNs) coupled with neural networks or other structurally guided reinforcement learning techniques[106].

The implementation of simulation and reinforcement learning strategies was surely successful, although some limitations were identified.

1. The material behaviour used both in simulations such as uniform thermal properties and simplified phase changes was simplified, approximated and taken from academic publications, which may not fully capture real-world complexities. The powder bed simulated using Discrete element method were oversimplified due to values taken from peer reviewed literature instead of proper qualitative and quantitative validation. This indicates that more in-depth long-term research needs to be applied on this study.
2. Even though laser power and scan speed are the most common process parameters considered in literature for process optimization and building control systems for L-PBF only focusing on two primary parameters may not be enough.
3. The current use of tabular methods like Response Surface Methodology (RSM) works well for simple cases with limited process parameters, but it might not work the same in more complex situations when many parameters are involved.
4. Simulation-based learning provides valuable insights, however experimental validation remains essential to ensure the real-world applicability and domain adaptation of the learned policy. Bridging the gap between simulated and physical data will help improve reliability and robustness of the control system.

5. Although Q-learning successfully showed convergence through the rewards vs. episodes graphical analysis, it is just one aspect of the evaluation of the learning dynamics of this method, hence a more comprehensive analysis is needed. This was beyond the scope of this study however, due to time constraints. Future work on hyperparameter interdependency, state map visualisation, Q table heat map should be studied to assess the algorithm's performance and robustness. Moreover, the control system we created is more passive and tedious as it depends on offline analysis. Hence, a real-time feedback system is needed to enable continuous monitoring and simultaneous adjustment of process parameters, thereby reducing defects as they occur.

6 References

[1] A. Haleem and M. Javaid, “Additive Manufacturing Applications in Industry 4.0: A Review,” *J. Ind. Integr. Manag.*, vol. 04, no. 04, p. 1930001, Dec. 2019, doi: 10.1142/S2424862219300011.

[2] Haapa, Erik, “Simulation of metal powder packing behaviour in laser-based powder bed fusion,” University of turku, 2023. [Online]. Available: https://www.utupub.fi/handle/10024/174459

[3] T. Herzog, M. Brandt, A. Trinchi, A. Sola, and A. Molotnikov, “Process monitoring and machine learning for defect detection in laser-based metal additive manufacturing,” *J. Intell. Manuf.*, Apr. 2023, doi: 10.1007/s10845-023-02119-y.

[4] M. Mani, B. M. Lane, M. A. Donmez, S. C. Feng, and S. P. Moylan, “A review on measurement science needs for real-time control of additive manufacturing metal powder bed fusion processes,” *Int. J. Prod. Res.*, vol. 55, no. 5, pp. 1400–1418, Mar. 2017, doi: 10.1080/00207543.2016.1223378.

[5] A. Khaimovich, A. Balyakin, M. Oleynik, A. Meshkov, and V. Smelov, “Optimization of Process Parameters for Powder Bed Fusion Additive Manufacturing Using a Linear Programming Method: A Conceptual Framework,” *Metals*, vol. 12, no. 11, Art. no. 11, Nov. 2022, doi: 10.3390/met12111976.

[6] Z. Chen, “Understanding of the Modeling Method in Additive Manufacturing,” *IOP Conf. Ser. Mater. Sci. Eng.*, vol. 711, no. 1, p. 012017, Jan. 2020, doi: 10.1088/1757-899X/711/1/012017.

[7] S. Dharmadhikari, N. Menon, and A. Basak, “A reinforcement learning approach for process parameter optimization in additive manufacturing,” *Addit. Manuf.*, vol. 71, p. 103556, Jun. 2023, doi: 10.1016/j.addma.2023.103556.

[8] C. Reiff, W. Bubeck, D. Krawczyk, M. Steeb, A. Lechler, and A. Verl, “Learning Feedforward Control for Laser Powder Bed Fusion,” *Procedia CIRP*, vol. 96, pp. 127–132, Jan. 2021, doi: 10.1016/j.procir.2021.01.064.

[9] C. Wang, X. P. Tan, S. B. Tor, and C. S. Lim, “Machine learning in additive manufacturing: State-of-the-art and perspectives,” *Addit. Manuf.*, vol. 36, p. 101538, Dec. 2020, doi: 10.1016/j.addma.2020.101538.

[10] R. Sutton and A. Barto, *Reinforcement Learning*, Second. Accessed: Nov. 02, 2023. [Online]. Available: https://mitpress.mit.edu/9780262039246/reinforcement-learning/

[11] D. Horst, C. Duvoisin, and R. Vieira, “Additive Manufacturing at Industry 4.0: a Review,” *Int. J. Eng. Tech. Res.*, vol. 8, pp. 3–8, Sep. 2018.

[12] F. Ogoke and A. B. Farimani, “Thermal control of laser powder bed fusion using deep reinforcement learning,” *Addit. Manuf.*, vol. 46, p. 102033, Oct. 2021, doi: 10.1016/j.addma.2021.102033.

[13] T. DebRoy *et al.*, “Additive manufacturing of metallic components – Process, structure and properties,” *Prog. Mater. Sci.*, vol. 92, pp. 112–224, Mar. 2018, doi: 10.1016/j.pmatsci.2017.10.001.

[14] I. Gibson, D. Rosen, and B. Stucker, *Additive Manufacturing Technologies: 3D Printing, Rapid Prototyping, and Direct Digital Manufacturing*. New York, NY: Springer, 2015. doi: 10.1007/978-1-4939-2113-3.

[15] L. Yang *et al.*, “Introduction to Additive Manufacturing,” in *Additive Manufacturing of Metals: The Technology, Materials, Design and Production*, L. Yang, K. Hsu, B. Baughman, D. Godfrey, F. Medina, M. Menon, and S. Wiener, Eds., Cham: Springer International Publishing, 2017, pp. 1–31. doi: 10.1007/978-3-319-55128-9_1.

[16] M. A. Mahmood, C. Diana, A. Ur Rehman, S. Mihai, and A. Popescu, “Post-Processing Techniques to Enhance the Quality of Metallic Parts Produced by Additive

Manufacturing," *Met. - Open Access Metall. J.*, vol. 12, p. 77, Jan. 2022, doi: 10.3390/met12010077.

[17] D. Lu, Z. Liu, X. Wei, C. Chen, and D. Wang, "Effect of post-processing methods on the surface quality of Ti6Al4V fabricated by laser powder bed fusion," *Front. Mater.*, vol. 10, Feb. 2023, doi: 10.3389/fmats.2023.1126749.

[18] X. Peng, L. Kong, J. Y. H. Fuh, and H. Wang, "A Review of Post-Processing Technologies in Additive Manufacturing," *J. Manuf. Mater. Process.*, vol. 5, no. 2, Art. no. 2, Jun. 2021, doi: 10.3390/jmmp5020038.

[19] "INTERNATIONAL STANDARD ISO/ASTM 52900."

[20] F. Zhang *et al.*, "The recent development of vat photopolymerization: A review," *Addit. Manuf.*, vol. 48, p. 102423, Dec. 2021, doi: 10.1016/j.addma.2021.102423.

[21] M. Rafiee, R. D. Farahani, and D. Therriault, "Multi-Material 3D and 4D Printing: A Survey," *Adv. Sci.*, vol. 7, no. 12, p. 1902307, 2020, doi: 10.1002/advs.201902307.

[22] D. Dev Singh, T. Mahender, and A. Raji Reddy, "Powder bed fusion process: A brief review," *Mater. Today Proc.*, vol. 46, pp. 350–355, Jan. 2021, doi: 10.1016/j.matpr.2020.08.415.

[23] A. Awad, F. Fina, A. Goyanes, S. Gaisford, and A. W. Basit, "Advances in powder bed fusion 3D printing in drug delivery and healthcare," *Adv. Drug Deliv. Rev.*, vol. 174, pp. 406–424, Jul. 2021, doi: 10.1016/j.addr.2021.04.025.

[24] S. Chokshi *et al.*, "Medical 3D Printing Using Material Jetting: Technology Overview, Medical Applications, and Challenges," *Bioengineering*, vol. 12, no. 3, p. 249, Feb. 2025, doi: 10.3390/bioengineering12030249.

[25] O. Gülcan, K. Günaydın, and A. Tamer, "The State of the Art of Material Jetting—A Critical Review," *Polymers*, vol. 13, no. 16, Art. no. 16, Jan. 2021, doi: 10.3390/polym13162829.

[26] W. Du, X. Ren, Z. Pei, and C. Ma, "Ceramic Binder Jetting Additive Manufacturing: A Literature Review on Density," *J. Manuf. Sci. Eng.*, vol. 142, no. 040801, Feb. 2020, doi: 10.1115/1.4046248.

[27] S. J. Trenfield, C. M. Madla, A. W. Basit, and S. Gaisford, "Binder Jet Printing in Pharmaceutical Manufacturing," in *3D Printing of Pharmaceuticals*, A. W. Basit and S. Gaisford, Eds., Cham: Springer International Publishing, 2018, pp. 41–54. doi: 10.1007/978-3-319-90755-0_3.

[28] G. Piscopo and L. Iuliano, "Current research and industrial application of laser powder directed energy deposition," *Int. J. Adv. Manuf. Technol.*, vol. 119, no. 11, pp. 6893–6917, Apr. 2022, doi: 10.1007/s00170-021-08596-w.

[29] D. Svetlizky *et al.*, "Directed energy deposition (DED) additive manufacturing: Physical characteristics, defects, challenges and applications," *Mater. Today*, vol. 49, pp. 271–295, Oct. 2021, doi: 10.1016/j.mattod.2021.03.020.

[30] A. Kumar, A. R. Dixit, and S. Sreenivasa, "Mechanical properties of additively manufactured polymeric composites using sheet lamination technique and fused deposition modeling: A review," *Polym. Adv. Technol.*, vol. 35, no. 4, p. e6396, Apr. 2024, doi: 10.1002/pat.6396.

[31] T. Obikawa, M. Yoshino, and J. Shinozuka, "Sheet steel lamination for rapid manufacturing," *J. Mater. Process. Technol.*, vol. 89–90, pp. 171–176, May 1999, doi: 10.1016/S0924-0136(99)00027-8.

[32] G. Hsiang Loh, E. Pei, J. Gonzalez-Gutierrez, and M. Monzón, "An Overview of Material Extrusion Troubleshooting," *Appl. Sci.*, vol. 10, no. 14, Art. no. 14, Jan. 2020, doi: 10.3390/app10144776.

[33] L. Chaunier, S. Guessasma, S. Belhabib, G. Della Valle, D. Lourdin, and E. Leroy, “Material extrusion of plant biopolymers: Opportunities & challenges for 3D printing,” *Addit. Manuf.*, vol. 21, pp. 220–233, May 2018, doi: 10.1016/j.addma.2018.03.016.

[34] S. Chowdhury *et al.*, “Laser powder bed fusion: a state-of-the-art review of the technology, materials, properties & defects, and numerical modelling,” *J. Mater. Res. Technol.*, vol. 20, pp. 2109–2172, Sep. 2022, doi: 10.1016/j.jmrt.2022.07.121.

[35] N. D. Dejene and H. G. Lemu, “Current Status and Challenges of Powder Bed Fusion-Based Metal Additive Manufacturing: Literature Review,” *Metals*, vol. 13, no. 2, Art. no. 2, Feb. 2023, doi: 10.3390/met13020424.

[36] R. Singh *et al.*, “Powder bed fusion process in additive manufacturing: An overview,” *Mater. Today Proc.*, vol. 26, pp. 3058–3070, Jan. 2020, doi: 10.1016/j.matpr.2020.02.635.

[37] Z. Wawryniuk, E. Brancewicz-Steinmetz, and J. Sawicki, “Revolutionizing transportation: an overview of 3D printing in aviation, automotive, and space industries,” *Int. J. Adv. Manuf. Technol.*, vol. 134, pp. 3083–3105, Sep. 2024, doi: 10.1007/s00170-024-14226-y.

[38] S. Rajinth, K. Chen, and C. Abeykoon, “Powder-Based Additive Manufacturing: A Critical Review of Materials, Methods, Opportunities, and Challenges,” *Adv. Eng. Mater.*, vol. 25, Jun. 2023, doi: 10.1002/adem.202300375.

[39] S. Zhe, “Computational fluid dynamics modelling of powder-based laser additive manufacturing processes,” University of manchester. Accessed: Nov. 01, 2023. [Online]. Available: https://research.manchester.ac.uk/en/studentTheses/computational-fluid-dynamics-modelling-of-powder-based-laser-addi

[40] S. Saedi, N. Shayesteh Moghaddam, A. Amerinatanzi, M. Elahinia, and H. E. Karaca, “On the effects of selective laser melting process parameters on microstructure and thermomechanical response of Ni-rich NiTi,” *Acta Mater.*, vol. 144, pp. 552–560, Feb. 2018, doi: 10.1016/j.actamat.2017.10.072.

[41] C. Y. Yap, C. K. Chua, and Z. L. Dong, “An effective analytical model of selective laser melting,” *Virtual Phys. Prototyp.*, vol. 11, no. 1, pp. 21–26, Jan. 2016, doi: 10.1080/17452759.2015.1133217.

[42] K. Wei, Z. Wang, and X. Zeng, “Influence of element vaporization on formability, composition, microstructure, and mechanical performance of the selective laser melted Mg–Zn–Zr components,” *Mater. Lett.*, vol. 156, pp. 187–190, Oct. 2015, doi: 10.1016/j.matlet.2015.05.074.

[43] J. Guan and Q. Wang, “Laser Powder Bed Fusion of Dissimilar Metal Materials: A Review,” *Materials*, vol. 16, no. 7, Art. no. 7, Jan. 2023, doi: 10.3390/ma16072757.

[44] D. Bourell *et al.*, “Materials for additive manufacturing,” *CIRP Ann.*, vol. 66, no. 2, pp. 659–681, Jan. 2017, doi: 10.1016/j.cirp.2017.05.009.

[45] P. Muthuswamy, “Influence of powder characteristics on properties of parts manufactured by metal additive manufacturing,” *Lasers Manuf. Mater. Process.*, vol. 9, no. 3, pp. 312–337, Sep. 2022, doi: 10.1007/s40516-022-00177-3.

[46] S. H. Saheb, V. K. Durgam, and A. Chandrashekhar, “A review on metal powders in additive manufacturing,” *AIP Conf. Proc.*, vol. 2281, no. 1, p. 020018, Oct. 2020, doi: 10.1063/5.0026203.

[47] Md. H. Ali, N. Sabyrov, and E. Shehab, “Powder bed fusion–laser melting (PBF–LM) process: latest review of materials, process parameter optimization, application, and up-to-date innovative technologies,” *Prog. Addit. Manuf.*, vol. 7, no. 6, pp. 1395–1422, Dec. 2022, doi: 10.1007/s40964-022-00311-9.

[48] M. Geetha, A. K. Singh, R. Asokamani, and A. K. Gogia, “Ti based biomaterials, the ultimate choice for orthopaedic implants – A review,” *Prog. Mater. Sci.*, vol. 54, no. 3, pp. 397–425, May 2009, doi: 10.1016/j.pmatsci.2008.06.004.

[49] S. Sanchez *et al.*, “Powder Bed Fusion of nickel-based superalloys: A review,” *Int. J. Mach. Tools Manuf.*, vol. 165, p. 103729, Jun. 2021, doi: 10.1016/j.ijmachtools.2021.103729.

[50] D. Carluccio, M. Bermingham, D. Kent, A. G. Demir, B. Previtali, and M. S. Dargusch, “Comparative Study of Pure Iron Manufactured by Selective Laser Melting, Laser Metal Deposition, and Casting Processes,” *Adv. Eng. Mater.*, vol. 21, no. 7, p. 1900049, 2019, doi: 10.1002/adem.201900049.

[51] J. Zhang, B. Song, Q. Wei, D. Bourell, and Y. Shi, “A review of selective laser melting of aluminum alloys: Processing, microstructure, property and developing trends,” *J. Mater. Sci. Technol.*, vol. 35, no. 2, pp. 270–284, Feb. 2019, doi: 10.1016/j.jmst.2018.09.004.

[52] A. Mostafaei *et al.*, “Defects and anomalies in powder bed fusion metal additive manufacturing,” *Curr. Opin. Solid State Mater. Sci.*, vol. 26, no. 2, p. 100974, Apr. 2022, doi: 10.1016/j.cossms.2021.100974.

[53] J. Wang, S. Liu, Y. Fang, and Z. He, “A short review on selective laser melting of H13 steel,” *Int. J. Adv. Manuf. Technol.*, vol. 108, no. 7, pp. 2453–2466, Jun. 2020, doi: 10.1007/s00170-020-05584-4.

[54] R. Li, J. Liu, Y. Shi, L. Wang, and W. Jiang, “Balling behavior of stainless steel and nickel powder during selective laser melting process,” *Int. J. Adv. Manuf. Technol.*, vol. 59, no. 9, pp. 1025–1035, Apr. 2012, doi: 10.1007/s00170-011-3566-1.

[55] Y. Huang *et al.*, “Keyhole fluctuation and pore formation mechanisms during laser powder bed fusion additive manufacturing,” *Nat. Commun.*, vol. 13, no. 1, p. 1170, Mar. 2022, doi: 10.1038/s41467-022-28694-x.

[56] L. Wang, Y. Zhang, H. Y. Chia, and W. Yan, “Mechanism of keyhole pore formation in metal additive manufacturing,” *Npj Comput. Mater.*, vol. 8, no. 1, pp. 1–11, Jan. 2022, doi: 10.1038/s41524-022-00699-6.

[57] L. Guo *et al.*, “Understanding keyhole induced-porosities in laser powder bed fusion of aluminum and elimination strategy,” *Int. J. Mach. Tools Manuf.*, vol. 184, p. 103977, Jan. 2023, doi: 10.1016/j.ijmachtools.2022.103977.

[58] H. Rezaeifar and M. Elbestawi, “Minimizing the surface roughness in L-PBF additive manufacturing process using a combined feedforward plus feedback control system,” *Int. J. Adv. Manuf. Technol.*, vol. 121, no. 11, pp. 7811–7831, Aug. 2022, doi: 10.1007/s00170-022-09902-w.

[59] E. Yasa, O. Poyraz, E. U. Solakoglu, G. Akbulut, and S. Oren, “A Study on the Stair Stepping Effect in Direct Metal Laser Sintering of a Nickel-based Superalloy,” *Procedia CIRP*, vol. 45, pp. 175–178, Jan. 2016, doi: 10.1016/j.procir.2016.02.068.

[60] R. A. Yildiz, C. Ozdogan, and M. Malekan, “On the surface roughness of 316L stainless steel fabricated using L-PBF additive manufacturing,” *Tribol. - Finn. J. Tribol.*, vol. 41, no. 3–4, Art. no. 3–4, Dec. 2024, doi: 10.30678/fjt.149389.

[61] J. Zhang, B. Song, Q. Wei, D. Bourell, and Y. Shi, “A review of selective laser melting of aluminum alloys: Processing, microstructure, property and developing trends,” *J. Mater. Sci. Technol.*, vol. 35, no. 2, pp. 270–284, Feb. 2019, doi: 10.1016/j.jmst.2018.09.004.

[62] M. Zhang *et al.*, “Fatigue and fracture behaviour of laser powder bed fusion stainless steel 316L: Influence of processing parameters,” *Mater. Sci. Eng. A*, vol. 703, pp. 251–261, Aug. 2017, doi: 10.1016/j.msea.2017.07.071.

[63] M. C. Brennan, J. S. Keist, and T. A. Palmer, “Defects in Metal Additive Manufacturing Processes,” *J. Mater. Eng. Perform.*, vol. 30, no. 7, pp. 4808–4818, Jul. 2021, doi: 10.1007/s11665-021-05919-6.

[64] M. Tang, P. C. Pistorius, and J. L. Beuth, "Prediction of lack-of-fusion porosity for powder bed fusion," *Addit. Manuf.*, vol. 14, pp. 39–48, Mar. 2017, doi: 10.1016/j.addma.2016.12.001.

[65] S. Cacace and Q. Semeraro, "On the Lack of fusion porosity in L-PBF processes," *Procedia CIRP*, vol. 112, pp. 352–357, Jan. 2022, doi: 10.1016/j.procir.2022.09.008.

[66] Z. Li *et al.*, "A Review of Spatter in Laser Powder Bed Fusion Additive Manufacturing: In Situ Detection, Generation, Effects, and Countermeasures," *Micromachines*, vol. 13, no. 8, Art. no. 8, Aug. 2022, doi: 10.3390/mi13081366.

[67] Y. Liu, Y. Yang, S. Mai, D. Wang, and C. Song, "Investigation into spatter behavior during selective laser melting of AISI 316L stainless steel powder," *Mater. Des.*, vol. 87, pp. 797–806, Dec. 2015, doi: 10.1016/j.matdes.2015.08.086.

[68] H. Chen, Y. Zhang, A. Giam, and W. Yan, "Experimental and computational study on thermal and fluid behaviours of powder layer during selective laser melting additive manufacturing," *Addit. Manuf.*, vol. 52, p. 102645, Apr. 2022, doi: 10.1016/j.addma.2022.102645.

[69] S. Luo, X. Ma, J. Xu, M. Li, and L. Cao, "Deep Learning Based Monitoring of Spatter Behavior by the Acoustic Signal in Selective Laser Melting," *Sensors*, vol. 21, no. 21, Art. no. 21, Jan. 2021, doi: 10.3390/s21217179.

[70] EUGENIO OÑATE, PEDRO DÍEZ, FRANCISCO ZÁRATE, and ANTONIA LARESE, *INTRODUCTION TO THE FINITE ELEMENT METHOD*. 2008.

[71] X. Song *et al.*, "Advances in additive manufacturing process simulation: Residual stresses and distortion predictions in complex metallic components," *Mater. Des.*, vol. 193, p. 108779, Aug. 2020, doi: 10.1016/j.matdes.2020.108779.

[72] Y. Yan, D. Wu, and Q. Li, "A three-dimensional method for the simulation of temperature fields induced by solar radiation," *Adv. Struct. Eng.*, vol. 22, no. 3, pp. 567–580, Feb. 2019, doi: 10.1177/1369433218795254.

[73] R. Ullah, J. Lian, J. S. Akmal, J. Wu, and E. Niemi, "Prediction and validation of melt pool dimensions and geometric distortions of additively manufactured AlSi10Mg," Jun. 2023, doi: 10.1007/s00170-023-11264-w.

[74] M. Grasso, A. Remani, A. Dickins, B. M. Colosimo, and R. K. Leach, "In-situ measurement and monitoring methods for metal powder bed fusion: an updated review," *Meas. Sci. Technol.*, vol. 32, no. 11, p. 112001, Jul. 2021, doi: 10.1088/1361-6501/ac0b6b.

[75] P. Yadav, O. Rigo, C. Arvieu, E. Le Guen, and E. Lacoste, "In Situ Monitoring Systems of The SLM Process: On the Need to Develop Machine Learning Models for Data Processing," *Crystals*, vol. 10, no. 6, Art. no. 6, Jun. 2020, doi: 10.3390/cryst10060524.

[76] D. Mahmoud, M. Magolon, J. Boer, M. A. Elbestawi, and M. G. Mohammadi, "Applications of Machine Learning in Process Monitoring and Controls of L-PBF Additive Manufacturing: A Review," *Appl. Sci.*, vol. 11, no. 24, Art. no. 24, Jan. 2021, doi: 10.3390/app112411910.

[77] L. Scime and J. Beuth, "Anomaly detection and classification in a laser powder bed additive manufacturing process using a trained computer vision algorithm," *Addit. Manuf.*, vol. 19, pp. 114–126, Jan. 2018, doi: 10.1016/j.addma.2017.11.009.

[78] L. Scime and J. Beuth, "Using machine learning to identify in-situ melt pool signatures indicative of flaw formation in a laser powder bed fusion additive manufacturing process," *Addit. Manuf.*, vol. 25, pp. 151–165, Jan. 2019, doi: 10.1016/j.addma.2018.11.010.

[79] A. Paul *et al.*, *A real-time iterative machine learning approach for temperature profile prediction in additive manufacturing processes*. 2019.

[80] L. Chen *et al.*, “In-situ process monitoring and adaptive quality enhancement in laser additive manufacturing: A critical review,” *J. Manuf. Syst.*, vol. 74, pp. 527–574, Jun. 2024, doi: 10.1016/j.jmsy.2024.04.013.

[81] B. Yao, F. Imani, and H. Yang, “Markov Decision Process for Image-Guided Additive Manufacturing,” *IEEE Robot. Autom. Lett.*, vol. 3, no. 4, pp. 2792–2798, Oct. 2018, doi: 10.1109/LRA.2018.2839973.

[82] G. Masinelli, S. A. Shevchik, V. Pandiyan, T. Quang-Le, and K. Wasmer, “Artificial Intelligence for Monitoring and Control of Metal Additive Manufacturing,” in *Industrializing Additive Manufacturing*, M. Meboldt and C. Klahn, Eds., Cham: Springer International Publishing, 2021, pp. 205–220. doi: 10.1007/978-3-030-54334-1_15.

[83] K. Wasmer, C. Kenel, C. Leinenbach, and S. A. Shevchik, “In Situ and Real-Time Monitoring of Powder-Bed AM by Combining Acoustic Emission and Artificial Intelligence,” in *Industrializing Additive Manufacturing - Proceedings of Additive Manufacturing in Products and Applications - AMPA2017*, M. Meboldt and C. Klahn, Eds., Cham: Springer International Publishing, 2018, pp. 200–209. doi: 10.1007/978-3-319-66866-6_20.

[84] J. Wang, R. Zhu, Y. Liu, and L. Zhang, “Understanding melt pool characteristics in laser powder bed fusion: An overview of single- and multi-track melt pools for process optimization,” *Adv. Powder Mater.*, vol. 2, no. 4, p. 100137, Oct. 2023, doi: 10.1016/j.apmate.2023.100137.

[85] M. N. Dogu *et al.*, “Digitisation of metal AM for part microstructure and property control,” *Int. J. Mater. Form.*, vol. 15, no. 3, p. 30, Apr. 2022, doi: 10.1007/s12289-022-01686-4.

[86] J. Yang *et al.*, “Role of molten pool mode on formability, microstructure and mechanical properties of selective laser melted Ti-6Al-4V alloy,” *Mater. Des.*, vol. 110, pp. 558–570, Nov. 2016, doi: 10.1016/j.matdes.2016.08.036.

[87] M. A. Chaudry, G. Mohr, and K. Hilgenberg, “Experimental and numerical comparison of heat accumulation during laser powder bed fusion of 316L stainless steel,” *Prog. Addit. Manuf.*, vol. 7, no. 5, pp. 1071–1083, Oct. 2022, doi: 10.1007/s40964-022-00282-x.

[88] FLOW-3D [Computer software]. Santa Fe, NM: Flow Science, Inc, “FLOW-3D® AM Version 2023R1 Users Manual (2023).” [Online]. Available: https://www.flow3d.com

[89] X. Jiang, “Stirring Performance Analysis Based on the Influence of Mechanics and Stirred Mill Environment,” *Math. Probl. Eng.*, vol. 2022, no. 1, p. 8077424, 2022, doi: 10.1155/2022/8077424.

[90] FLOW-3D [Computer software]. Santa Fe, NM: Flow Science, Inc., “FLOW-3D®DEM Version 2023R1 Users Manual (2023).” [Online]. Available: https://www.flow3d.com

[91] P. W. Cleary, “DEM prediction of industrial and geophysical particle flows,” *Particuology*, vol. 8, no. 2, pp. 106–118, Apr. 2010, doi: 10.1016/j.partic.2009.05.006.

[92] M. A. Mahmood, A. Ur Rehman, M. M. Azeem, A. Alkhouzaam, and M. Khraisheh, “On the development of part-scale FEM modeling for laser powder bed fusion of AISI 316L stainless steel with experimental verification,” *Int. J. Adv. Manuf. Technol.*, vol. 127, no. 5, pp. 2229–2255, Jul. 2023, doi: 10.1007/s00170-023-11572-1.

[93] D. Yao *et al.*, “Numerical insights on the spreading of practical 316 L stainless steel powder in SLM additive manufacturing,” *Powder Technol.*, vol. 390, pp. 197–208, Sep. 2021, doi: 10.1016/j.powtec.2021.05.082.

[94] Y. S. Lee, P. Nandwana, and W. Zhang, “Dynamic simulation of powder packing structure for powder bed additive manufacturing,” *Int. J. Adv. Manuf. Technol.*, vol. 96, no. 1, pp. 1507–1520, Apr. 2018, doi: 10.1007/s00170-018-1697-3.

[95] J. Zegzulka, D. Gelnar, L. Jezerska, A. Ramirez-Gomez, J. Necas, and J. Rozbroj, “Internal Friction Angle of Metal Powders,” *Metals*, vol. 8, no. 4, Art. no. 4, Apr. 2018, doi: 10.3390/met8040255.

[96] Horiba Scientific, “A Guidebook to particle Size analysis.”

[97] A. Özcan, S. Kollmannsberger, J. Jomo, and E. Rank, *Residual stresses in metal deposition modeling: discretizations of higher order*. 2018. doi: 10.48550/arXiv.1809.07663.

[98] Flow science, “FLOW-3D®WELD Version 2023R1 software (2023). FLOW-3D [Computer software]. Santa Fe, NM: Flow Science, Inc.” [Online]. Available: https://www.flow3d.com

[99] “Abaqus/CAE User’s Guide (2016),” Getting started with Abaqus/CAE. Accessed: Jul. 23, 2025. [Online]. Available: http://130.149.89.49:2080/v2016/books/usi/default.htm

[100] K.-Hyun. Lee and G. J. Yun, “A novel heat source model for analysis of melt Pool evolution in selective laser melting process,” *Addit. Manuf.*, vol. 36, p. 101497, Dec. 2020, doi: 10.1016/j.addma.2020.101497.

[101] A. Kiran, Y. Li, J. Hodek, M. Brázda, M. Urbánek, and J. Džugan, “Heat Source Modeling and Residual Stress Analysis for Metal Directed Energy Deposition Additive Manufacturing,” *Materials*, vol. 15, no. 7, p. 2545, Mar. 2022, doi: 10.3390/ma15072545.

[102] B. Li, J. Du, Y. Sun, S. Zhang, and Q. Zhang, “On the importance of heat source model determination for numerical modeling of selective laser melting of IN625,” *Opt. Laser Technol.*, vol. 158, p. 108806, Feb. 2023, doi: 10.1016/j.optlastec.2022.108806.

[103] N. An, G. Yang, K. Yang, J. Wang, M. Li, and J. Zhou, “Implementation of Abaqus user subroutines and plugin for thermal analysis of powder-bed electron-beam-melting additive manufacturing process,” *Mater. Today Commun.*, vol. 27, p. 102307, Jun. 2021, doi: 10.1016/j.mtcomm.2021.102307.

[104] N. Bradley, “THE RESPONSE SURFACE METHODOLOGY,” Indiana university of South bend, 2007. [Online]. Available: https://hdl.handle.net/2022/16795

[105] S. Lamidi *et al.*, “Applications of Response Surface Methodology (RSM) in Product Design, Development, and Process Optimization,” in *Response Surface Methodology - Research Advances and Applications*, IntechOpen, 2022. doi: 10.5772/intechopen.106763.

[106] J. Dornheim, L. Morand, S. Zeitvogel, T. Iraki, N. Link, and D. Helm, “Deep reinforcement learning methods for structure-guided processing path optimization,” *J. Intell. Manuf.*, vol. 33, no. 1, pp. 333–352, Jan. 2022, doi: 10.1007/s10845-021-01805-z.

7 Appendix 1

A. Q learning code used to created control policy

```
import numpy as np
import random
import matplotlib.pyplot as plt
import seaborn as sns

# Constants
a1, b1, c1 = -5.33335E-05, 0.005571812, 2.321736449
a2, b2, c2 = -0.000164653, 0.143259306, -1.908263576

def random_argmax(array):
    max_value = np.max(array)
    max_indices = np.where(array == max_value)[0]
    return random.choice(max_indices)

# Ranges
v_range = np.arange(40, 101, 1) #610 values in state space v
P_range = np.arange(75, 301, 1) #2260 values in state space P Total values are 610*2260= 13786000 in (p,V)

# Parameters
epsilon = 0.2
epsilon_decay = 0.9995
alpha = 0.01
gamma = 0.5
num_episodes = 50000
max_steps = 8

#  MODIFIED reward function
def reward_function(v, P):
    f = (a1 * v**2 + b1 * v + c1) * (a2 * P**2 + b2 * P + c2)
    if f > 0:
        return np.tanh(1 / f)  # for Smoothed positive reward
    else:
        return -1 / (1 + abs(f))  #for Scaled smooth penalty

episode_rewards = []
```

```
# Actions
actions = [
    ('increase_v', 'decrease_P'),
    ('increase_v', 'increase_P'),
    ('decrease_v', 'decrease_P'),
    ('decrease_v', 'increase_P'),
    ('increase_v', 'no_change_P'),
    ('decrease_v', 'no_change_P'),
    ('no_change_v', 'increase_P'),
    ('no_change_v', 'decrease_P'),
    ('no_change_v', 'no_change_P')
]

Q_table = np.ones((len(v_range), len(P_range), len(actions)))* 10.0 # Initialize Q-table with high values

best_seen_reward = -float('inf')
best_state_from_training = None


break_var=0


# Q-learning
for episode in range(num_episodes):
    if break_var==0:
        v = random.choice(v_range) # Randomly select initial v
        P = random.choice(P_range) # Randomly select initial p
        reward = reward_function(v, P)
        total_reward = 0
        break_var+=1

    for step in range(max_steps):
        v_index = np.where(v_range == v)[0][0] # Get index of current v
        P_index = np.where(P_range == P)[0][0] # Get index of current p
        indexdeltav = 1
        indexdelta = 1

        if np.random.rand() < epsilon:
            action_index = random.choice(range(len(actions)))
```

```
        else:
            action_index = random_argmax(Q_table[v_index, P_index])

        action = actions[action_index]

        if v_index + indexdeltav <= 610 & v_index - indexdeltav >= 0:
            indexdeltav = int(reward/best_seen_reward) #index delta v should increase if the reward is large compared to best seen reward and decrease if opposite
        else:
            indexdeltav = 1

        if P_index + indexdelta <= 2260 & P_index - indexdelta >= 0:
            indexdelta = int(reward/best_seen_reward) #index delta p should increase if the reward is large compared to best seen reward and decrease if opposite
        else:
            indexdelta = 1

        if action == ('increase_v', 'decrease_P'): # Defining Action values
            v = v_range[v_index + indexdeltav] if v_index + 1 < len(v_range) else v
            P = P_range[P_index - indexdelta] if P_index > 0 else P
        elif action == ('increase_v', 'increase_P'):
            v = v_range[v_index + indexdeltav] if v_index + 1 < len(v_range) else v
            P = P_range[P_index + indexdelta] if P_index + 1 < len(P_range) else P
        elif action == ('decrease_v', 'decrease_P'):
            v = v_range[v_index - indexdeltav] if v_index > 0 else v
            P = P_range[P_index - indexdelta] if P_index > 0 else P
        elif action == ('decrease_v', 'increase_P'):
            v = v_range[v_index - indexdeltav] if v_index > 0 else v
            P = P_range[P_index + indexdelta] if P_index + 1 < len(P_range) else P
        elif action == ('increase_v', 'no_change_P'):
            v = v_range[v_index + indexdeltav] if v_index + 1 < len(v_range) else v
        elif action == ('decrease_v', 'no_change_P'):
            v = v_range[v_index - indexdeltav] if v_index > 0 else v
        elif action == ('no_change_v', 'increase_P'):
            P = P_range[P_index + indexdelta] if P_index + 1 < len(P_range) else P
        elif action == ('no_change_v', 'decrease_P'):
            P = P_range[P_index - indexdelta] if P_index > 0 else P

        v = max(min(v, v_range[-1]), v_range[0])
        P = max(min(P, P_range[-1]), P_range[0])
```

```
        # EARLY TERMINATION + reward improvement
        reward = reward_function(v, P)
        total_reward += reward

        print(f"Episode: {episode}, Step: {step}, Action: {action}")
        print(f"Reward: {reward}")

        if reward > best_seen_reward:
            best_seen_reward = reward
            best_state_from_training = (v, P)
            best_action = actions[action_index]

        next_v_index = np.where(v_range == v)[0][0]
        next_P_index = np.where(P_range == P)[0][0]


 Q_table[v_index, P_index, action_index] += alpha * ( reward + gamma *
np.max(Q_table[next_v_index, next_P_index]) - Q_table[v_index, P_index, action_index]
        )

        # TERMINATE episode early if penalty state
        if reward < 0:
            break_var=1
            # Optional final update if terminating
            break

    epsilon = max(0.01, epsilon * epsilon_decay)
    episode_rewards.append(best_seen_rewar
# Plotting
def moving_average(data, window_size):
    return np.convolve(data, np.ones(window_size)/window_size, mode='valid')

smoothed_rewards = moving_average(episode_rewards, window_size=50)

plt.figure(figsize=(7, 5))
plt.plot(episode_rewards, alpha=0.3, label='Raw Reward')
plt.plot(smoothed_rewards, label='Smoothed Reward')
plt.xlabel('Episode')
plt.ylabel('Total Reward')
```

```
plt.title('Reward vs Episodes')
plt.legend()
plt.show()

# Final printout
print("\n🎯 Best reward seen during training:")
print(f"Best reward: {best_seen_reward} at state: v={best_state_from_training[0]}, P={best_state_from_training[1]}")
```

B. **Material properties of SS316L used in Abaqus simulation** [92], [97]

The material properties of SS316L stainless steel, essential for accurately modeling thermal and mechanical behavior during L-PBF, were sourced from literature and incorporated into the Abaqus simulation [91], [96]

Temperature (K)	**Thermal Conductivity (k) (W/m·K)**	**Young's Modulus (E) (MPa)**	**Poisson's Ratio (ν)**	**Expansion Coefficient (1/K) (α)**	**Specific Heat (cp)(J/kg·K)**
293	14.12	195600	0.3	1.45E-05	4.9E+08
373	15.26	191200	0.3	1.54E-05	5.0E+08
473	16.69	185400	0.3	1.62E-05	5.1E+08
573	18.11	179600	0.3	1.69E-05	5.3E+08
673	19.54	172600	0.3	1.74E-05	5.4E+08
773	20.96	164500	0.3	1.78E-05	5.5E+08
873	22.38	155000	0.3	1.81E-05	5.6E+08
973	23.81	144100	0.3	1.84E-05	5.7E+08
1073	25.23	131400	0.3	1.87E-05	5.9E+08
1173	26.66	116800	0.3	1.90E-05	6.1E+08
1273	28.08	100000	0.3	1.93E-05	6.2E+08
1373	29.50	80000	0.3	1.95E-05	6.4E+08
1473	30.93	57000	0.3	1.98E-05	6.4E+08
1573	32.35	30000	0.3	2.00E-05	6.5E+08
1673	33.78	2000	0.3	2.02E-05	6.6E+08

Latent Heat for SS316L

Latent Heat (J/kg)	Solidus Temp (K)	Liquidus Temp (K)
276000	1643	1673

Bulk density For SS316L

Mass Density (kg/m³) (ρ)
7.96E-09

Yield stress vs Yield strain

Stress (MPa)	Strain (mm/mm)
210	0.000
238	0.002
292	0.100
325	0.200
393	0.500
494	1.000
648	2.000
775	3.000
880	4.000